

**CGER'S SUPERCOMPUTER MONOGRAPH REPORT Vol.12**

**Climate Change Simulations with a Coupled Ocean-Atmosphere GCM  
Called the Model for Interdisciplinary Research on Climate: MIROC**

Toru Nozawa, Tatsuya Nagashima, Tomo'o Ogura, Tokuta Yokohata,  
Naosuke Okada, and Hideo Shiogama

**Center for Global Environmental Research**



**National Institute for Environmental Studies, Japan**



**CGER'S SUPERCOMPUTER MONOGRAPH REPORT Vol.12**

**Climate Change Simulations with a Coupled Ocean-Atmosphere GCM  
Called the Model for Interdisciplinary Research on Climate: MIROC**

Toru Nozawa, Tatsuya Nagashima, Tomo'o Ogura, Tokuta Yokohata,  
Naosuke Okada, and Hideo Shiogama

**Center for Global Environmental Research**



**National Institute for Environmental Studies, Japan**



**Supercomputer Steering Committee (FY2006):**

Yasumasa Kanada (University of Tokyo)  
Teruyuki Nakajima (University of Tokyo)  
Akira Noda (Meteorological Research Institute)  
Hiromasa Ueda (Acid Deposition and Oxidant Research Center)  
Hideo Harasawa (NIES)  
Takashi Imamura (NIES)  
Kunio Kohata (NIES)  
Motokazu Iwata\*<sup>1</sup> (EIC/NIES)  
Hidemasa Yamamoto (EIC/NIES)  
Yukihiro Nojiri (CGER/NIES)

**Coordination for Resource Allocation of the Supercomputer (FY2006):**

Yukihiro Nojiri (Deputy Director, CGER/NIES)  
Yasumi Fujinuma (CGER/NIES)  
Akira Yamamoto (CGER/NIES)

**Maintenance of the Supercomputer System (FY2006):**

Motokazu Iwata\*<sup>1</sup> (EIC/NIES)  
Hidemasa Yamamoto (Director, EIC/NIES)  
Kunihiko Shirai (Head, EIC/NIES)  
Hiroaki Abe (EIC/NIES)

**Operation of the Supercomputer System:**

System Engineers of NEC

**Editors:**

Akira Yamamoto (Chief)  
Hiroko Kaizu  
Atsuko Isaka

\*<sup>1</sup> Present Affiliation: Japan Environmental Safety Corporation

---

**Copies of this report can be obtained by contacting:**

Center for Global Environmental Research  
National Institute for Environmental Studies  
16-2 Onogawa, Tsukuba, Ibaraki 305-8506, Japan  
Fax: +81-29-858-2645  
E-mail: cgerpub@nies.go.jp

The report is also available as a PDF file.

See: [http://www-cger.nies.go.jp/cger-e/e\\_report/r\\_index-e.html](http://www-cger.nies.go.jp/cger-e/e_report/r_index-e.html)

**Copyright 2007:**

NIES: National Institute for Environmental Studies

*This book is printed on recycled paper.*

## Foreword

The Center for Global Environmental Research (CGER) at the National Institute for Environmental Studies (NIES) was established in October 1990. CGER's main objectives are to contribute to the scientific understanding of global change and to identify solutions for pressing environmental problems. CGER conducts environmental research from interdisciplinary, multi-agency, and international perspectives, provides an intellectual infrastructure for research activities in the form of databases and a supercomputer system, and makes the data from its long-term monitoring of the global environment available to the public.

CGER installed its first supercomputer system (NEC SX-3, Model 14) in March 1992. That system was subsequently upgraded to an NEC Model SX-4/32 in 1997, and an NEC Model SX-6 in 2002. In March 2007, we replaced that system with an NEC Model SX-8R/128M16 in order to provide an increased capacity for speed and storage. We expect our research to benefit directly from this upgrade.

The supercomputer system is available for use by researchers from NIES and other research organizations and universities in Japan. The Supercomputer Steering Committee evaluates proposals of research requiring the use of the system. The committee consists of leading Japanese scientists in climate modeling, atmospheric chemistry, ocean environment, computer science, and other areas of concern in global environmental research. In the 2005 fiscal year (April 2005 to March 2006), sixteen proposals were approved.

To promote the dissemination of the results, we publish both an Annual Activity Report and occasional Monograph Reports. The Annual Activity Report presents results for all research projects that have used the supercomputer system in a single year. Each Monograph Report presents the integrated results of a completed research program.

This Monograph Report presents the results obtained between 2000 to 2006 from the joint NIES/CCSR/FRCGC research program entitled "Climate Change Experiments with a High-Resolution Coupled Atmosphere-Ocean General Circulation Model (CGCM)". The Model for Interdisciplinary Research on Climate (MIROC), which was developed as a part of this research, is a world class CGCM and the results of this research will allow us to make a substantial contribution to the comprehension and projection of climate change.

In the years to come, we will continue to support environmental research with our supercomputer resources and disseminate practical information on our results.

March 2007



Yasuhiro Sasano  
Director  
Center for Global Environmental Research  
National Institute for Environmental Studies

## Preface

The present volume of CGER'S SUPERCOMPUTER MONOGRAPH REPORT series is the twelfth publication of research results achieved by the users of the supercomputer facilities at the Center for Global Environmental Research (CGER) of the National Institute for Environmental Studies (NIES). Our computer resources have been used by the collaborative research group at NIES, the Center for Climate System Research (CCSR) at the University of Tokyo, and the Frontier Research Center for Global Change (FRCGC) at the Japan Agency for Marine-Earth Science and Technology (JAMSTEC). These groups have been participating in studies on global climate change using the new version of their coupled ocean-atmosphere general circulation model (CGCM) known as the Model for Interdisciplinary Research on Climate (MIROC).

This joint research team involving CCSR, NIES, and FRCGC has developed two versions of MIROC: one with a higher resolution (with about 100 km and 20 km horizontal resolution in the atmosphere and ocean, respectively) for research on regional as well as global climate change and extreme events, and another with medium resolution (with about 300 km and 150 km horizontal resolution in the atmosphere and ocean, respectively) for research on historical simulations and future projections, ensembles, and climate sensitivity. This monograph deals with the results from various climate change simulations done with the medium resolution version of MIROC. A subset of the simulated results are provided to climate scientists worldwide as our contribution to the forthcoming Intergovernmental Panel on Climate Change (IPCC) 4th Assessment Report (AR4), and many results of analyses using the dataset simulated by MIROC have already been reported in scientific journals.

I hope this publication contributes to further progress in research on global environmental change, especially in the area of global warming.

March 2007

A handwritten signature in black ink, consisting of three characters: '野' (Nozawa), '沢' (Nozawa), and '徹' (Nozawa).

Toru Nozawa  
Chief of Atmospheric Physics Section,  
Atmospheric Environment Division,  
National Institute for Environmental Studies

# Contents

Foreword .....	i
Preface .....	ii
Contents .....	iii
List of Figures .....	v
List of Tables .....	viii
 Abstract .....	 2
 <b>Chapter 1</b> <b>General Introduction</b> .....	  3
References .....	4
 <b>Chapter 2</b> <b>Model Description and Experimental Design</b>	
2.1 Model Description .....	5
2.1.1 Model Overview .....	5
2.1.2 Climate Sensitivity of MIROC .....	7
2.2 Experimental Design .....	8
2.2.1 How the Climate Forcing Agents Were Incorporated into MIROC .....	8
2.2.2 Pre-industrial Control Simulation .....	10
2.2.3 1%/year CO <sub>2</sub> Increase Simulation .....	10
2.2.4 20th Century Simulation .....	10
2.2.5 21st Century Simulation .....	17
References .....	20
 <b>Chapter 3</b> <b>Simulated Climate States in the Control Experiment</b>	
3.1 Time Evolution of the Climate System .....	23
3.2 Mean States of the Climate System .....	25
3.3 Variability of the Climate System .....	31
References .....	33
 <b>Chapter 4</b> <b>Transient Climate Responses to Increasing CO<sub>2</sub></b>	
4.1 Time Evolution of the Climate System .....	35
4.2 Mean Climate States in Global Warming .....	38
4.3 Climate Feedback Processes in Global Warming .....	42
References .....	45

## Chapter 5

### 20th Century Simulations

5.1 Causes of Global Warming during the Latter Half of the 20th Century .....	47
5.1.1 Goals of This Section.....	47
5.1.2 Experiments .....	47
5.1.3 Results .....	47
5.2 Causes of Global Warming during the Early Half of the 20th Century: (1) Influences of Natural and Anthropogenic Forcings .....	49
5.2.1 Goals of This Section.....	49
5.2.2 Experiments .....	49
5.2.3 Results .....	49
5.2.4 Discussion.....	52
5.3 Causes of Global Warming during the Early Half of the 20th Century: (2) Influences of Volcanic Activity and Changes in Solar Irradiance .....	52
5.3.1 Goals of This Section.....	52
5.3.2 Experiments .....	52
5.3.3 Detection and Attribution .....	53
5.3.4 Comparison with the HadCM3 Model .....	56
5.3.5 Discussion.....	57
5.4 Causes of the Changes in SAT during the Mid-20th Century.....	57
5.4.1 Goals of This Section.....	57
5.4.2 Experiments .....	57
5.4.3 Results .....	58
5.4.4 Discussion.....	62
5.5 Causes of the Changes in Temperature Extremes .....	63
5.5.1 Goals of This Section.....	63
5.5.2 Data and Experiments.....	63
5.5.3 Results .....	64
5.5.4 Discussion.....	65
References .....	68

## Chapter 6

### Projections of Climate Change under IPCC SRES Scenarios

6.1 Surface Air Temperature .....	71
6.2 Precipitation .....	72
6.3 Commitment Scenarios .....	75
References .....	76

## Chapter 7

Summary and Conclusions .....	77
References .....	79

## List of Figures

### Chapter 2

2.1	Time series of global annual mean land surface temperature for pre-industrial CO <sub>2</sub> concentration experiments and doubled CO <sub>2</sub> experiments .....	7
2.2	Historical time series of total solar irradiance (TSI) from Lean <i>et al.</i> (1995).....	11
2.3	Historical time series of monthly global mean volcanic aerosol optical thickness at 550 nm integrated in the lower to middle stratosphere compiled by Sato <i>et al.</i> (1986) and updated by Hansen <i>et al.</i> (2002) .....	12
2.4	Historical time series of global annual mean volume mixing ratios of well-mixed GHGs: CO <sub>2</sub> , N <sub>2</sub> O, CH <sub>4</sub> , and the sum of halocarbons.....	12
2.5	(a) Zonal mean change in ozone (%) from the 1901-1915 mean to the 1986-2000 mean. (b) Historical time series of global annual mean ozone mixing ratio at circa 60 hPa and at the surface. Horizontal distributions of the ozone mixing ratio (ppbv) at the surface averaged over (c) 1901-1915 and (d) 1986-2000.....	13
2.6	Horizontal distributions of SO <sub>2</sub> emissions from anthropogenic sources (TgS/year) averaged over 1901-1925 and 1986-2000.....	14
2.7	Horizontal distributions of black carbon aerosol emissions from fossil fuel combustion, domestic fuelwood consumption, agricultural waste combustion, and biomass burning in TgS/year averaged over 1901-1925 and 1986-2000 .....	15
2.8	Historical time series of globally integrated emissions of (a) SO <sub>2</sub> (TgS/year) and (b) black carbon aerosols from each source (Tg/year).....	16
2.9	Schematic illustration of the 4 SRES scenario families. The short summaries of the scenarios are taken from IPCC (2000) .....	18
2.10	Temporal evolution of global annual mean volume mixing ratios of well-mixed GHGs: CO <sub>2</sub> , N <sub>2</sub> O, CH <sub>4</sub> and the sum of halocarbons for A1B, A2, and B1 scenarios.....	18
2.11	Temporal evolution of globally integrated emissions of (a) SO <sub>2</sub> (TgS/year) and (b) black carbon aerosols from each source (Tg/year).....	19
2.12	Temporal evolution of the global annual mean ozone mixing ratio at circa 60 hPa and at the surface .....	19

### Chapter 3

3.1	Time series of globally averaged a) surface air temperature, b) 3m soil temperature. Annually averaged data are used for the plot.....	23
3.2	Time series of globally averaged a) ocean mean temperature, b) ocean temperature anomaly, and c) maximum of stream function of North Atlantic deep water (NADW). Annually averaged data are used for a) and c), and 10-year averaged data are used for b).....	24
3.3	Global map of the model simulation and the difference from observation for a-b) surface air temperature, c-d) sea surface temperature, and e-f) precipitation .....	26
3.4	Sea-ice concentration of the model simulation and observation.....	27
3.5	Same as Fig. 3.3 but for the net downward a-b) shortwave (SW) radiation at top of the atmosphere (TOA) and c-d) SW cloud radiative forcing (CRF) at the TOA.....	28
3.6	Same as Fig. 3.5 but for the longwave (LW) radiation.....	28
3.7	Zonal mean of the model simulation and difference from observation for a-b) atmospheric temperature, c-d) specific humidity, and e-f) relative humidity.....	30
3.8	Zonal mean of the model simulation for a) cloud water formed by cumulus convection, b) cloud water formed by large scale condensation (LSC), and c) total cloud fraction.....	31



3.9	El Niño/Southern Oscillation index from 20 years of data from the model simulation and observation from the year 1991 to 2000. a-b) NINO3 index and c-d) Equatorial (from 4°S to 4°N) SST anomaly at longitudes from 120° to 270° .....	32
-----	---	----

## Chapter 4

4.1	Time series of globally averaged atmospheric temperature anomalies in the 1%/year CO <sub>2</sub> increase experiment (1%CO <sub>2</sub> ). Anomalous time series of a) surface air temperature (SAT) and b) vertical distribution .....	36
4.2	Time series of the globally averaged ocean temperature anomaly in 1%CO <sub>2</sub> for depths a) from the surface to 500 m and b) below 500 m .....	37
4.3	Global maps of the anomalies from the annual averages of a) SAT, b) diurnal maximum of SAT, c) diurnal minimum of SAT, and d) the difference between b) and c), namely the diurnal temperature range.....	38
4.4	Same as Fig. 4.3 but for a) sea surface temperature (SST), b) precipitation, c) precipitation by cumulus convection, and d) precipitation by large scale condensation (LSC).....	39
4.5	Anomalies in sea-ice concentration and sea-ice concentration at the time of doubled CO <sub>2</sub> (2XCO <sub>2</sub> ) .....	39
4.6	Zonal averages of anomalies in a) temperature, b) relative humidity, c) cloud water formed by cumulus convection, and d) cloud water by LSC .....	41
4.7	Zonal mean of zonal wind (u), a) anomaly calculated in the same way as Fig. 4.5, b) in the control experiment, and c) bias in the control experiment .....	42
4.8	Climate feedback analysis based on the scheme by Yokohata <i>et al.</i> , 2005. ....	43
4.9	Global maps of the parameters shown in Fig. 4.8.....	44

## Chapter 5

5.1	Temporal variations of global annual mean surface air temperature (SAT).....	48
5.2	Geographical distributions of linear SAT trends (K/decade) in the first half of the century for the (a) observations (Jones and Moberg, 2003) and the ensemble means of the (b) FULL, (c) NTRL, (d) ANTH, and (e) GHGS simulations .....	51
5.3	Best-estimated (a, b) signal amplitudes and (c, d) linear trends (K/century) with 5%-95% uncertainty ranges for the 50-year segment from 1900 to 1949 for the (a, c) GHGS, ANTH-GHGS (anthropogenic signal other than well-mixed GHGs), and the NTRL analyses and for the (b, d) ANTH and NTRL analyses .....	51
5.4	Temporal changes of global annual mean surface air temperature .....	54
5.5	Best estimates of (a) scaling factors and (b) linear trends (K/century) with 5%-95% uncertainty ranges for the SOLR and VLCN in a 2-way analysis .....	55
5.6	Same as Fig. 5.5, except for the ANTH, SOLR, and VLCN 3-way analysis.....	55
5.7	Time series of annual and global mean T2 from the observations (Johns and Moberg, 2003) and from the AEFX, CEFX, and FULL experiments expressed as anomalies relative to the 1881-1910 mean (K) .....	59
5.8	Geographical distributions of linear trends (K/decade) of T2 from 1942 to 1979 for (a) the observations (Johns and Moberg, 2003), (b) AEFX, (c) CEFX, and (d) FULL .....	60
5.9	Geographical distributions of linear trends of net RFs from 1940 to 1980 from carbonaceous (a and b) and sulfate (c and d) aerosols for direct (a and c) and first-indirect (b and d) effects at the Earth's surface, while (e) shows (a) but in the tropopause .....	61
5.10	Scaling factors by which we must multiply the model-simulated spatio-temporal change of T2 (1940-1979) to reproduce the corresponding change in the observation .....	62

5.11	Changes in the warmest night (1980–1999 minus 1950–1969; K) for (a) the observations, (b) GHGS, (c) ANTH, and (d) FULL .....	66
5.12	Scaling factors and their 5%–95% uncertainty ranges from single detection/attribution analyses .....	66
5.13	Changes in the frost days (1980–1999 minus 1950–1969; days) for (a) the observations, (b) GHGS, (c) ANTH, and (d) FULL .....	67
5.14	(a) Scaling factors and their 5%–95% uncertainty ranges from [GHGS, FULL–GHGS] multi detection/attribution analyses. The lower 3 panels are global mean linear trends with 5%–95% uncertainty ranges for (b) warmest day/night, (c) coldest day/night, and (d) summer/frost days .....	67

## Chapter 6

6.1	Changes in the global mean annual mean of surface air temperature (K; anomalies from the 1961–2000 mean) under (a) the A1B, (b) A2, and (c) B1 scenarios .....	71
6.2	Changes in surface air temperature (K; 2081–2100 minus 1961–2000) under (a) the A1B, (b) A2, and (c) B1 scenarios .....	72
6.3	Changes in the global mean annual mean of precipitation (percentile changes with respect to the 1961–2000 mean) under (a) the A1B, (b) A2, and (c) B1 scenarios .....	73
6.4	Same as Fig. 6.3 except for precipitable water (%) .....	73
6.5	Scatter plot of annual mean anomalies of SAT and precipitation for the period of 2001–2100 under the A1B, A2, and B1 scenarios .....	74
6.6	Changes in precipitation (%; 2081–2100 minus 1961–2000) under (a) the A1B, (b) A2, and (c) B1 scenarios .....	74
6.7	Changes in global mean of surface air temperature (K; anomalies from the 1961–2000 mean) under the year 2100 commitment experiment for A1B and A2, and the year 2000 commitment experiment .....	75
6.8	Same as Fig. 6.7 except for precipitation (%) .....	76

## **List of Tables**

### **Chapter 2**

2.1	Globally uniform climate forcings for the pre-industrial control simulation .....	10
2.2	Combinations of climate forcing agents for each experiment.....	16

**Climate Change Simulations with a Coupled Ocean-Atmosphere GCM  
Called the Model for Interdisciplinary Research on Climate: MIROC**

Toru Nozawa, Tatsuya Nagashima, Tomo'o Ogura, Tokuta Yokohata,  
Naosuke Okada, and Hideo Shiogama

*National Institute for Environmental Studies,  
16-2 Onogawa, Tsukuba, Ibaraki 305-8506, Japan*

## Abstract

Transient climate change simulations were carried out by using a coupled ocean-atmosphere general circulation model (CGCM) to study the mechanism of observed historical climate change and to investigate future possible climate responses to varying anthropogenic forcing factors. The CGCM used here is called the Model for Interdisciplinary Research on Climate (MIROC), which has been developed collaboratively by the National Institute for Environmental Studies (NIES), the Center for Climate System Research (CCSR) of the University of Tokyo, and the Frontier Research Center for Global Change (FRCGC) of the Japan Agency for Marine-Earth Science and Technology (JAMSTEC). The MIROC has an equilibrium climate sensitivity of 4.0 K to doubling the concentration of carbon dioxide ( $\text{CO}_2$ ).

Although the MIROC does not employ any flux adjustment, globally averaged surface air temperatures (SAT) in the control experiment showed no significant drift over more than 2000 years, indicating that the simulated control climate is extremely stable. In a 1% per year  $\text{CO}_2$  increase experiment, the increase in the globally averaged SAT was about 1.9 K by the time the  $\text{CO}_2$  concentration had doubled, which is about the average of the state-of-the-art climate models that contributed to the forthcoming Intergovernmental Panel on Climate Change (IPCC) 4th Assessment Report (AR4). For the historical climate change simulations, we considered most external forcings including both natural and anthropogenic factors. Our model can reproduce the observed global annual mean SAT change with this set of external forcings. A number of experiments with different combinations of external forcing factors were carried out to diagnose the relative importance of various forcings. These strongly suggest that the observed warming in the latter half of the 20th century results from anthropogenic forcings. On the other hand, the observed warming in the early half of the 20th century seems to result mainly from natural forcings, although we cannot rule out that increases in greenhouse-gas concentrations influenced global warming during this period. We also investigated the impact of aerosols on global mean SAT change for the middle and the latter half of the 20th century. For future projections, we carried out climate change simulations under the IPCC Special Report on Emissions Scenarios (SRES). The spatial distributions of changes in SAT and in precipitation are not markedly different among the scenarios, although their amplitudes differ.

## Chapter 1: General Introduction

Recent studies on historical changes in surface air temperature (SAT) show that the observed global annual mean SAT increased about 0.6 K in the 20th century (e.g., Jones and Moberg, 2003; Brohan *et al.*, 2006). According to the Intergovernmental Panel on Climate Change (IPCC) Third Assessment Report (TAR; IPCC, 2001), most of the warming observed in the second half of the 20th century is likely to have been caused by increasing levels of greenhouse gas concentrations. There is concern that serious climate change may occur due to increasing concentrations of well-mixed greenhouse gases, and that such climate change may have considerable impact on water resources, ecosystems, etc., in the near future.

To make future climate change projections, it is useful to employ numerical climate models. In the IPCC TAR, increases in global annual mean SAT from 1990 to 2100 are estimated ranging from 1.4 to 5.8 K based on a number of climate models (mainly using simple climate models whose major parameters are calibrated to yield a climate response equivalent to complex climate models) for the full range of the IPCC Special Report on Emissions Scenarios (SRES; IPCC, 2000). The climate-modeling group of the Center for Climate System Research (CCSR) of the University of Tokyo and the National Institute for Environmental Studies (NIES) contributed to the IPCC TAR by performing several numerical simulations with a previous version of the CCSR/NIES coupled ocean-atmosphere general circulation model (CGCM). For example, the global and annual mean SAT change in 2100 with respect to the 1961–90 average ranges from 3.3 to 5.5 K for all the SRES marker scenarios. Further details of projected future climate change are described in Nozawa *et al.* (2003).

A few years ago, climate-modeling groups around the world were requested to perform an unprecedented set of coordinated climate change experiments in the past and future for the IPCC Fourth Assessment Report (AR4). In response to this, our research group, which consists of the CCSR, NIES, and the Frontier Research Center for Global Change (FRCGC) of the Japan Agency for Marine-Earth Science and Technology (JAMSTEC), collaboratively developed a state-of-the-art CGCM (K-1 model developers, 2004), called the Model for Interdisciplinary Research on Climate (MIROC), with the aim of making substantial contributions to the IPCC AR4. Almost all the requested climate change experiments were carried out, and the simulated results as well as the experimental design are described in this report. Chapter 2 presents a brief description of the model, experimental design, and details of the external forcing factors used in the 20th and 21st century climate change experiments. Simulated climate states in the long-term pre-industrial control experiment and transient climate responses to increasing concentrations of carbon dioxide (CO<sub>2</sub>) are described in chapters 3 and 4, respectively. Chapter 5 deals with the results from the 20th century simulations. Analysis is concentrated on the causes of global warming in the early half of the 20th century, the impacts of carbonaceous aerosols on SAT changes in the mid-20th century, and the causes of the changes in temperature extremes in the latter half of the 20th century. Chapter 6 describes projections of future climate change based on the IPCC SRES marker scenarios, and conclusions are summarized in chapter 7.

## References

- Brohan, P., Kennedy, J.J., Harris, I., Tett, S.F.B., Jones P.D. (2006) Uncertainty estimates in regional and global observed temperature changes: A new data set from 1850, *J. Geophys. Res.*, 111, D12106.
- IPCC (2000) Special Report on Emission Scenarios, Nakicenovic, N., Swart, R. (eds.), Cambridge University Press, Cambridge, UK, 612pp.
- IPCC (2001) Climate Change 2001: The Scientific Basis. Contribution of Working Group I to the Third Assessment Report of the Intergovernmental Panel on Climate Change, Houghton, J.T., Ding, Y., Griggs, D. J., Noguer, M., van der Linden, P.J., Dai, X., Maskell, K., Johnson, C.A. (eds.), Cambridge University Press, Cambridge, United Kingdom and New York, NY, USA, 881pp.
- Jones, P.D., Moberg, A. (2003) Hemispheric and large-scale surface air temperature variations: An extensive revision and an update to 2001, *J. Climate*, 16, 206-223.
- K-1 model developers (2004) K-1 coupled GCM (MIROC) description, K-1 technical report. 1, Hasumi, H., Emori, S. (eds.), Center for Climate System Research, University of Tokyo, Tokyo, 34pp.
- Nozawa, T., Emori, S., Numaguti, A., Tsushima, Y., Takemura, T., Nakajima, T., Abe-Ouchi, A., Kimoto, M. (2003) Transient climate change simulations in the 21st century with the CCSR/NIES CGCM under a new set of IPCC SRES scenarios, CGER's Supercomputer Monograph Report, 8, CGER-REPORT, CGER/NIES, Tsukuba, 44pp.

## Chapter 2: Model Description and Experimental Design

In this chapter, we present brief descriptions of the climate model we used and the experimental design, including details of the external forcing factors adopted in each simulation.

### 2.1 Model Description

The model used for the series of experiments reported here is a coupled atmosphere-ocean general circulation model (CGCM) called MIROC (Model for Interdisciplinary Research on Climate). MIROC has been developed with the collaboration of the Center for Climate System Research (CCSR), University of Tokyo; National Institute for Environmental Studies (NIES); and the Frontier Research Center for Global Change (FRCGC). A detailed description of MIROC's numerical algorithms, theories, and physical parameterizations can be found in K-1 model developers (2004). There are 2 different well-maintained setups of MIROC, both of which have been applied to climate studies, one with high resolution (hereafter higher-resolution setup) and the other with low resolution (hereafter lower-resolution setup). The higher-resolution setup is the flagship of MIROC and is used to study phenomena having relatively small spatial scales, such as extreme climate events or regional climate change as well as global climate issues. However, the higher-resolution setup is so computationally expensive to run that multi-ensemble or multi-scenario integrations, which are necessary to get statistically reliable results on climate change, are difficult to perform even if we can use the Earth Simulator. Therefore, a lower-resolution setup, which is computationally cheap to run, has been developed to be available for multi-member integrations, which extend the ability of MIROC in climate research. The NIES staff has the main responsibility for tuning, maintaining, and performing runs using the lower-resolution setup of MIROC. Here, we present a brief summary of the main components of the lower-resolution setup of MIROC, followed by information about climate sensitivity.

#### 2.1.1 Model Overview

The atmospheric component of MIROC is the CCSR/NIES/FRCGC Atmospheric General Circulation Model (AGCM) version 5.7, which is based on the CCSR/NIES AGCM described in Numaguti *et al.*, (1997). In the lower-resolution setup, horizontal resolution of T42 is employed in which the grid spacing is approximately  $2.8^\circ$  (~300 km). There are 20 vertical  $\sigma$  layers. The  $\sigma$  values of the vertical layer boundaries are 1.000, 0.990, 0.970, 0.930, 0.870, 0.790, 0.700, 0.600, 0.500, 0.410, 0.330, 0.260, 0.200, 0.150, 0.100, 0.070, 0.050, 0.040, 0.030, 0.020, and 0.0001. The height of the model top layer is approximately 30 km. The physical parameterizations include a radiation scheme with a 2-stream discrete ordinate method and a k-distribution method, a prognostic Arakawa-Schubert cumulus scheme, a prognostic cloud water scheme for large-scale condensation, a turbulence closure scheme with cloud effects, and an orographic gravity wave drag scheme. In the radiation scheme, the absorption by major well-mixed greenhouse gases ( $\text{CO}_2$ ,  $\text{CH}_4$ ,  $\text{N}_2\text{O}$ , and 16 kinds of organic halogen species) is considered. References to each parameterization can be found in K-1 model developers (2004). One of the main features of this version of the CCSR/NIES/FRCGC AGCM is an interactive calculation of atmospheric aerosols. A simplified version of the aerosol transport module (SPRINTARS; Takemura *et al.*, 2000, 2002) can calculate the global 3-dimensional distributions of 5 sorts of aerosols: soil dust, sea salt, sulfate, black carbon



(BC), and organic carbon (OC). Then, the calculated distributions of these aerosols are used in the radiation scheme to estimate the direct radiative effect of aerosols in which the aerosol particles scatter and absorb solar and thermal radiation. Moreover, the first and second indirect radiative effects of aerosols, in which soluble aerosols change the size of cloud droplets and the lifetime of a cloud acting as cloud condensation nuclei are explicitly represented through an empirical relationship between the cloud droplet number concentration  $N_c$  and the soluble aerosol (sea salt, sulfate, and organic carbon) particle number concentration  $N_a$ :

$$N_c = \frac{\varepsilon N_a N_m}{\varepsilon N_a + N_m}, \quad (2.1)$$

where  $\varepsilon$  and  $N_m$  are constants. Then, the radius of the cloud droplet and the rate of conversion from cloud droplets to rain, which determines the cloud lifetime, are estimated using  $N_c$  as determined from the above formula.

The land-surface module MATSIRO (Minimal Advanced Treatments of Surface Interaction and RunOff; Takata *et al.*, 2003) is used to represent energy and water exchange between land-surface and atmosphere. MATSIRO has 1 canopy layer, 5 soil layers, and a variable number of snow layers (0–3 depending on the snow amount). The thicknesses of the soil layers from the top are 5, 20, 75, 100, and 200 cm. The canopy and surface skin layer do not have heat capacity. The horizontal resolution and the grid structure are the same as those of the AGCM, that is, T42. The boundary conditions required are land-cover type, soil type, leaf area index (LAI), soil albedo for visible and near-IR wavelength bands, mean surface slope, and the standard deviation of surface height. The LAI should be prescribed by a monthly dataset, while the others are temporally constant. The same concentration of CO<sub>2</sub> as in the radiation scheme is also used in MATSIRO. The runoff water from the land-surface model is transported to the ocean model at river mouths by the river routing module. The module predicts river water storage in each grid box assuming a globally uniform and temporary constant river flow speed of 0.3 m/s. Glacier flow (an amount of snow exceeding a certain critical value is treated as glacier in the land-surface model) is also treated in this module, although the freezing and thawing of river water is not considered. The river flow direction dataset developed by Dr. Shinjiro Kanae (personal communication), which is similar in structure to the TRIP (Total Runoff Integrating Pathways; Oki and Sud, 1998) dataset, is used.

The ocean component of MIROC is the CCSR Ocean Component Model (COCO; Hasumi, 2000) version 3.4. COCO is an ocean general circulation model (OGCM) and the basic equations of COCO are the primitive equations on a sphere, for which the Boussinesq and hydrostatic approximations are adopted. The model explicitly represents the sea surface elevation. The vertical coordinate of the model is a hybrid of  $\sigma$  (normalized depth) and  $z$  (geopotential height). The  $\sigma$ -coordinate is introduced to avoid the disappearance of the top level. There are 43 vertical levels, excluding the bottom boundary layer, 8 of which are within the  $\sigma$ -coordinate. The vertical grid spacing varies with depth with values 5, 5, 5, 5, 5, 5, 7.5, 7.5, 10, 10, 10, 10, 15, 20, 25, 25, 30, 50, 75, 75, 100, 100, 150, 150, 150, 150, 200, 250, 250, 250, 250, 250, 250, 250, 250, 250, 250, 250, 250, 250, 250, 250, and 250 m from the top to the bottom. The zonal resolution is  $1.40625^\circ (= 360^\circ/256)$ . The meridional resolution is about  $0.56^\circ$  at latitudes lower than  $8^\circ$  and  $1.4^\circ$  at latitudes higher than  $65^\circ$ , with a smooth transition in between. The exchanges of information through the straits that cannot be resolved due to the coarse horizontal resolution are artificially expressed by 2-way linear dumping. The water pathway through the Canadian Archipelago is also represented by artificially excavating a channel. The physical processes included as forms of parameterizations are vertical

convection, vertical mixing, lateral mixing of momentum and tracer, bottom boundary layer, and vertical penetration of shortwave radiation. Sea ice is treated as a 2-dimensional continuum. In each horizontal grid, concentration, mean thickness (over the ice-covered portion), and horizontal velocity components are predicted. Sea ice concentration and thickness change due to thermodynamic growth/decay, advection, and mechanical deformation of ice floes. The horizontal resolution of the sea ice model is taken to be the same as that of the ocean model. References to each parameterization and sea ice modeling can be found in K-1 model developers (2004).

### 2.1.2 Climate Sensitivity of MIROC

Climate sensitivity, which is measured as the equilibrium response of the surface temperature to a doubling of the atmospheric CO<sub>2</sub> concentration, is one of the key characteristics of a CGCM for understanding the projected climate in the next hundred years when used in a global warming experiment. There has been a wide variety of projected surface temperature rise estimates by various CGCMs due to differences in climate sensitivity, even if the CGCMs are driven by similar climate forcings. The predecessor of MIROC yielded the highest surface temperature rise in a global warming experiment among the CGCMs that participated in the Third Assessment Report of the Intergovernmental Panel on Climate Change (IPCC/TAR; IPCC, 2001), which means our model might have the highest climate sensitivity. In the course of investigating the cause of this high climate sensitivity, we got to have 2 different setups of MIROC, each of which have a similar ability to reproduce the current climate but have the totally different climate sensitivities: a higher one of 6.3 K, and a lower one of 4.0 K (Fig. 2.1). Fig. 2.1 shows the global annual mean surface temperature time series calculated with these 2 different setups of MIROC but they are coupled with a mixed-layer type ocean module. Two pairs of experiments were performed with both setups of MIROC: each pair consisted of an experiment forced with a pre-industrial atmospheric CO<sub>2</sub> concentration (285.431 ppmv; solid lines) and one with doubled CO<sub>2</sub> concentration (570.862 ppmv; dotted lines). The experiments were continued for 60 years to reach equilibrium states. The 2 setups have a number of differences in the treatment of the cloud microphysics parameterization. A detailed investigation of how such differences in cloud microphysics lead to a difference in climate sensitivity appears in Ogura *et al.*, (2007). In brief, since the decrease of cloud water in response to global warming is larger in the higher sensitivity setup, more solar radiation could be penetrating to and absorbed at the surface, in which case the atmosphere is warmed more in the higher sensitivity setup than in the lower one. In this report, almost all the results shown are calculated with the lower sensitivity setup of MIROC.

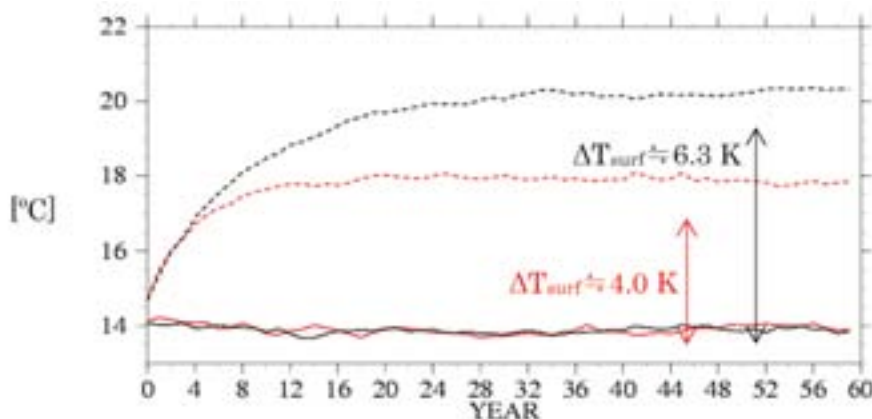


**Fig. 2.1:** Time series of global annual mean land surface temperature for pre-industrial CO<sub>2</sub> concentration experiments (solid lines) and doubled CO<sub>2</sub> experiments (dotted lines). Red lines denote the results with the lower sensitivity setup and the black lines with the higher sensitivity setup.

## 2.2 Experimental Design

One of the main motivations behind the series of experiments shown in this report is the participation in and contribution to IPCC activity. For the forthcoming fourth assessment report (AR4) of the IPCC, the following 4 sets of simulations were planned and performed by using the low-resolution and lower sensitivity setup of MIROC, which broadly cover the required experiments for IPCC/AR4.

1. **Pre-industrial control simulation:** Control for the other simulations. With all climate forcings on the model set to values corresponding to the pre-industrial era, several centennial integrations need to be performed.
2. **20th century simulation:** Experiment to reproduce the 20th century climate. Additional companion experiments are forced with several different combinations of climate forcing agents of the 20th century.
3. **21st century simulation:** Projection experiments of the 21st century climate that assume several different scenarios of greenhouse gas concentrations, aerosol emissions, etc. Some scenarios are extended to the end of the 22nd century.
4. **1%/year CO<sub>2</sub> increase simulation:** Experiments to see the response of the CGCM to an increase of 1% per year in atmospheric CO<sub>2</sub>. Two follow-up experiments are performed that branch from the point when CO<sub>2</sub> reaches doubled and quadrupled concentrations with holding CO<sub>2</sub> fixed at those values.

### 2.2.1 How the Climate Forcing Agents Were Incorporated into MIROC

Except for the pre-industrial control simulation, all the above simulations need to be driven by year-to-year changes of climate forcing agents specific to each simulation. We considered as many climate forcing agents to drive MIROC as possible, and they can be classified into natural and anthropogenic agents. In this section, the methods used to incorporate these climate forcing agents into the model are introduced. The combination of climate forcing agents and the sources of the climate forcing datasets actually employed in each simulation are presented in the next section.

**Solar radiation:** Incoming solar radiation is a well-known natural external climate forcing agent that has a periodically variable energy on various time scales (e.g., 27 days, 11 years). Temporal changes of both total solar irradiance (TSI) and spectral irradiance in each wavelength band at the top of the atmosphere are considered in the radiative transfer calculation. To consider the spectral change of solar irradiance we employed the method of the Hadley Center group (G. Johns, private communication), which is based on the empirical regression method by Lean *et al.* (1995b).

**Volcanism:** Large volcanic eruptions, which can also be regarded as a natural climate forcing agent, have had a tremendous impact on climate through modulation of the radiation budget by enormous amounts of erupted aerosols that act as a sunshade for the Earth. To consider such an effect, data on aerosol optical thickness (AOT) increments due to large volcanic eruptions, whose plumes of volcanic ash and aerosols could enter the stratosphere, were supposed to be placed on the upper adjacent layer of the tropopause in the model. However, by mistake we placed them specifically in the 50 hPa layer. This might have some effect on the stratospheric dynamics.

Note that a temporal change of these natural climate forcing agents is considered only in the 20th century simulation. In the other simulations, TSI and volcanic AOT data

corresponding to the year 1850 or 2000 are used repeatedly during the integration according to their purpose.

Rapid industrialization and its worldwide spread from the 19th century has brought several environmental problems through the massive consumption and emission of various chemical substances and alteration of land use. Some of them have been recognized to have a considerable impact on global and regional climate systems. We considered the following 6 agents as the leading anthropogenic climate forcing agents: well-mixed greenhouse gases, tropospheric ozone, stratospheric ozone, sulfate aerosol, carbonaceous aerosol, and land-use change.

**Well-mixed greenhouse gases:** Greenhouse gases (GHGs) that have relatively long lifetimes in the troposphere are assumed to be well mixed, so the mixing ratios of such gases are given to the model as globally and vertically uniform values. Annual cycles of GHG mixing ratios are not considered. The well-mixed GHGs considered in the model are CO<sub>2</sub>, CH<sub>4</sub>, N<sub>2</sub>O, CCl<sub>4</sub>, CFC11, CFC12, CFC113, CFC114, CFC115, CH<sub>3</sub>CCl<sub>3</sub>, HCFC123, HCFC124, HCFC22, HFC125, HFC134a, HFC141b, HFC142b, HFC143a, and HFC152a.

**Ozone:** The distribution of ozone shows a notable inhomogeneity in both the horizontal and vertical directions and temporally. To include this inhomogeneity, monthly 2- or 3-dimensional data of ozone mixing ratios are provided for the model. While zonal mean monthly data are used in the stratosphere due to the relatively small zonal structure of ozone in the stratosphere, 3-dimensional monthly data are employed in the troposphere because there are localized maxima of ozone concentration near the surface of polluted regions, which might have a large localized radiative impact.

**Sulfate aerosol:** The 3-dimensional distribution of sulfate aerosol is internally calculated through emission, chemistry, deposition, and transport processes in the model. Then, the distribution is passed to radiation and large-scale condensation modules to calculate the direct and indirect effects of sulfate aerosols. An emission map of SO<sub>2</sub>, which is a precursor of sulfate aerosol, from anthropogenic sources and continuously erupting volcanoes is given to the model. The emission of dimethylsulfide (DMS), which is another precursor of sulfate, is internally calculated by using an empirical formula. The concentrations of ozone, hydroxyl radical (OH), and hydrogen peroxide (H<sub>2</sub>O<sub>2</sub>) are given to the model to calculate the oxidation processes of SO<sub>2</sub> and DMS.

**Carbonaceous aerosol:** The procedure for carbonaceous aerosol is similar to that for sulfate aerosol, but no chemical process refers to carbonaceous aerosol. Emission maps of BC from fossil fuel combustion, domestic fuelwood consumption, agricultural waste combustion, and biomass burning are given to the model. OC emissions from these anthropogenic sources are assumed to be proportional to the corresponding BC emission. For OC, biogenic emissions originating from terpenes are also considered.

**Land-use change:** In the MATSIRO module, 1 of the 10 types of land-use conditions (e.g., cultivation, broadleaf evergreen forest, tundra) is assigned to each land surface grid, where each type is invested with its characteristic vegetation parameters. With applying these parameters as well as the prescribed annual cycle of LAI for each grid, MATSIRO calculates the energy and water exchange between land-surface and atmosphere. Therefore, a temporal change of land-use conditions and/or of LAI could have an impact on the climate system. Among the historical changes of land-use, we considered only the increase of crop area, which is the most notable change in land use during the 20th century, in the 20th century simulation. In the other simulations, datasets for the year 1850 or 2000 are repeatedly used during the integration according to their purpose.

### 2.2.2 Pre-industrial Control Simulation

Because we do not use the flux correction method to stabilize the simulated climate, it is necessary to ensure that a steady climate is simulated without any unintentional climate drift. After several trial runs, we finally obtained a proper set of parameters for a non-drifting climate. With these parameters, a control simulation under pre-industrial climate forcings (hereinafter CONT), where all climate forcing agents were set to values corresponding to the year 1850, was performed. Those that can be given as a globally uniform value are listed in Table 2.1. For the other climate forcings, values of the year 1850 in datasets that were prepared for the 20th century simulation were used (see 2.2.4 for details). The initial conditions were taken from a trial run, and the integrations have been performed for over 2500 years (as of October 2006).

**Table 2.1: Globally uniform climate forcings for pre-industrial control simulation**

TSI [W/m <sup>2</sup> ]	CO <sub>2</sub> [ppmv]	CH <sub>4</sub> [ppbv]	N <sub>2</sub> O [ppbv]	CCl <sub>4</sub> [pptv]	The other halocarbons
1366.12	285.431	279.266	863.303	1.72222	0.0

### 2.2.3 1%/year CO<sub>2</sub> Increase Simulation

The Coupled Model Inter-comparison Project (CMIP) studies the intrinsic differences between global CGCMs when they are forced with the same climate forcing scenario (Covey *et al.*, 2003). The scenario is an idealized one in which CO<sub>2</sub> increases at the rate of 1% per year. Other anthropogenic climate forcing agents (i.e., other GHGs, anthropogenic aerosols, and land-use) as well as natural ones (i.e., volcanism and solar radiation) are kept fixed. We followed this experimental design, and during the integration fixed the climate forcing agents other than CO<sub>2</sub> at the values corresponding to the year 1850 (cf. 2.2.2). The initial conditions were taken from the pre-industrial control simulation, so the initial CO<sub>2</sub> concentration was 285.431 ppmv. The simulation consists of 3 parts: 1%/year CO<sub>2</sub> increase run for 150 years (hereinafter INCR), an additional run starting from year 70 of INCR when the CO<sub>2</sub> had doubled in concentration (hereinafter 2xCO<sub>2</sub>), and another additional run starting from year 140 of INCR when the CO<sub>2</sub> had quadrupled in concentration (hereinafter 4xCO<sub>2</sub>). In the 2xCO<sub>2</sub> (4xCO<sub>2</sub>) run, the concentration of CO<sub>2</sub> was held fixed at 570.862 (1141.724) ppmv during the integration of 150 years. INCR consists of 3 ensemble members, starting from different initial conditions taken from CONT at intervals of 100 years. Only 1 run was performed for 2xCO<sub>2</sub> and 4xCO<sub>2</sub>.

### 2.2.4 20th Century Simulation

It is highly important to estimate the ability of a CGCM to simulate the actually observed past climate if one is to use that model for the projection of future climate. A future climate calculated with a CGCM that could not properly simulate the real climate would not be trusted. From this point of view, reproduction simulation of the 20th century climate with CGCMs has risen in importance in recent years. To simulate the 20th century climate, we decided upon a period of integration from 1850 to 2000 and compiled the available data of each climate forcing agent mentioned in 2.2.1 for this period.

For the natural forcings, we used the long-term reconstructed data of TSI from Lean *et al.* (1995a) (Fig. 2.2) and the volcanic AOT increase data since 1850 compiled by Sato *et al.*

(1993) and updated by Hansen *et al.* (2002), which provides the zonal mean monthly volcanic AOT at 550 nm in the lower to middle stratosphere (Fig. 2.3). In Fig. 2.2, the 11-year sunspot cycle and the irradiance variations that have similar or greater magnitude over periods longer than 11 years are significant, but a recent study has pointed out that the second component of TSI variation is overestimated to some degree (Foukal *et al.*, 2004).

The global annual mean time series of well-mixed GHGs used in the 20th century simulation are shown in Fig. 2.4. These data are taken from Johns *et al.* (2003). The concentrations of all species show fairly steady increases during the 20th century. Note that the increasing rate of CO<sub>2</sub> is far smaller than 1%/year.

It is well known that the massive consumption of halocarbons that appears in Fig. 2.4 has caused a significant reduction of stratospheric ozone since the late 1970s. Continuous observations of stratospheric ozone from satellites and by ozonesondes have revealed the trend of zonal mean stratospheric ozone for the period 1979-1997 (Randel and Wu, 1999). With this trend data and with zonal mean stratospheric ozone data representative of the mid-1980s (Wang *et al.*, 1995), we calculated the zonal mean stratospheric ozone data for individual years from 1975 to 1997, where half of the trend was applied to the period 1975-1978. After 1997, the stratospheric ozone was assumed to change in proportion to the effective equivalent stratospheric chlorine (EESC) reported in appendix II of IPCC/TAR. For before 1975, the data of 1975 are repeatedly used.

In contrast to the situation in the stratosphere, tropospheric ozone tended to increase in the 20th century. An increase in the emission of ozone precursors such as NO<sub>x</sub>, CO, and volatile organic carbons (VOC) could have caused the increase in tropospheric ozone. Observation of tropospheric ozone in the 20th century did not cover the whole globe well and there are few long-term records over several decades. Therefore, the global distribution of tropospheric ozone in the 20th century was estimated using the 3-dimensional global chemical transport model CHASER (Sudo *et al.*, 2003b). CHASER calculated the tropospheric ozone mixing ratio from 1850 to 2000 at intervals of 10 years with the historical emissions of ozone precursors (based on Van Aardenne *et al.*, 2001), concentrations of well-mixed GHGs (cf. Fig. 2.4), sea surface temperature, and sea-ice extent (Rayner *et al.*, 2003). The mixing ratios for intermediate years are obtained by linear interpolation in time.

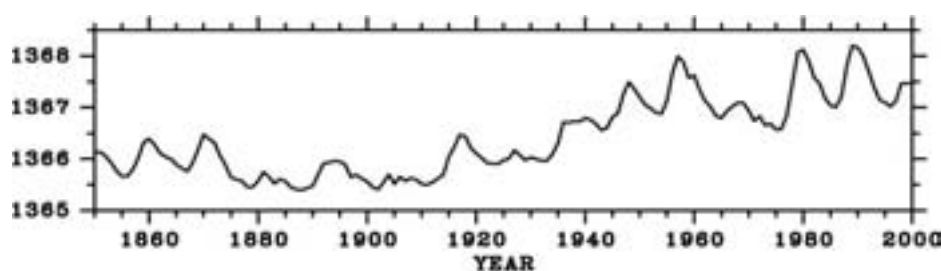
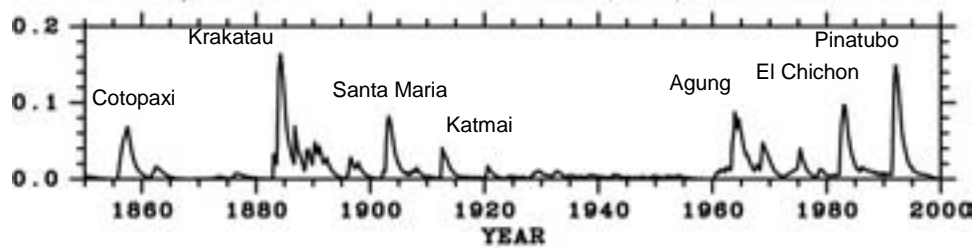
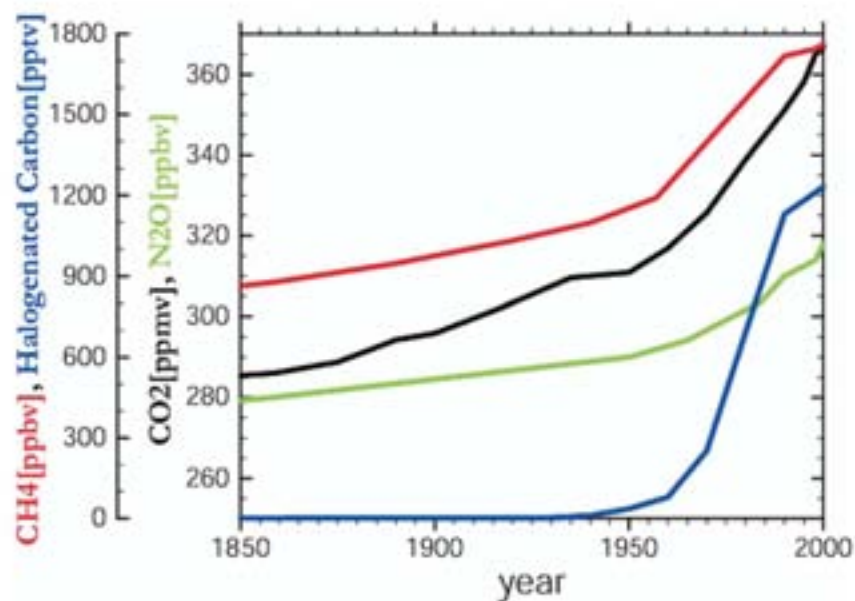


Fig. 2.2: Historical time series of total solar irradiance (TSI) from Lean *et al.* (1995a).



**Fig. 2.3:** Historical time series of monthly global mean volcanic aerosol optical thickness at 550 nm integrated in the lower to middle stratosphere compiled by Sato *et al.* (1993) and updated by Hansen *et al.* (2002).



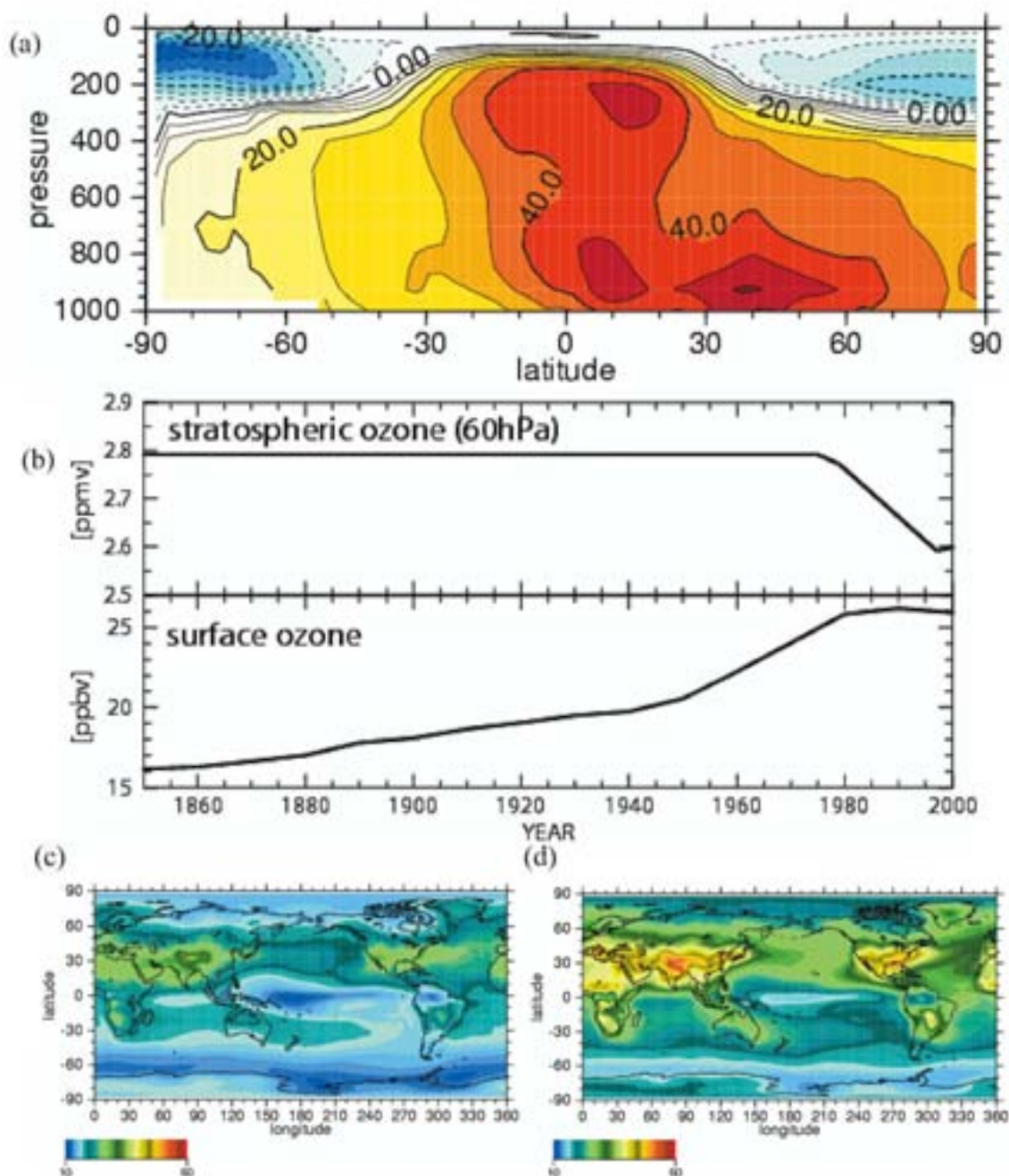
**Fig. 2.4:** Historical time series of global annual mean volume mixing ratios of well-mixed GHGs: CO<sub>2</sub> (black), N<sub>2</sub>O (green), CH<sub>4</sub> (red), and the sum of halocarbons (blue).

Fig. 2.5a shows the zonal mean change rate of the ozone mixing ratio over the whole model domain. While significant downward trends are seen in the high-latitude lower stratosphere, in particular in the southern hemisphere, tropospheric ozone generally increases with strong increases in the lower layer of the northern hemisphere and in the tropics. The global annual mean ozone in the lower stratosphere (approx. 60 hPa) and at the surface is shown in Fig. 2.5b. The stratospheric ozone bottoms out around 1997 then starts a faint recovery following the decrease in EESC. An over 70% increase in the ozone mixing ratio is calculated at the surface. Such an increase in the surface ozone is seen in remote areas, such as over ocean or polar regions, as well as in polluted areas in the northern mid-latitude (Figs. 2.5c and 2.5d).

Anthropogenic SO<sub>2</sub> emissions are created based on the country-based emission inventory of Lefohn *et al.* (1999). This dataset is the estimation of annual SO<sub>2</sub> emissions from industry (e.g. metal extraction) and fossil fuel consumption from 1850 to 1990. This country-based inventory is allocated to globally evenly distributed grids (0.5° × 0.5°) with the aid of global population data from the History Database of the Global Environment (HYDE; Klein



Goldewijk, 2001) and the Center for International Earth Science Information Network (CIESIN; CIESIN, 2005). This gridded dataset is then converted to the horizontal resolution of the atmospheric model ( $2.8^\circ$ ). Fig. 2.6 illustrates the change of horizontal distributions of  $\text{SO}_2$  emission from the early to the late 20th century. Except for the polar regions in both hemispheres,  $\text{SO}_2$  emission generally increases everywhere on land, especially in China, Eastern Europe, Turkey, India, and South Africa. An increase in  $\text{SO}_2$  emission from navigation over the northern Pacific and Atlantic Oceans is also seen in Fig. 2.6.



**Fig. 2.5: (a) Zonal mean change in ozone (%) from the 1901-1915 mean to the 1986-2000 mean. (b) Historical time series of global annual mean ozone mixing ratio at circa 60 hPa (upper) and at the surface (lower). Horizontal distributions of the ozone mixing ratio (ppbv) at the surface averaged over (c) 1901-1915 and (d) 1986-2000.**



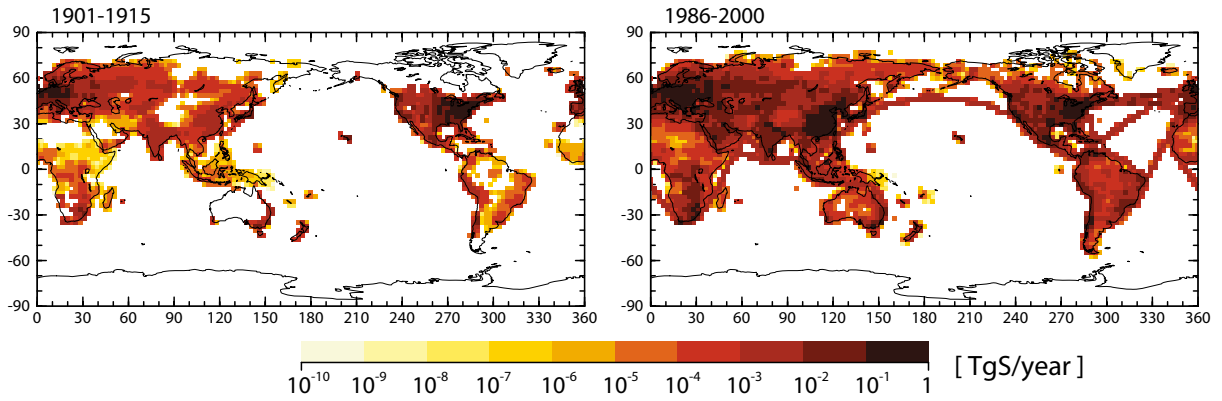


**Fig. 2.6: Horizontal distributions of SO<sub>2</sub> emissions from anthropogenic sources (TgS/year) averaged over 1901-1925 (left) and 1986-2000 (right).**

The country-based emissions of BC from 4 categories of anthropogenic sources, namely fossil fuel combustion, domestic fuelwood consumption, agricultural waste combustion, and biomass burning, were estimated from 1850 to 2000, and were gridded following the same method as SO<sub>2</sub> (Nozawa and Kurokawa, 2007). Except for biomass burning, country-based emissions were estimated by using the emission factor method with energy consumption statistics from organizations such as the Food and Agriculture Organization of the United Nations (FAO) and the International Energy Agency (IAE). On the other hand, the historical emission level of BC from biomass burning is highly uncertain; therefore, we estimated it assuming that its spatial distribution in the mid-1980s (Cooke and Wilson, 1996) is unchanged time-wise, but that its value scales with historical world population data (HYDE and CIESIN). This assumption is valid to a first-order approximation because a large part of the biomass burning that occurs in the tropics is relevant to agricultural activities that are normally traditional and indigenous. This implies that the regions in which biomass burning occurs may not have changed dramatically during the 20th century. Note that these data have the apparent defect of lacking emissions from China. The emission of OC is represented by multiplying BC emission by the ratio of OC to BC (OC/BC), which have different values reflecting the different burning conditions for each source. For example, a large OC/BC value (8.28) is applied to incomplete burning such as biomass burning of a tropical rain forest, while a small value (3.33) is applied to relatively complete burning such as fossil fuel combustion. Fig. 2.7 shows the changes in the horizontal distributions of BC emission from each anthropogenic source in the 20th century. The emission of BC from each source shows a distinct increase in the 20th century. The increase of BC emission due to fossil fuel combustion is significant in almost all land areas. In addition, there is large contribution of biomass burning in the low latitude regions.

Figs. 2.8a and 2.8b show the globally integrated emissions of SO<sub>2</sub> and BC, respectively. All emission time series show a rapid increase during the 20th century, although the emissions of SO<sub>2</sub> and BC from fossil fuel combustion do not increase so much in the last couple of decades.

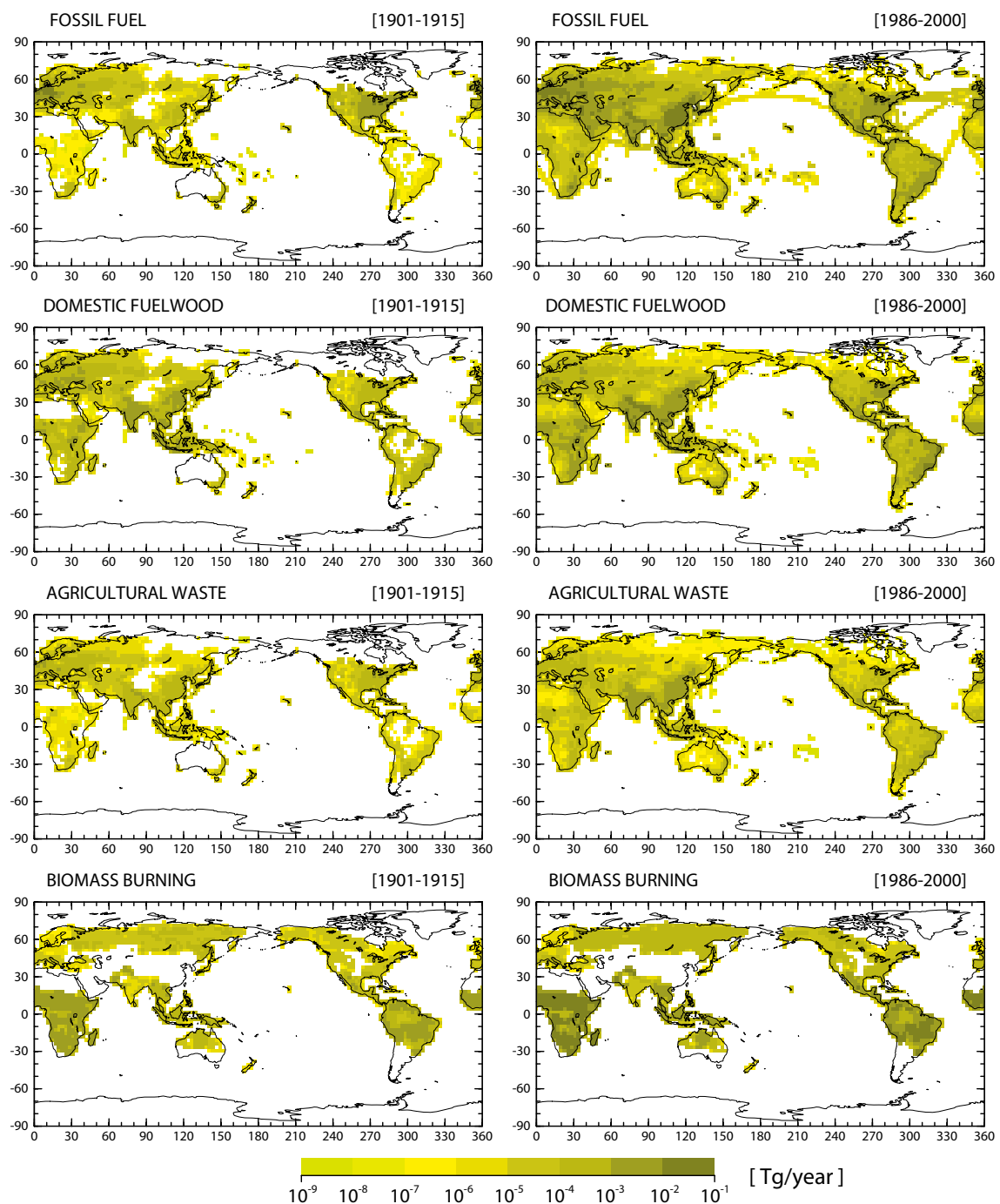


**Fig. 2.7: Horizontal distributions of black carbon aerosol emissions from fossil fuel combustion (first row), domestic fuelwood consumption (second row), agricultural waste combustion (third row), and biomass burning (4th row) in TgS/year averaged over 1901-1925 (left column) and 1986-2000 (right column).**

We used an estimation of the change in land use, actually the increase of crop area, in the 20th century (Hirabayashi *et al.*, 2005). These data backcasted historical crop area starting from current land-use data (U.S. Geological Survey, 2003) with the aid of historical global

crop ratio data from 1700 to 1992 (Ramankutty and Foley, 1999). Grids that were backcasted not to be crop were converted to potential vegetation classifications based on Ramankutty and Foley (1999) data. LAI data were adjusted to the historical change in crop area mentioned above.

Besides the experiment above, which considered all the climate forcing agents, we have performed 9 other experiments that were forced with a partial set of climate forcing agents. The combinations of climate forcing agents used for each experiment are listed in Table 2.2. These combinations were selected to isolate the effect of a particular set of forcing agents on the 20th century climate by comparing experiments with and without the set. For example, while global warming in the late 20th century can be reproduced in FULL and ANTH, it cannot be reproduced in NTRL (not shown). This strongly demonstrates the considerable effect of anthropogenic climate forcing agents on global warming in the late 20th century. All of the experiments consist of 4 ensemble members starting from different initial conditions taken from CONT at intervals of 100 years.

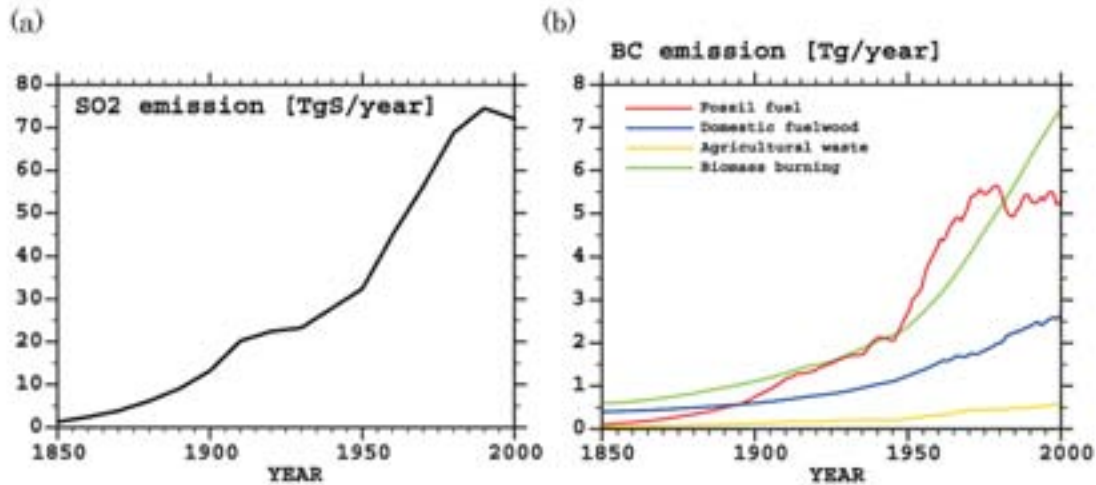


**Fig. 2.8: Historical time series of globally integrated emissions of (a)  $\text{SO}_2$  (TgS/year) and (b) black carbon aerosols from each source (Tg/year).**

**Table 2.2: Combinations of climate forcing agents for each experiment.** Agents marked “O” were considered in the experiment and those marked “X” were not

exp. name	natural		anthropogenic				
	solar	volcano	GHGs	ozone	$\text{SO}_2$	BC/OC	Land-use
FULL	O	O	O	O	O	O	O
NTRL	O	O	X	X	X	X	X
SOLR	O	X	X	X	X	X	X
VLCN	X	O	X	X	X	X	X
ANTH	X	X	O	O	O	O	O
GHGS	X	X	O	X	X	X	X
OZON	X	X	X	O	X	X	X
ARSL	X	X	X	X	O	O	X
AEFX	O	O	O	O	X	X	O
CEFX	O	O	O	O	O	X	O

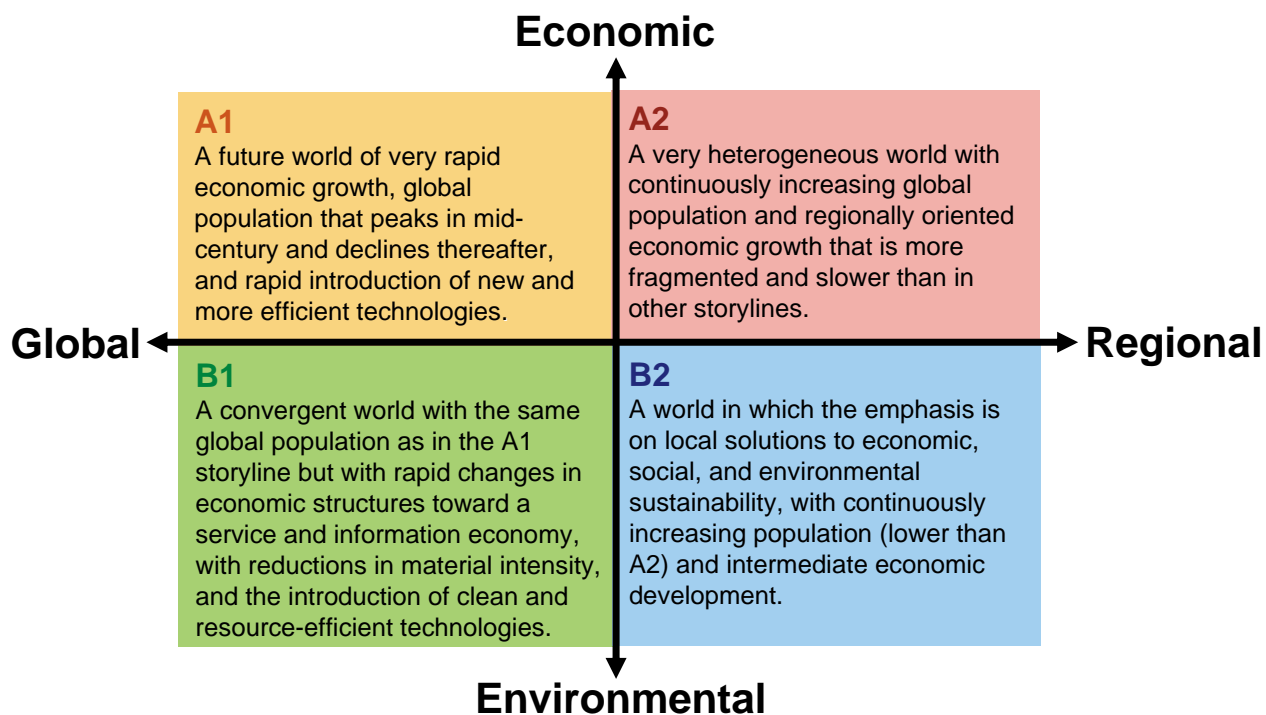
### 2.2.5 21st Century Simulation

To make a future climate projection, it is necessary, if possible, to estimate the quantitative change of climate forcing agents in the future and input them into a climate model. For such needs, IPCC has prepared future estimations of the anthropogenic emissions of GHGs and precursors of aerosols and ozone (Special Report on Emissions Scenarios (SRES); IPCC, 2000). The time evolutions of emissions in the future are estimated based on several potential scenarios of future development of the global society: these scenarios are called SRES scenarios. There are 4 scenarios (or more correctly, scenario families); each represents 1 of the 4 quadrants in Fig. 2.9. The A1 scenario family is further divided into 3 scenarios, A1B, A1FI, and A1T, depending on the source of energy used to drive this expanding economy. A1FI intensively uses fossil fuels and A1T uses new technologies based on renewable energy sources rather than fossil fuels, while A1B makes a point of balance between both energy sources. We made projections of the climate into the 21st century using 3 distinct scenarios: A1B, A2, and B1. Besides these 3 SRES scenarios, we also performed an experiment with all climate forcing agents held fixed at values corresponding to the year 2000 during the entire 21st century (committed scenario). For the A1B and B1 scenarios, the experiments have been extended to the year 2200 with all climate forcing agents kept fixed at year 2100 values during the entire 22nd century. The experiments under the 3 SRES scenarios consist of 3 ensemble members starting from the year 2000 that are taken from different members of the 20th century simulation. Only 1 run was performed for the committed scenario and extension of A1B and B1.

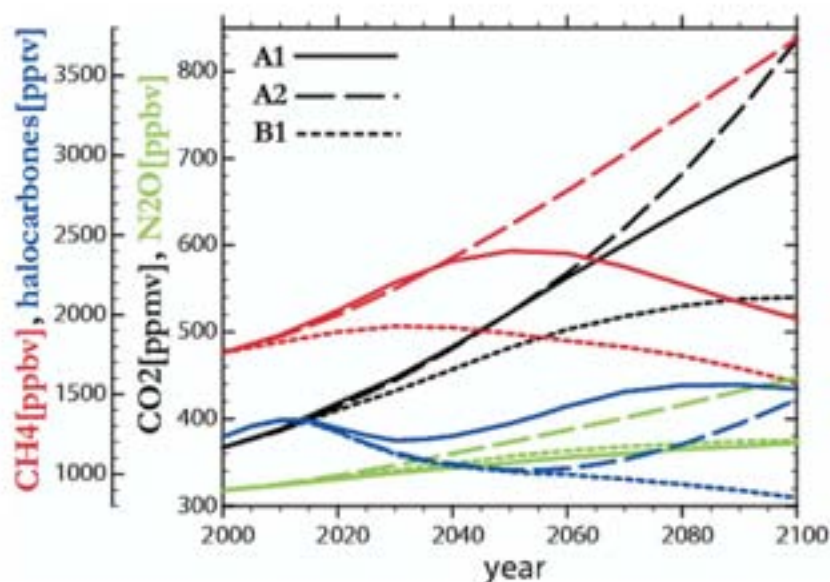
The temporal evolution of global annual mean well-mixed GHGs for each scenario are shown in Fig. 2.10. The highest amounts of CO<sub>2</sub>, CH<sub>4</sub>, and N<sub>2</sub>O are achieved in the A2 scenario, which also continues to grow.

Fig. 2.11 shows the globally integrated emissions of SO<sub>2</sub> (Fig. 2.11a) and BC from respective sources (Fig. 2.11b). Regardless of the scenario, SO<sub>2</sub> emission in the 21st century is estimated to peak in the early half of the century and continue to decrease after that.

Similar to the stratospheric ozone after 1997 in the 20th century simulation, we assumed that stratospheric ozone recovers in proportion to the decrease of EESC reported in appendix II of IPCC/TAR. The same stratospheric ozone data are used in the 3 SRES scenario experiments. The chemical transport model CHASER was used to estimate the future evolution of the tropospheric ozone corresponding to each scenario (Kawamiya *et al.*, 2005). CHASER calculated the tropospheric ozone mixing ratio from 2000 to 2100 at intervals of 10 years with the emissions of ozone precursors and the concentrations of well-mixed GHGs projected in each SRES scenario, and the sea surface temperature and the sea-ice extent projected in our preceding experiments performed for the IPCC/TAR (Emori *et al.*, 1999; Nozawa *et al.*, 2001). The mixing ratios for intermediate years are obtained by linear interpolation in time. Fig. 2.12 shows the global annual mean ozone in the lower stratosphere (approx. 60 hPa) and at the surface for each SRES scenario. Only the A2 scenario shows a continuous increase in the surface ozone. The increase of the surface ozone is mainly influenced by the increase in emission of ozone precursors, but there is some impact from the change in the transport of ozone between the stratosphere and the troposphere due to the increase of GHGs and the consequent change in atmospheric circulation (Sudo *et al.*, 2003a; Kawamiya *et al.*, 2005)



**Fig. 2.9: Schematic illustration of the 4 SRES scenario families.** The short summaries of the scenarios are taken from IPCC (2000).



**Fig. 2.10: Temporal evolution of global annual mean volume mixing ratios of well-mixed GHGs:** CO<sub>2</sub> (black), N<sub>2</sub>O (green), CH<sub>4</sub> (red) and the sum of halocarbons (blue) for A1B (solid lines), A2 (dashed lines), and B1 (dotted lines) scenarios.

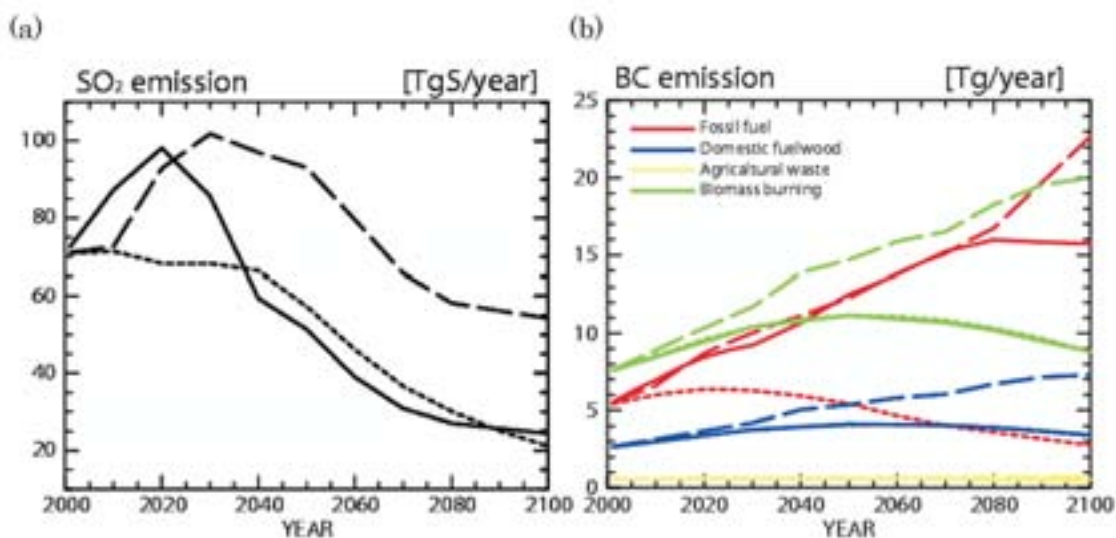


**Fig. 2.11: Temporal evolution of globally integrated emissions of (a) SO<sub>2</sub> (TgS/year) and (b) black carbon aerosols from each source (Tg/year).** In both figures, the A1B case (solid lines), A2 case (dashed lines), and B1 case (dotted lines) are shown.

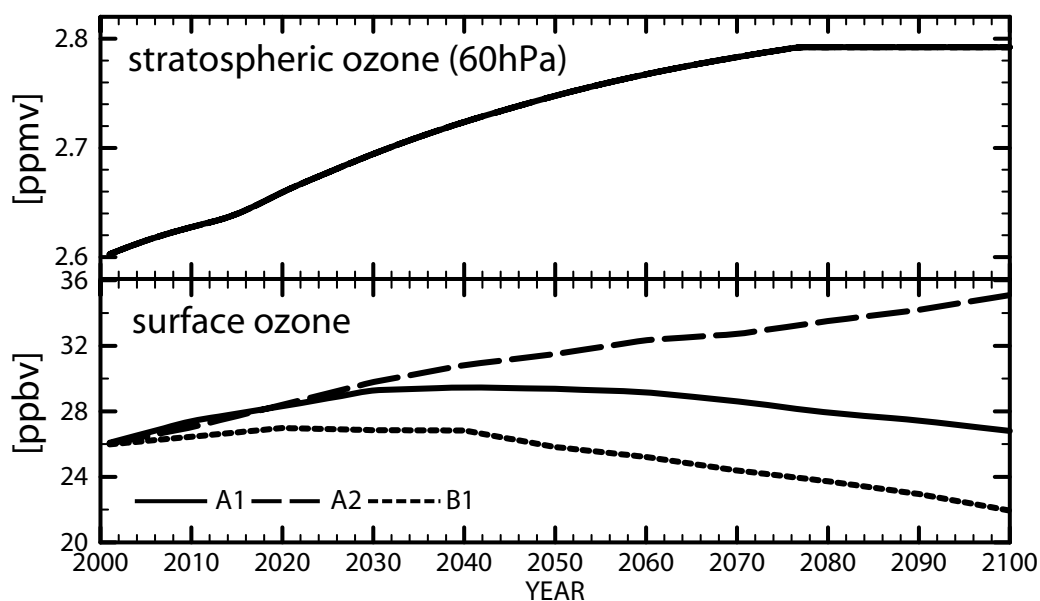


**Fig. 2.12: Temporal evolution of the global annual mean ozone mixing ratio at circa 60 hPa (upper) and at the surface (lower).** The A1B (solid lines), A2 (dashed lines), and B1 (dotted lines) cases are shown. Note that in the stratosphere the same ozone data are used for each scenario.

## References

- Center for International Earth Science Information Network (CIESIN), Columbia University; and Centro Internacional de Agricultura Tropical (CIAT) (2005) Gridded Population of the World Version 3 (GPWv3): Population Grids. Available at <http://sedac.ciesin.columbia.edu/gpw>.
- Cooke, W.F., Wilson, J.J.N. (1996) A global black carbon aerosol model. *J. Geophys. Res.*, 101, 19395-19409.
- Covey, C., AchutaRao, K.M., Cubasch, U., Jones, P., Lambert, S.J., Mann, M.E., Phillips, T.J., Taylor, K.E. (2003) An overview of results from the Coupled Model Intercomparison Project (CMIP). *Global and Planetary Change*, 37, 103-133.
- Emori, S., Nozawa, T., Abe-Ouchi, A., Numaguti, A., Kimoto, M., Nakajima, T. (1999) Coupled ocean-atmosphere model experiments of future climate change with an explicit representation of sulfate aerosol scattering. *J. Meteor. Soc. Japan*, 77, 1299-1307.
- Foukal, P., North, G., Wigley, T. (2004) A Stellar View on Solar Variations and Climate. *Science*, 306, 68-69.
- Hansen, J., Sato, M., Nazarenko, L., Ruedy, R., Lacis, A., Koch, D., Tegen, I., Hall, T., Shindell, D., Santer, B., et al. (2002) Climate forcings in Goddard Institute for Space Studies SI2000 simulations. *J. Geophys. Res.*, 107, D18, 4347, doi:10.1029/2001JD001143.
- Hasumi, H. (2000) CCSR Ocean Component Model (COCO) Version 2.1. CCSR Report, 13, 68pp.
- Hirabayashi, Y., Struthers, I., Kanae, S., Oki, T. (2005) A 100-year (1901-2000) global retrospective estimation of terrestrial water cycle. *J. Geophys. Res.*, 110, D19, doi:10.2029/2004JD005492.
- IPCC (2000) Special Report on Emission Scenarios, Nakicenovic, N., Swart, R. (eds.), Cambridge University Press, Cambridge, UK, 612pp.
- IPCC (2001) Climate Change 2001: The Scientific Basis. Contribution of Working Group I to the Third Assessment Report of the Intergovernmental Panel on Climate Change, Houghton, J.T., Ding, Y., Griggs, D. J., Noguer, M., van der Linden, P.J., Dai, X., Maskell, K., Johnson, C.A. (eds.), Cambridge University Press, Cambridge, United Kingdom and New York, NY, USA, 881pp.
- Johns, T.C., Gregory, J.M., Ingram, W.J., Johnson, C.E., Jones, A., Lowe, J.A., Mitchell, J.F.B., Roberts, D.L., Sexton, D.M.H., Stevenson, D.S., et al. (2003) Anthropogenic climate change for 1860 to 2100 simulated with the HadCM3 model under updated emissions scenarios. *Clim. Dyn.*, 20, 583-612.
- K-1 model developers (2004) K-1 coupled GCM (MIROC) description, K-1 technical report. 1, Hasumi, H., Emori, S. (eds.), Center for Climate System Research, University of Tokyo, Tokyo, 34pp.
- Kawamiya, M., Yoshikawa, C., Kato, T., Sato, H., Sudo, K., Watanabe, S., Matsuno, T. (2005) Development of an Integrated Earth System Model on the Earth simulator. *J. Earth Sim.*, 4.
- Klein Goldwijk, K. (2001) Estimating global landuse change over the past 300 years: The HYDE Database. *Global Biogeochem. Cycles*, 15, 417-433.
- Lean J., Beer, J., Bradley, R. (1995a) Reconstruction of solar irradiance since 1600: Implications for climate change. *Geophys. Res. Lett.*, 22, 3195-3198.
- Lean, J., White, O.R., Skumanich, A. (1995b) On the solar ultraviolet spectral irradiance during the Maunder Minimum. *Global Biogeochemical Cycles*, 9, 171-182.
- Lefohn, A.S., Husar, J.D., Husar, R.B. (1999) Estimating historical anthropogenic global sulfur emission patterns for the period 1850-1990. *Atmos. Environ.*, 33, 3435-3444.
- Nozawa, T., Kurokawa, J. (2007) Historical and future emissions of sulfur dioxide and black carbon for global and regional climate change studies. CGER-REPORT, Center for Global Environmental Research, National Institute for Environmental Studies, Tsukuba, in preparation.
- Nozawa, T., Emori, S., Numaguti, A., Tsushima, Y., Takemura, T., Nakajima, T., Abe-Ouchi, A., Kimoto, M. (2001) Projections of future climate change in the 21st century simulated by the CCSR/NIES CGCM under the IPCC SRES scenarios, in *Present and Future of Modeling Global Environmental Change toward Integrated Modeling*, Matsuno, T., Kida, H. (eds.), Terra Scientific Publishing, 15-28.
- Numaguti, A., Takahashi, M., Nakajima T., Sumi, A. (1997) Description of CCSR/NIES Atmospheric General Circulation Model. CGER's Supercomputer Monograph Report, Center for Global Environmental Research. National Institute for Environmental Studies, No. 3, 1-48.
- Ogura, T., Emori, S., Tsushima, Y., Yokohata, T., Abe-Ouchi, A., Kimoto, M. (2007) Climate sensitivity of a general circulation model with different cloud modelling assumptions. Submitted to *J. Meteor. Soc. Japan*.
- Oki, T., Sud, Y.C. (1998) Design of total runoff integrating pathways (TRIP) - a global river channel network. *Earth Interactions*, 2.
- Ramankutty, N., Foley, J.A. (1999) Estimating historical changes in global land cover: Croplands from 1700 to 1992. *Global Biogeochem. Cycles*, 13, 997-1027.
- Randel, W.J., Wu, F. (1999) A stratospheric ozone trends data set for global modeling studies. *Geophys. Res. Lett.*, 26, 3089-3092.



- Rayner N.A., Parker, D.E., Horton, E.B., Folland, C.K., Alexander, L.V., Rowell, D.P., Kent, E.C., Kaplan, A. (2003) Global analyses of sea surface temperature, sea ice, and night marine air temperature since the late nineteenth century. *J. Geophys. Res.*, 108 (D14), 4407, doi:10.1029/2002JD002670.
- Sato, M., Hansen, J.E.M., McCormick, P., Pollack, J.B. (1993) Stratospheric aerosol optical depths, 1850-1990. *J. Geophys. Res.*, 98, 22987-22994.
- Sudo, K., Takahashi, M., Akimoto, H. (2003a) Future changes in stratosphere- troposphere exchange and their impacts on future tropospheric ozone simulations. *Geophys. Res. Lett.*, 30, 2256, 10.1029/2003GL018526.
- Sudo, K., Takahashi, M., Kurokawa, J., Akimoto, H. (2003b) CHASER: A global chemical model of the troposphere 1. Model description. *J. Geophys. Res.*, 107, doi:10.1029/2001JD001113.
- Takata, K., Watanabe, T., Emori, S. (2003) Development of the minimal advanced treatments of surface interaction and runoff. *Global and Planetary Change*, 38, 209-222.
- Takemura, T., Okamoto, H., Maruyama, Y., Numaguti, A., Higurashi A., Nakajima, T. (2000) Global three-dimensional simulation of aerosol optical thickness distribution of various origins. *J. Geophys. Res.*, 105, 17,853-17,873.
- Takemura, T., Nakajima, T., Dubovik, O., Holben, B.N., Kinne, S. (2002) Single-scattering albedo and radiative forcing of various aerosol species with a global three-dimensional model. *J. Climate*, 15, 333-352.
- U.S. Geological Survey (2003) Global land cover characteristics database. Sioux Falls, SD (available at [http://LPDAAC.usgs.gov/glcc/globdoc2\\_0.html](http://LPDAAC.usgs.gov/glcc/globdoc2_0.html)).
- Van Aardenne, J., Dentener, J.F., Olivier, J.G.J., Klein Goldewijk, C.G.M., Lelieveld, J. (2001) A 1° x 1° resolution dataset of historical anthropogenic trace gas emissions for the period 1890–1990. *Global Biogeochemical Cycles*, 15(4), 909-928.
- Wang, W.-C., Liang, X.-Z., Dudek, M.P., Pollard, D., Thompson, S.L. (1995) Atmospheric ozone as a climate gas. *Atm. Res.*, 37, 247-256.





## Chapter 3: Simulated Climate States in the Control Experiment

In the present section, the characteristics of the control simulation (the external condition in the model simulation is the year 1850) are described. The simulations of the control experiment were integrated over more than 3000 years. Our contention is that the climate states simulated in the control experiment are very stable (no significant climate drift in the control simulation) and realistic. Here, we describe the time evolution, mean state, and variability of the climate system in the control experiment.

### 3.1 Time Evolution of the Climate System

The time evolution of the important factors in the climate system is shown in Fig. 3.1. The surface air temperature (SAT) is shown to be extremely stable during the integration (Fig. 3.1a). The climate drift in the first 500 years is less than  $0.1^{\circ}\text{C}$  per 100 years. The temperature in the ground (3 m soil temperature, Fig. 3.1b) is also stable during the integration.

The time evolution of the ocean temperature is shown in Fig. 3.2. The ocean temperature is relatively stable during the control integration. Although during the first 500 years the ocean temperature increases about  $0.1^{\circ}\text{C}$ , the rate of increase decreases after the year 500, to about  $0.05^{\circ}\text{C}$  per 1000 years. Then, the rate of increase of the ocean mean temperature decreases further after the year 1000. It is interesting to compare the time evolution of the ocean mean temperature (Fig. 3.2a) with that of the vertical profile of the ocean temperature (Fig. 3.2b). In the upper layer (above about 1000 m depth), the ocean temperature changes only at the beginning of the integration (until about the year 1000) and then does not change during the latter part of the integration. On the other hand, in deeper layers, the ocean temperature continues to increase gradually during the whole term of the integration. These results reflect the fact that the time for a deeper ocean layer to achieve an equilibrium state is much longer than for the upper ocean layer. Therefore, it can be assumed that the small increasing rate of the ocean mean temperature during the latter half of the integration (Fig. 3.1) is caused by a temperature increase in the deeper layer after the upper layer has achieved equilibrium.

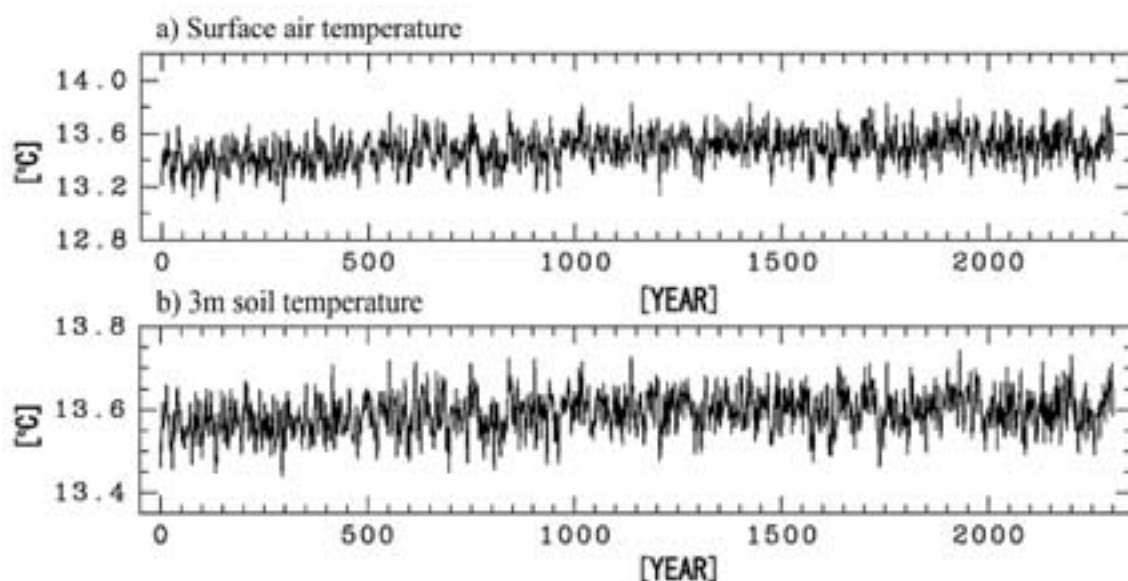


**Fig. 3.1:** Time series of globally averaged a) surface air temperature, b) 3m soil temperature. Annually averaged data are used for the plot.

The time evolution of North Atlantic deep water (NADW) is shown in Fig. 3.2c. Like the atmospheric and ocean temperatures, the strength of NADW is stable during the integration. It is interesting to note that a centennial variability (with a time scale of about a few hundred years) can be seen in the time sequence of NADW (Oka *et al.*, 2006). Since this feature cannot be seen in the time sequence of SAT (Fig. 3.1a), this variability must be related to variability in ocean circulation, as suggested by Vellinga and Wu (2004) by using another climate model.

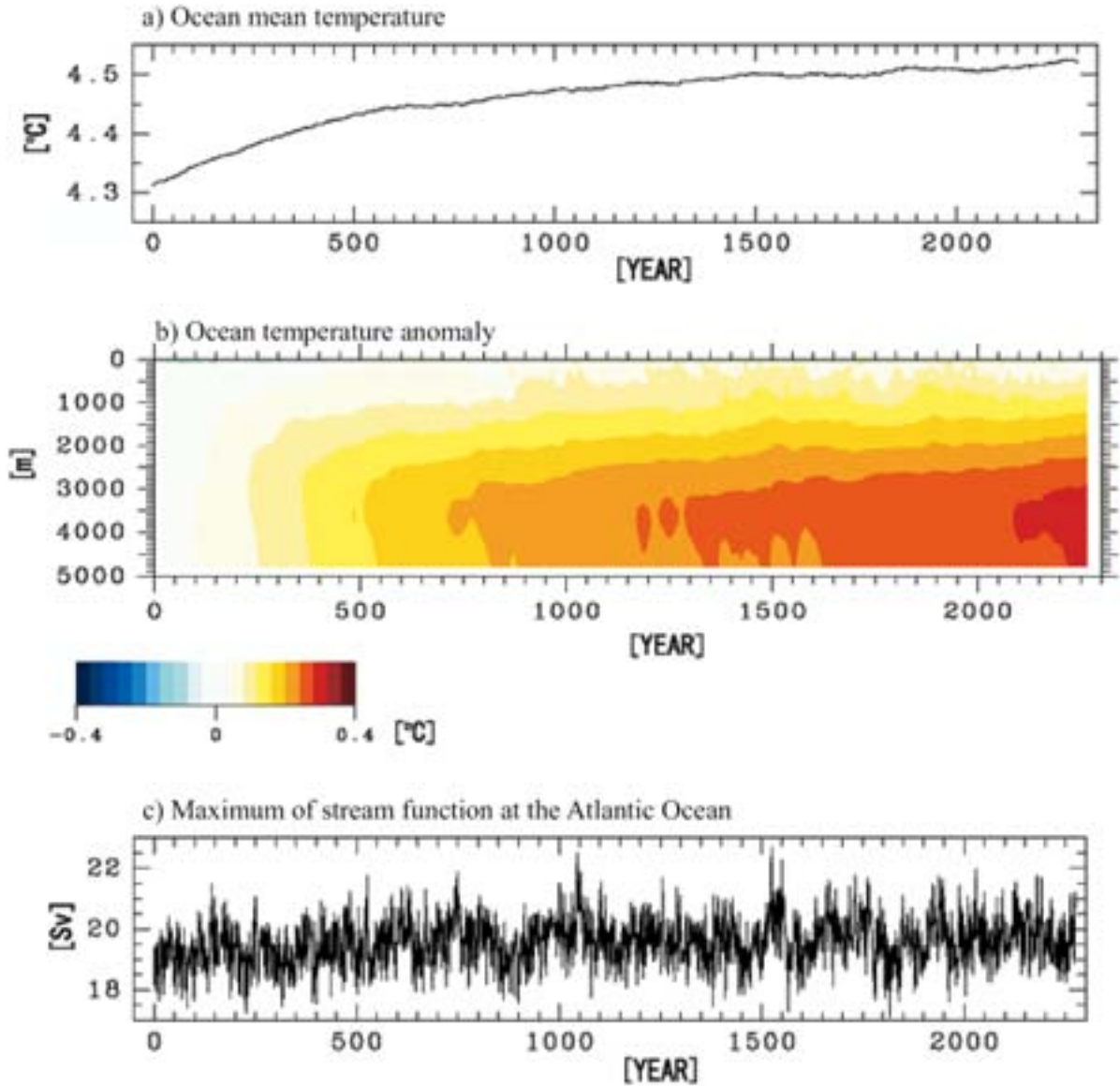


**Fig. 3.2:** Time series of globally averaged a) ocean mean temperature, b) ocean temperature anomaly (taking first 20-year average as a baseline), and c) maximum of stream function of North Atlantic deep water (NADW). Annually averaged data are used for a) and c), and 10-year averaged data are used for b).

### 3.2 Mean States of the Climate System

The mean states of the model simulation and their biases (differences between model result and observation) are presented in this section. All the figures of the model simulation presented in this subsection (Figs. 3.3 to 3.8) show 30-year averaged data from the time when the simulated climate state had reached equilibrium. Global maps of simulated variables and their biases are shown in Figs. 3.3 to 3.5. In general, our model simulation is sufficiently realistic compared to other climate models (e.g., Johns *et al.*, 2006, Delworth *et al.*, 2006, Gnanadesikan *et al.*, 2006, Yukimoto *et al.*, 2006).

Results for SAT and sea surface temperature (SST) are shown in Fig. 3.1. Observational data are obtained from a dataset by the European Centre for Medium-Range Weather Forecasts Re-analysis ERA-40 (Uppala *et al.*, 2005) for SAT and from Met Office HadISST 1.1 (Rayner *et al.*, 2003) for SST. For the observations, 30-year averages from the years 1971 to 2000 were chosen for analysis. Overall, temperatures near the surface, SAT and SST, are relatively low compared to the observations (Figs. 3.3b and 3.3d). SAT and SST are lower than the observations in the Pacific, Atlantic, and Indian Oceans. Cooling bias is also large in the Arctic Ocean, the northern part of the Eurasian continent, and the Antarctic. On the other hand, there is warming bias around Antarctica. This is possibly because the extent of sea ice is insufficient in these areas (Yokohata *et al.*, 2007). In addition, warming bias also can be seen around the Caspian Sea, where the surface is covered by desert. It is interesting to note that the bias of SAT is larger than that of SST. This could be because SAT has larger temperature variability than SST, and the simulated temperature variability is not large enough compared to observation (examples can be seen in the next section).

Precipitation from the model simulation and comparison to observations by the Climate Prediction Center's Merged Analysis of Precipitation (CMAP, Xie and Arkin, 1997) are also shown in Fig. 3.3. In the equatorial zone of the Pacific Ocean, double InterTropical Convergence Zones (ITCZ) exist. This is a feature typically simulated in an atmosphere-ocean CGCM, but it is not observed in the real world (e.g., Zhang, 2001). In addition, precipitation in the model is less than observation in the South Pacific Convergence Zone (SPCZ, e.g., Vincent, 1994). This feature could be related to the SST bias (Fig. 3.3d), although the locations of the maxima in the SST and precipitation biases do not precisely agree. Positive bias (more precipitation than the observation) can be seen in the Southern Ocean, which could be related to the bias in the sea surface pressure (not shown), and offshore of Peru, which could be related to the bias of SST (Fig. 3.3d). Positive bias can also be seen at the western coasts of Central Africa and Southeast Asia, which is related to the simulated Indian and Asian monsoons, respectively.

Fig. 3.4 shows sea ice concentration of the model simulation and observation (Rayner *et al.*, 2003). In the northern hemisphere, the simulated concentration is very realistic in both the winter and summer seasons. Although the distribution of sea ice concentration is slightly different between simulation and observation (for example, the simulation tends to have higher concentration near coasts), they are in good agreement with each other. On the other hand, simulated sea ice in the southern hemisphere seems to be less than the real world in the winter and summer seasons. In the model simulation, the concentration is less than observation especially in the Weddell and Ross Seas.

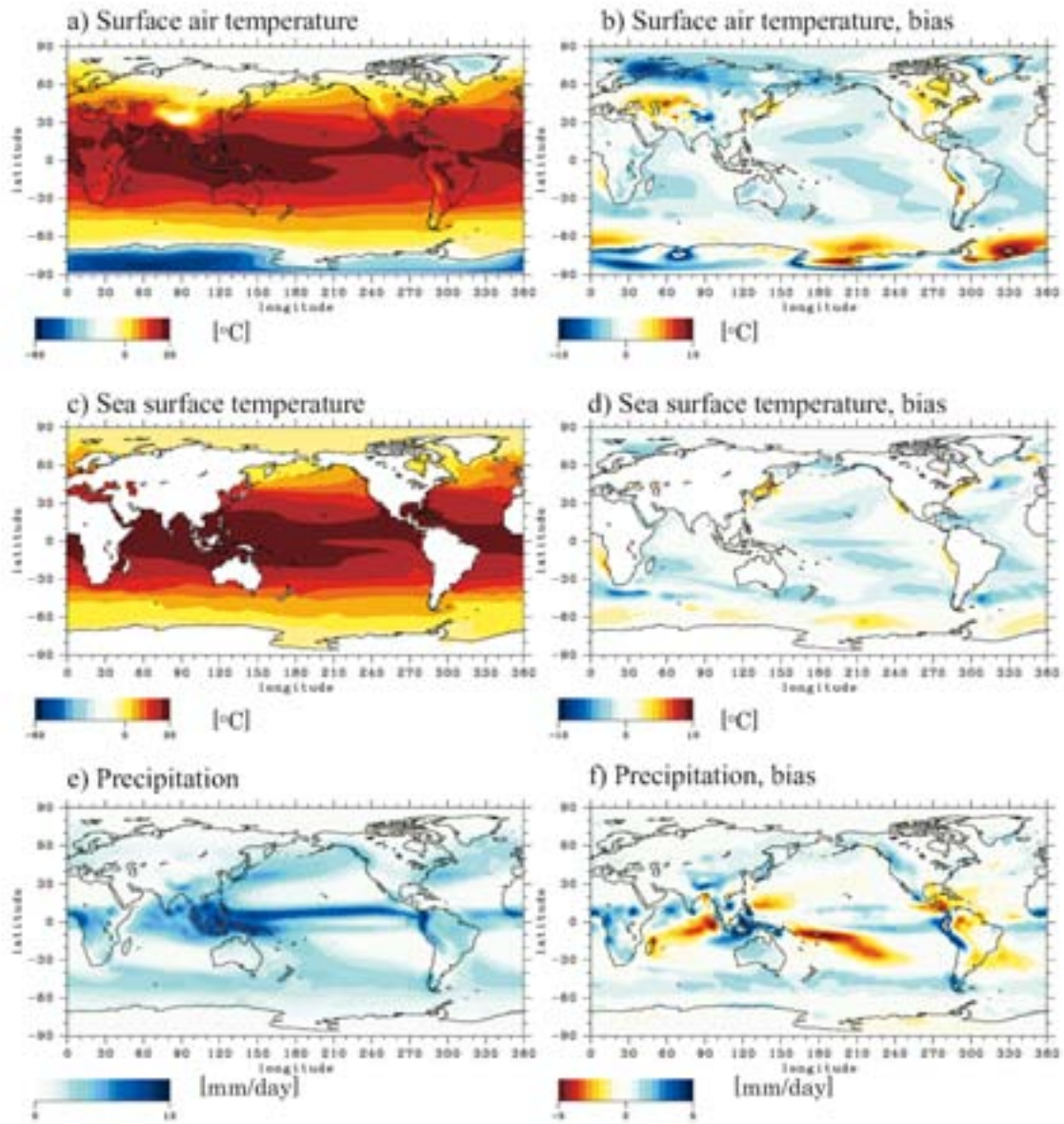


**Fig. 3.3:** Global map of the model simulation (left column) and the difference from observation (right column) for a-b) surface air temperature, c-d) sea surface temperature, and e-f) precipitation.

The shortwave (SW) and longwave (LW) radiation at the top of the atmosphere (TOA), and their cloud radiative forcing (CRF), are shown in Figs. 3.5 and 3.6, respectively. Observational data from the Earth Radiation Budget Experiment (ERBE), Earth Radiant Fluxes and Albedo for Month (S-9), from the years 1985 to 1989 (Barkstrom *et al.*, 1989), are used for comparison with the model simulation. For all the variables shown in Figs. 3.5 and 3.6, positive is defined in the downward direction; thus a positive bias would cause more warming compared to the real world. A very large negative bias in the SW radiation can be seen at low to mid-latitudes in the central Pacific, western Atlantic, and Indian Oceans (Fig. 3.5). Since the bias in SW CRF has a similar magnitude, the bias in SW radiation could be caused by the cloud bias in the model simulation. In addition, offshore of Peru and California



there are positive biases in SW radiation and SW CRF, and thus the simulated cloud amount is not enough compared to the real world. On the other hand, especially around Antarctic, a positive bias can be seen in SW CRF that cannot be seen in SW radiation. We should be careful when examining the bias in SW CRF at high latitude, since it can include biases in non-cloud components, such as a bias in the surface SW reflection (e.g., Yokohata *et al.*, 2005a and 2005b).

In general, the bias is relatively small for LW radiation compared to SW radiation. In the equatorial Pacific, where the double ITCZ exists, a positive bias in LW radiation and LW CRF can be seen. Since these features of the LW biases are similar to those of the precipitation bias, these two biases are related. Because convection would occur in the equatorial Pacific more frequently or strongly in the model simulation compared to the real world, effective LW emissivity in these areas should become higher, and thus cause the positive LW biases. Similarly, the negative biases in the LW radiation and LW CRF in the SPCZ could be related to the negative precipitation bias there.

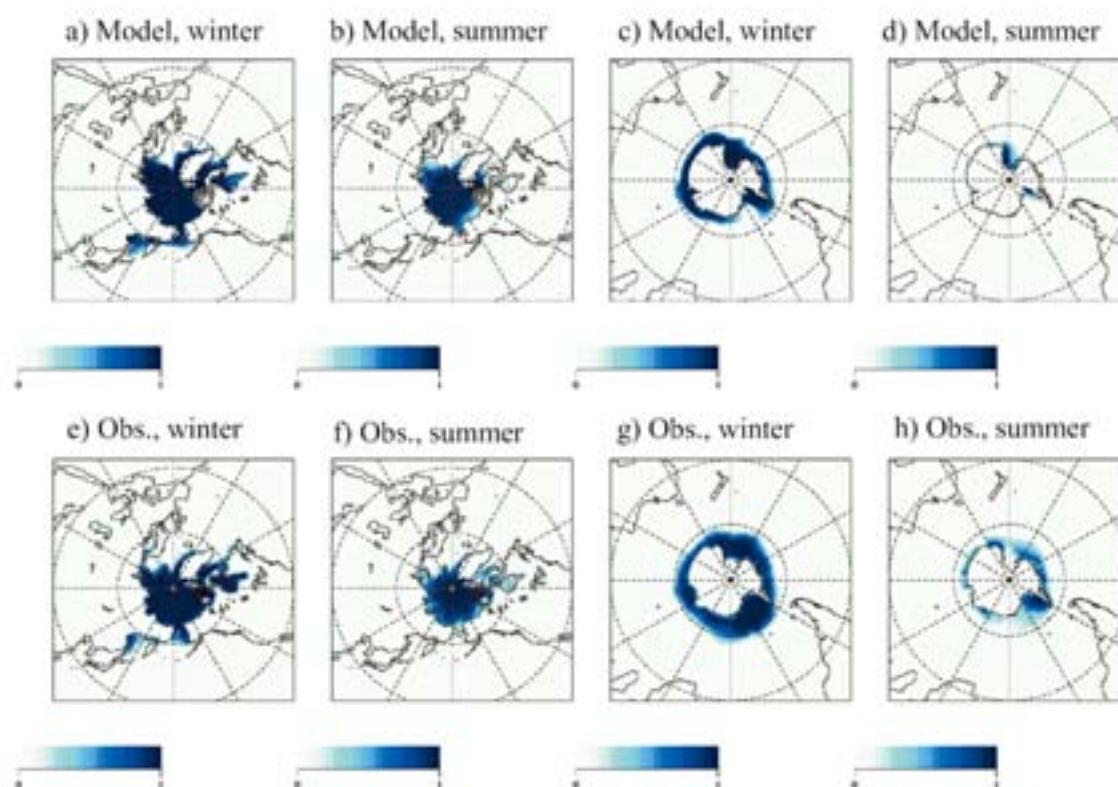


**Fig. 3.4: Sea-ice concentration of the model simulation (upper column) and observation (lower column).** Data from December to February are used for the northern winter and southern summer, and from June to August for the northern summer and southern winter.

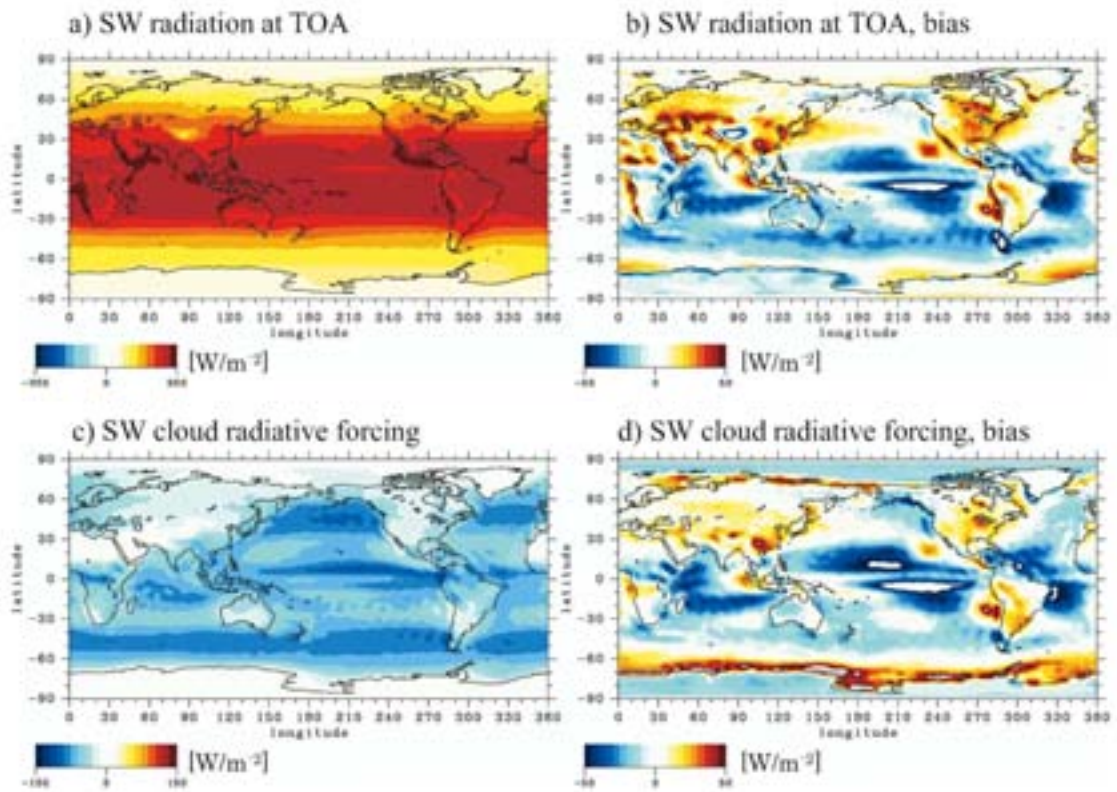


**Fig. 3.5:** Same as Fig. 3.3 but for the net downward a-b) shortwave (SW) radiation at top of the atmosphere (TOA) and c-d) SW cloud radiative forcing (CRF) at the TOA.

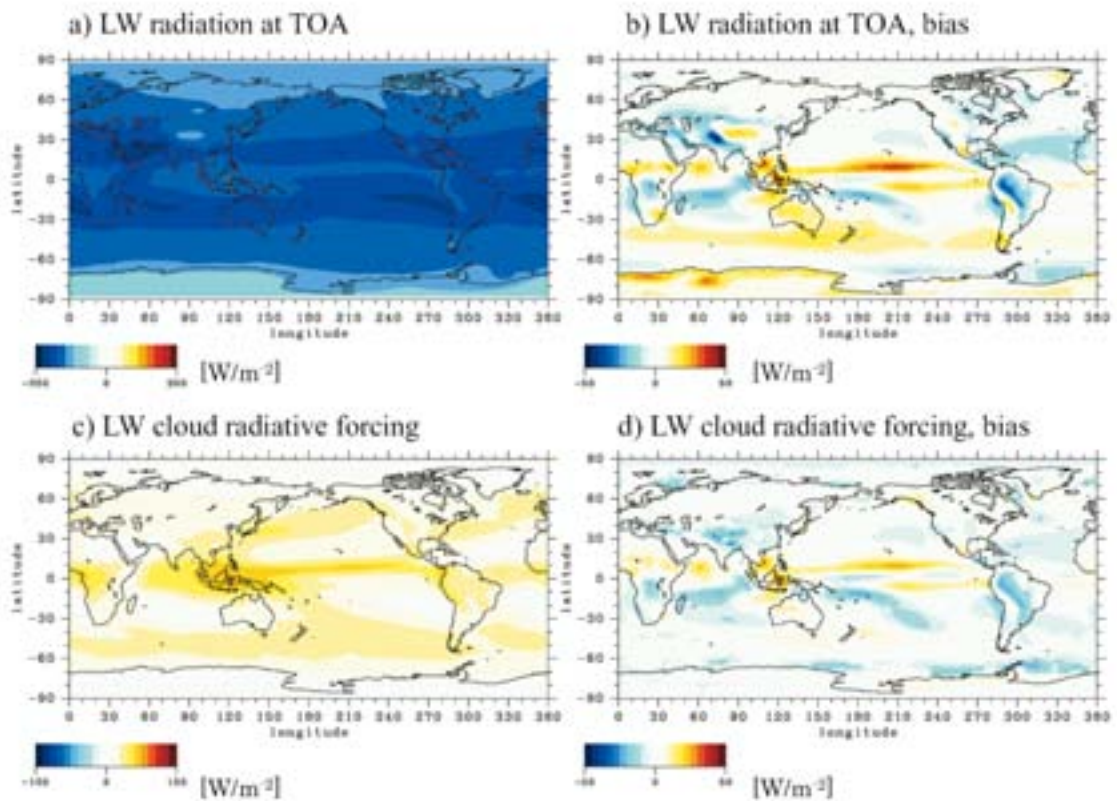


**Fig. 3.6:** Same as Fig. 3.5 but for the longwave (LW) radiation.

Vertical and latitudinal profiles of simulated and observed mean states are shown in Figs. 3.7 and 3.8. A cold bias in the atmospheric temperature can be seen near the surface except in the Southern Ocean (Figs. 3.7a and 3.7b). This is consistent with what we discussed regarding the results of the SAT bias. At higher altitudes, a cold bias can be seen in the middle troposphere (especially at low latitudes less than  $30^\circ$ ), and a large cold bias can be seen in the upper troposphere or stratosphere. In the southern hemisphere, a large cold bias in the upper troposphere extends downward to the lower troposphere, a feature similar to the zonal mean of zonal wind (details are explained in the description of transient climate response to atmospheric  $\text{CO}_2$  increase).

Results for specific and relative humidity are also shown in Fig. 3.7. A large negative (dry) bias can be found in the lower troposphere, especially at latitudes lower than  $30^\circ$  (Fig. 3.7d). Reasons for the dry bias in these regions are related to the cold bias (Fig. 3.7b) and the dry bias in the relative humidity (Fig. 3.7f). In the region where the dry bias in relative humidity is maximal, the dry bias in specific humidity is also maximal. In the upper troposphere and stratosphere, a large positive (wet) bias can be seen. This bias could cause the negative temperature bias (Fig. 3.7b) owing to an increase in LW emission into outer space.

The mean states of clouds are shown in Fig. 3.8. Cloud water (here defined as the sum of liquid and solid water) by cumulus convection exists at the tropics in the troposphere, with maximum latitude about  $10^\circ$  in the northern and southern hemispheres (Fig. 3.8a). The latitudinal region of this maximum in cumulus cloud water corresponds to that of the maximum in precipitation (Fig. 3.3). Another peak in cumulus cloud water can be seen in the latitudinal region from  $30^\circ$  to  $40^\circ$ , which could be caused by disturbances in the middle latitudes. Fig. 3.8b shows the cloud water by large-scale condensation (LSC). As discussed by Tsushima *et al.*, (2006), the differences in LSC cloud water among state-of-art climate models are considerably large, and thus understanding the mechanisms that determine the distributions of LSC clouds is very important. A large amount of LSC cloud water can be seen at an altitude around 900 hPa. In the tropics, LSC cloud water extends to a middle altitude of about 600 hPa. It is interesting to note that the vertical and latitudinal profile of the cloud fraction (Fig. 3.8c) is different from the cloud water distributions (Figs. 3.8a and 3.8b). A cloud fraction maximum can be found at extremely high altitudes ( $\sim 100$  hPa) in the tropics, and at the whole altitude layer in the troposphere over the middle-to-high latitudinal region. This large fraction at higher altitudes could be related to the formation of cirrus.



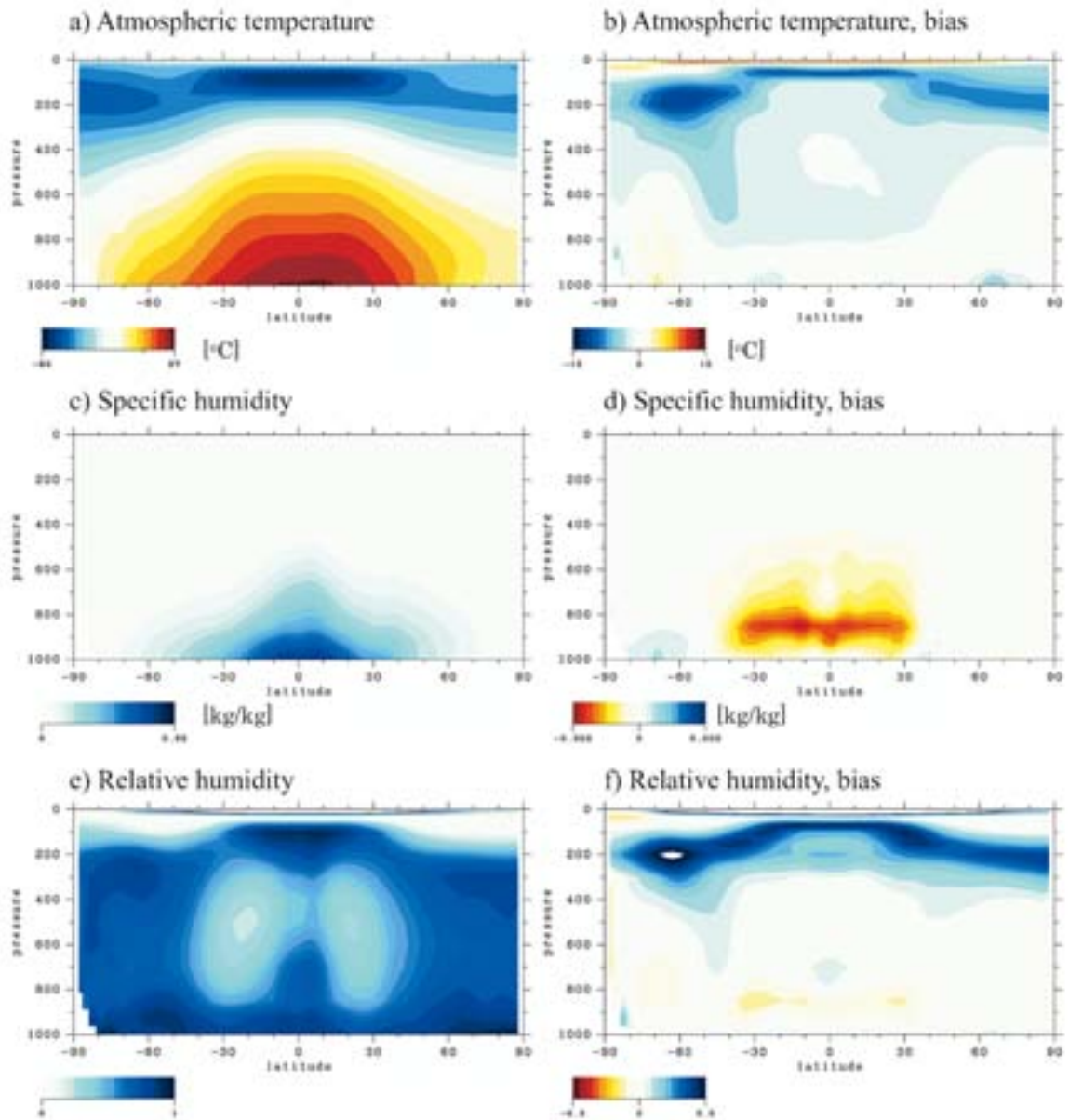


**Fig. 3.7:** Zonal mean of the model simulation (left column) and difference from observation (right column) for a-b) atmospheric temperature, c-d) specific humidity, and e-f) relative humidity.

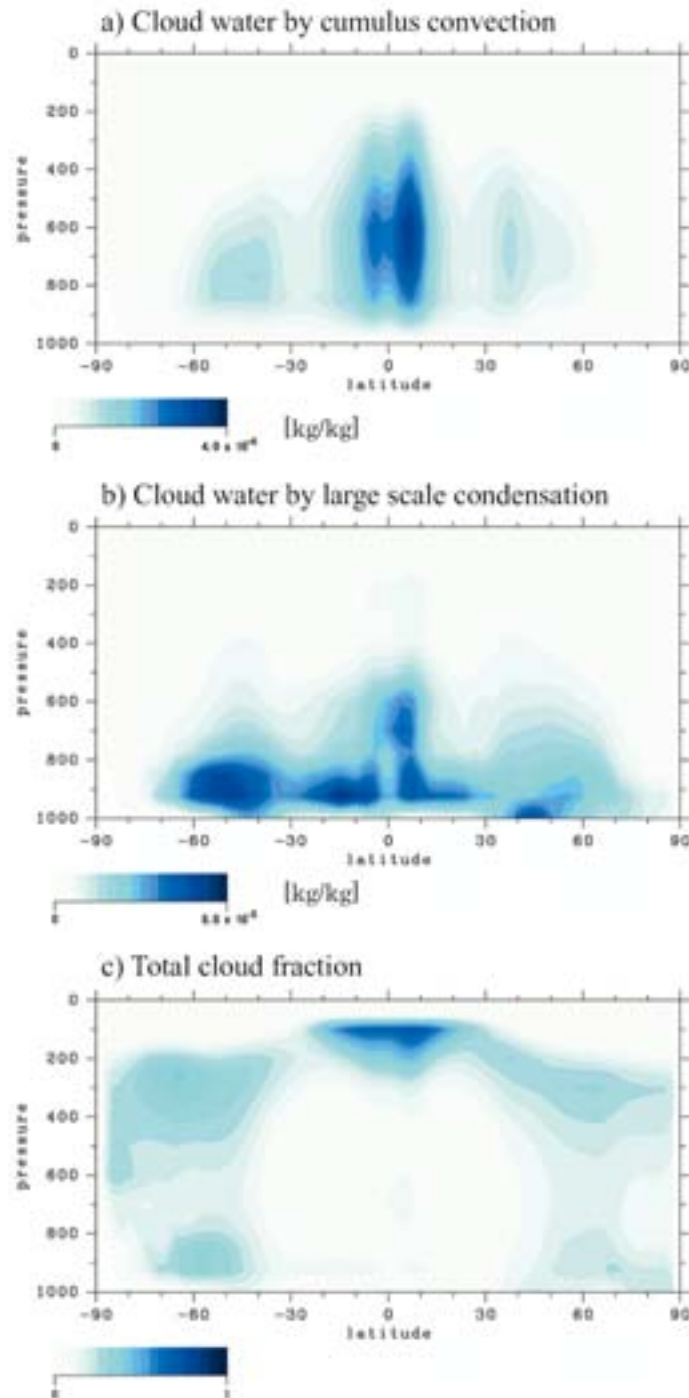


**Fig. 3.8:** Zonal mean of the model simulation for a) cloud water formed by cumulus convection, b) cloud water formed by large scale condensation (LSC), and c) total cloud fraction.

### 3.3 Variability of the Climate System

Features of the variability in the atmosphere-ocean climate system are briefly investigated in the present section. Here, the simulated features of El Niño/Southern Oscillation (ENSO), which has one of the largest variabilities in the real climate system, are presented and

compared with observation. Fig. 3.9 shows SST anomalies over the NINO3 region ( $5^{\circ}\text{N}$ - $5^{\circ}\text{S}$ ,  $150^{\circ}\text{W}$ - $90^{\circ}\text{W}$ , namely the NINO3 index) of the model simulation and observation. For the model result, 20 years of data were arbitrarily chosen from the integration after the simulated climate states had reached equilibrium. For the observation, data from the year 1980 to 2000 were chosen. Overall, the model has a feature similar to the NINO3 index: an oscillation with a period of about a few years. However, the simulated amplitude of the oscillation is smaller than the observation.

Fig. 3.9 also shows the longitudinal profile of SST anomalies for the simulation and observation. As in the case of the amplitude, the longitudinal region of oscillation is different from the observation: The simulated region with oscillation is much wider in longitude, and extends further westward compared to the observation. These features could be related to biases in the circulation and/or temperature in the ocean. This discrepancy in ENSO features between model simulations and observation has been reported among other state-of-the-art climate models (e.g., AchutaRao and Sperber 2006). In addition, the range of the simulated ENSO amplitude spans an order of magnitude among them (e.g., Santer *et al.*, 2005). Therefore, it is of considerable importance to improve the model's ability to simulate ENSO features in the real world in future work.

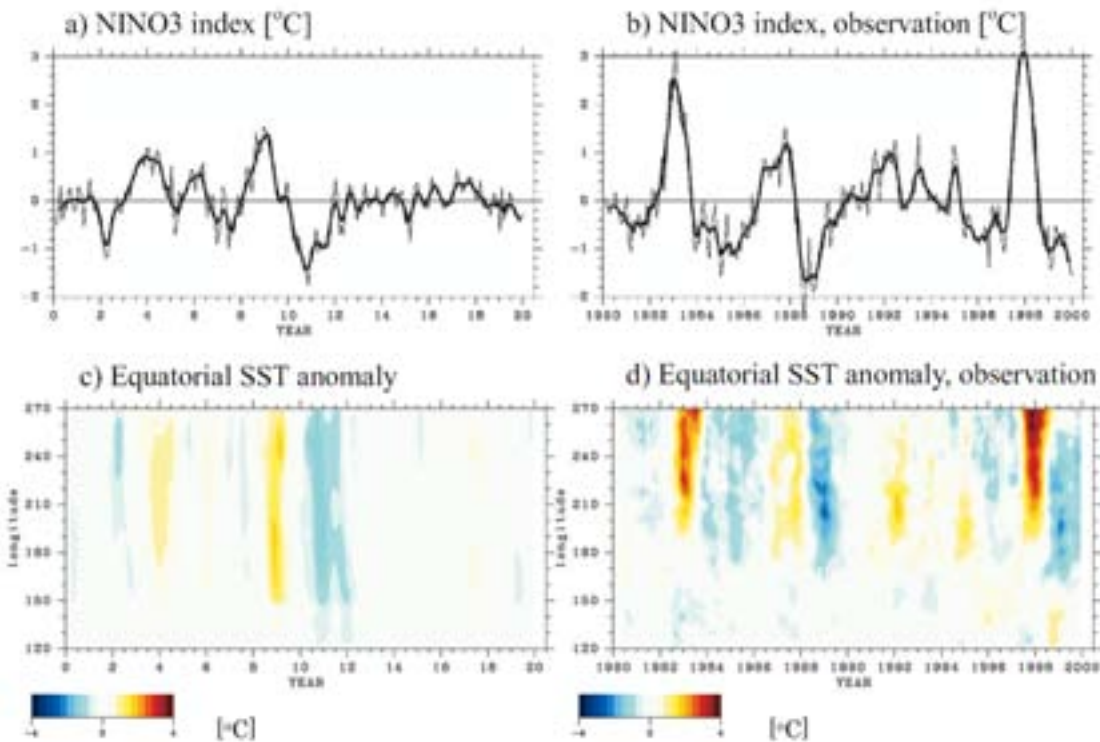


**Fig. 3.9:** El Niño/Southern Oscillation index from 20 years of data from the model simulation (left column) and observation from the year 1991 to 2000 (right column). a-b) NINO3 index and c-d) Equatorial (from  $4^{\circ}\text{S}$  to  $4^{\circ}\text{N}$ ) SST anomaly at longitudes from  $120^{\circ}$  to  $270^{\circ}$ . Anomalies are calculated by taking the 20-year monthly averaged data as a baseline.

## References

- AchutaRao, K., Sperber, K.R. (2006) ENSO simulation in coupled ocean-atmosphere models: are the current models better? *Climate Dynamics*, 27, 1-15.
- Barkstrom, B.R., Harrison, E.F., G. Smith, R. Green, J. Kibler, R. Cess, and the ERBE Science Team (1989) Earth Radiation Budget Experiment (ERBE) Archival and April 1985 Results. *Bulletin of American Meteorological Society*, Vol. 70, No. 10, 1254-1262.
- Delworth, T.L., Rosati, A., Stouffer, R.J., Dixon, K.W., Dunne, J., Findell, K., Ginoux, P., Gnanadesikan, A., Gordon, C.T., Griffies, S.M., et al. (2006) GFDL's CM2 Global Coupled Climate Models. Part I: Formulation and simulation characteristics. *Journal of Climate*, 19(5), 643-674.
- Gnanadesikan, A., Dixon, K.W., Griffies, S.M., Delworth, T.L., Harrison, M.J., Held, I.M., Hurlin, W.J., Pacanowski, R.C., Rosati, A., Samuels, B.L., et al. (2006) GFDL's CM2 Global Coupled Climate Models. Part II: The baseline ocean simulation. *Journal of Climate*, 19(5), 675-697.
- Johns, T.C., Durman, C.F., Banks, H.T., Roberts, M.J., McLaren, A.J., Ridley, J.K., Senior, C.A., Williams, K.D., Jones, A., Rickard, G.J., et al. (2006) The New Hadley Centre Climate Model (HadGEM1): Evaluation of Coupled Simulations. *Journal of Climate*, 19, 1327-1353.
- Oka, A., Hasumi, H., Okada, N., Sakamoto, T., Suzuki, T. (2006) Deep convection seesaw controlled by freshwater transport through the Denmark Strait. *Ocean Modelling*, 15, 157-176.
- Rayner, N.A., Parker, D.E., Horton, E.B., Folland, C.K., Alexander, L.V., Rowell, D.P., Kent, E.C., Kaplan, A. (2003) Global analyses of sea surface temperature, sea ice, and night marine air temperature since the late nineteenth century. *J. Geophys. Res.*, 108, doi:10.1029/2002JD002670.
- Santer, B.D., Wigley, T.M.L., Mears, C., Wentz, F.J., Klein, S.A., Seidel, D.J., Taylor, K.E., Thorne, P.W., Wehner, M.F., Gleckler, P.J., et al. (2005) Amplification of surface temperature trends and variability in the tropical atmosphere. *Science*, 309, 1551-1556.
- Tsushima, Y., Emori, S., Ogura, T., Kimoto, M., Webb, M.J., Williams, K.D., Ringer, M.A., Soden, B.J., Li B., Andronova, N. (2006) Importance of the mixed-phase cloud distribution in the control climate for assessing the response of clouds to carbon dioxide increase: a multi-model study. *Climate Dynamics*, 27, 113-126.
- Uppala, S.M., Kållberg, P.W., Simmons, A.J., Andrae, U., da Costa Bechtold, V., Fiorino, M., Gibson, J.K., Haseler, J., Hernandez, A., Kelly, G.A., et al. (2005) The ERA-40 re-analysis. *Quart. J. R. Meteorol. Soc.*, 131, 2961-3012.
- Vellinga, M., Wu, P. (2004) Low-latitude freshwater influence on centennial variability of the Atlantic Thermohaline Circulation. *J. Climate*, 17, 4498-4511.
- Vincent, D.G. (1994) The south Pacific convergence zone (SPCZ): A Review. *Monthly Weather Review*, 122, 1949-1970.
- Xie, P., Arkin, P.A. (1997) Global precipitation: A 17-year monthly analysis based on gauge observations, satellite estimates and numerical model outputs. *Bull. Amer. Meteor. Soc.*, 78, 2359-2558.
- Yokohata, T., Emori, S., Nozawa, T., Tsushima, Y., Ogura, T., Kimoto, M. (2005a) Climate response to volcanic forcing: Validation of climate sensitivity of a coupled atmosphere-ocean general circulation model. *Geophys. Res. Lett.*, 32, L21710, doi:10.1029/2005GL023542.
- Yokohata, T., Emori, S., Nozawa, T., Ogura, T., Tsushima, Y., Kimoto, M. (2005b) A simple scheme for climate feedback analysis. *Geophys. Res. Lett.*, 32, L19703, doi:10.1029/2005GL023673.
- Yokohata, T., Emori, S., Nozawa, T., Ogura, T., Okada, N., Suzuki, T., Tsushima, Y., Kawamiya, M., Abe-Ouchi, A., Hasumi, H., Sumi, A., Kimoto, M. (2007) Different transient climate responses of two versions of an atmosphere-ocean coupled general circulation model., *Geophys. Res. Lett.*, 34, L02707, doi:10.1029/2006GL027966.
- Yukimoto S., Noda, A., Kitoh, A., Hosaka, M., Yoshimura, H., Uchiyama, T., Shibata, K., Arakawa, O., Kusunoki, S. (2006) Present-day climate and climate sensitivity in the Meteorological Research Institute Coupled GCM Version 2.3 (MRI-CGCM2.3). *J. Meteor. Soc. Japan*, 84, 333-363.
- Zhang, C. (2001) Double ITCZs. *J. Geophys. Res.*, 106, 11785-11792.



## Chapter 4: Transient Climate Responses to Increasing CO<sub>2</sub>

In the present chapter, the characteristics of the transient climate response to increasing atmospheric CO<sub>2</sub> concentration (1%/year compounded) are described. As the atmospheric CO<sub>2</sub> concentration increases, the tropospheric atmospheric temperature increases owing to the enhanced greenhouse effect of CO<sub>2</sub>. This atmospheric warming changes the states of factors in the climate system, such as water vapor, clouds, and surface snow and ice, then the climate feedback processes change the rate of the atmospheric warming (Hartmann, 1994). In the following, we first present an overview of the time evolution of the climate system. Next, we describe the mean climate states in global warming by using the simulated results at the time of doubled atmospheric CO<sub>2</sub>. Finally, the strength of the climate feedback processes is analyzed by using a simple scheme we developed (Yokohata *et al.*, 2005).

### 4.1 Time Evolution of the Climate System

Fig. 4.1a shows the time series of the globally averaged atmospheric temperature anomalies in the 1% per year CO<sub>2</sub> increase experiment (1%CO<sub>2</sub>). The increase in the globally averaged surface air temperature (SAT) is about 1.9 K at the time of doubling CO<sub>2</sub> concentration (70 years) and about 4.9 K at the time of quadrupling (140 years). This increase in SAT is about the average among the state-of-the-art climate models that contributed to the Intergovernmental Panel on Climate Change 4th Assessment Report (IPCC AR4) (Yokohata *et al.*, 2007, Winton, 2006).

The vertical distribution of the globally averaged atmospheric temperature is shown in Fig. 4.1b. Maximum warming can be seen at an altitude of about 300 hPa, which is in the upper troposphere. Very strong warming at this altitude occurs possibly because of “lapse rate feedback”: Since the atmospheric vertical temperature profile is close to the moist adiabatic lapse rate (MALR, e.g., Stone, 1979) and the MALR decreases when the temperature increases (e.g., Hartmann, 1994) the lapse rate decreases from global warming. This change in the lapse rate causes an amplification of the warming in the upper troposphere (Santer *et al.*, 2005). On the other hand, atmospheric cooling can be seen above an altitude of 100 hPa (Fig. 4.1b). This is because the stratospheric cooling is enhanced by the increase in CO<sub>2</sub> concentration.

Fig. 4.2 shows the time evolution of the ocean temperature. The surface layer warms more effectively than deeper layers. Especially at depth less than 100 m, about the depth of the ocean thermocline, the temperature increasing rate is very large. The ocean water above this depth is warmed very effectively because of strong mixing. Because of this effective surface ocean warming, the vertical temperature gradient increases with time. This enhanced ocean stratification should also work as positive feedback which enhances the increase in SAT (e.g., Russell *et al.*, 2006).

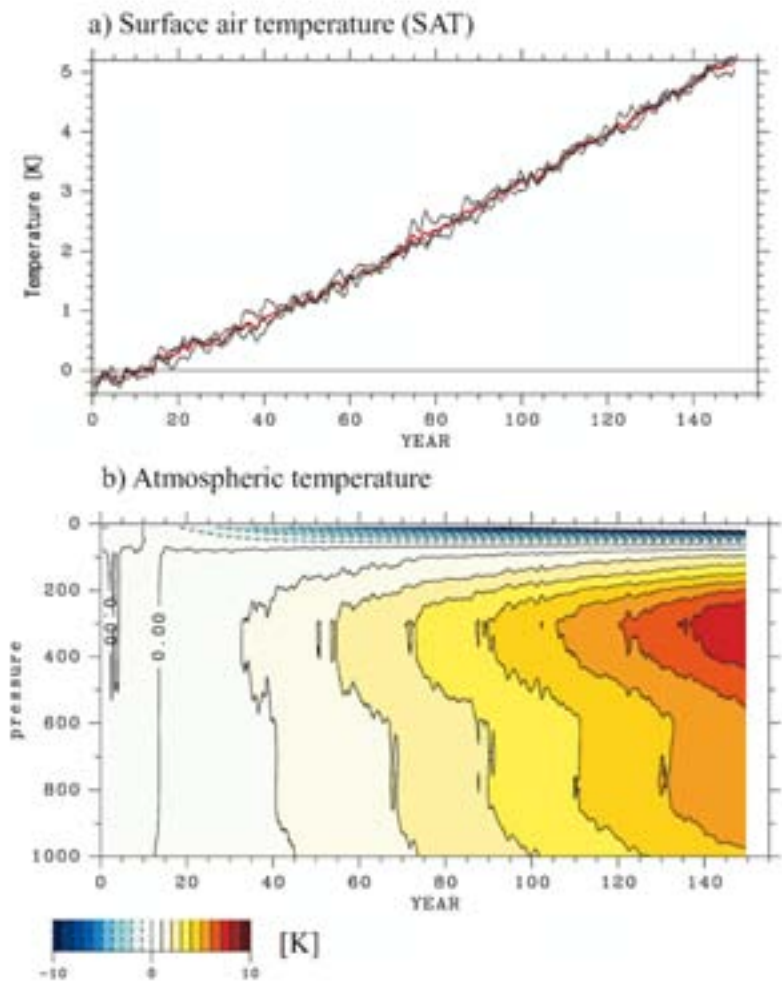


**Fig. 4.1: Time series of globally averaged atmospheric temperature anomalies in the 1%/year CO<sub>2</sub> increase experiment (1%CO<sub>2</sub>).** Anomalous time series of a) surface air temperature (SAT) and b) vertical distribution. Anomalies are calculated by taking the average of the first 20 years as a baseline.

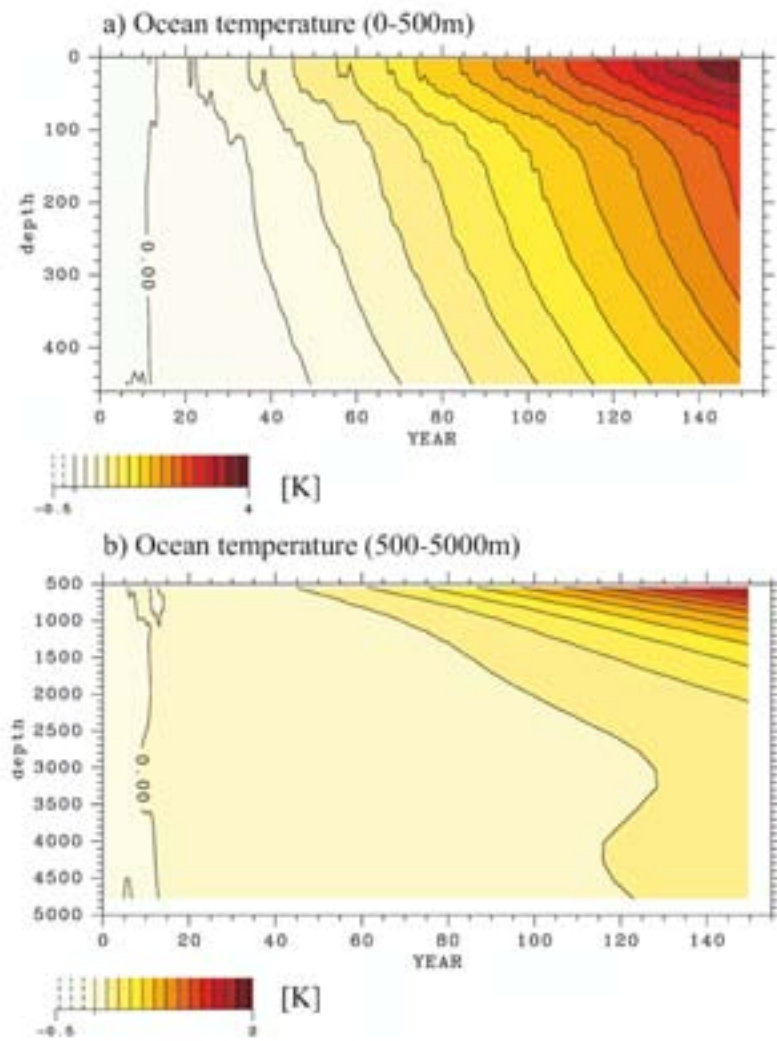


**Fig. 4.2:** Time series of the globally averaged ocean temperature anomaly in 1%CO<sub>2</sub> for depths a) from the surface to 500 m and b) below 500 m. Anomaly calculation is the same as for Fig. 4.1.



## 4.2 Mean Climate States in Global Warming

Here we describe the simulated mean climate states in 1%CO<sub>2</sub>. Fig. 4.3 shows the SAT anomalies at the time of CO<sub>2</sub> doubling by taking the average of the first 20 years as a baseline. The anomaly of annually averaged SAT is shown in Fig. 4.3a. The increase in the temperature is large in the high northern latitudes, especially around the Arctic Ocean. The maximum SAT increase corresponds to areas of sea-ice reduction (a global map of ice-albedo feedback is shown in Fig. 4.9c) and, in general, larger SAT increases can be seen over land than over ocean.

The annual averages of daily maximum SAT (SAT max) and daily minimum SAT (SAT min) are shown in Figs. 4.3b and 4.3c, respectively. Generally, the geographical patterns of SAT max and SAT min are similar to that of SAT, but the increase in SAT max is especially large over continental areas such as the Amazon, southern Africa, and western Australia. Although the difference between SAT max and SAT min (diurnal temperature range, DTR) is generally negative over almost the entire world (the DTR decreases with global warming), it is positive over the above continental areas.

Fig. 4.4 shows the anomalies of sea surface temperature (SST) and precipitation. The global map of SST anomaly in 1%CO<sub>2</sub> (Fig. 4.4a) is slightly different from that of the SAT anomaly (Fig. 4.3a). The former is more inhomogeneous compared to the latter because it is directly affected by the anomaly in the ocean current. For example, the SST anomaly is large in the northern Pacific and northern Atlantic where anomalies of ocean current and convection are large (e.g., Sakamoto *et al.*, 2005) whereas the SAT anomaly is not so large in these areas.

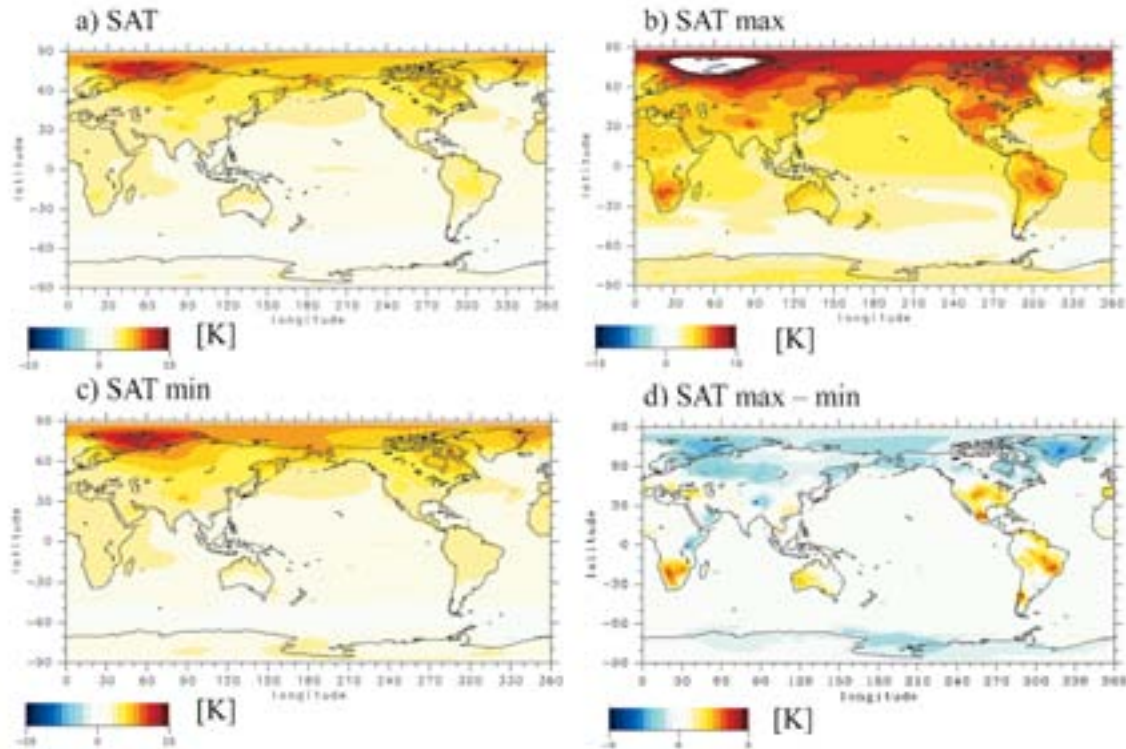


**Fig. 4.3:** Global maps of the anomalies from the annual averages of a) SAT, b) diurnal maximum of SAT, c) diurnal minimum of SAT, and d) the difference between b) and c), namely the diurnal temperature range. Note that the color range of each figure is different. Anomalies are calculated by using the 20-year average around the time of doubling of the atmospheric CO<sub>2</sub> concentration (the integration year from 60 to 80) taking the first 20-year average as a baseline.

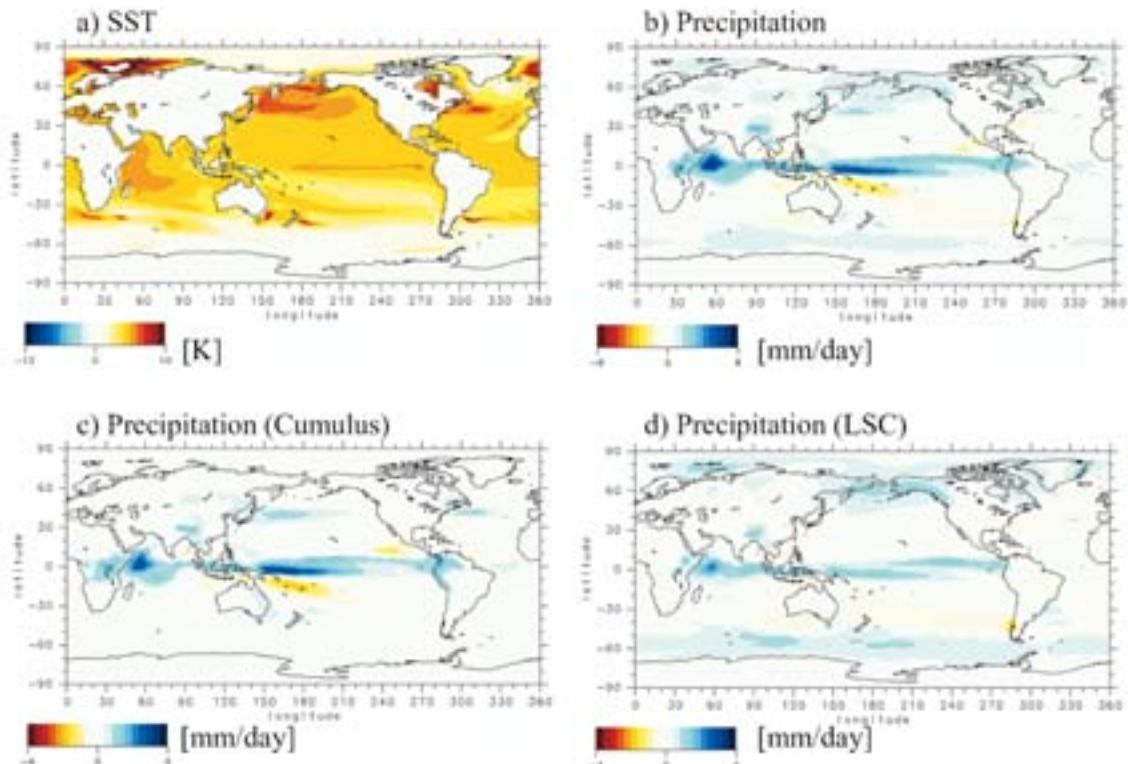


Fig. 4.4: Same as Fig. 4.3 but for a) sea surface temperature (SST), b) precipitation, c) precipitation by cumulus convection, and d) precipitation by large scale condensation (LSC).

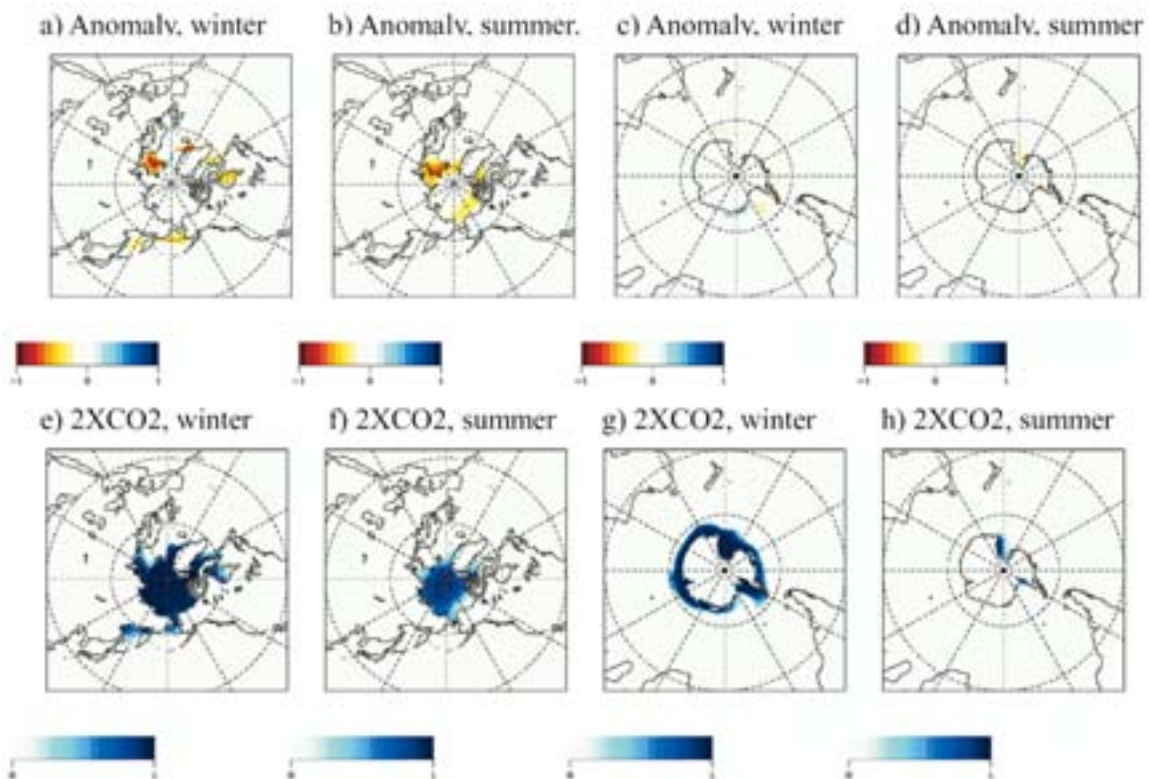


Fig. 4.5: Anomalies in sea-ice concentration (upper column) and sea-ice concentration at the time of doubled CO<sub>2</sub> (2XCO<sub>2</sub>, lower column). Data from December to February are used for the northern winter and southern summer, and from June to August for the northern summer and southern winter.

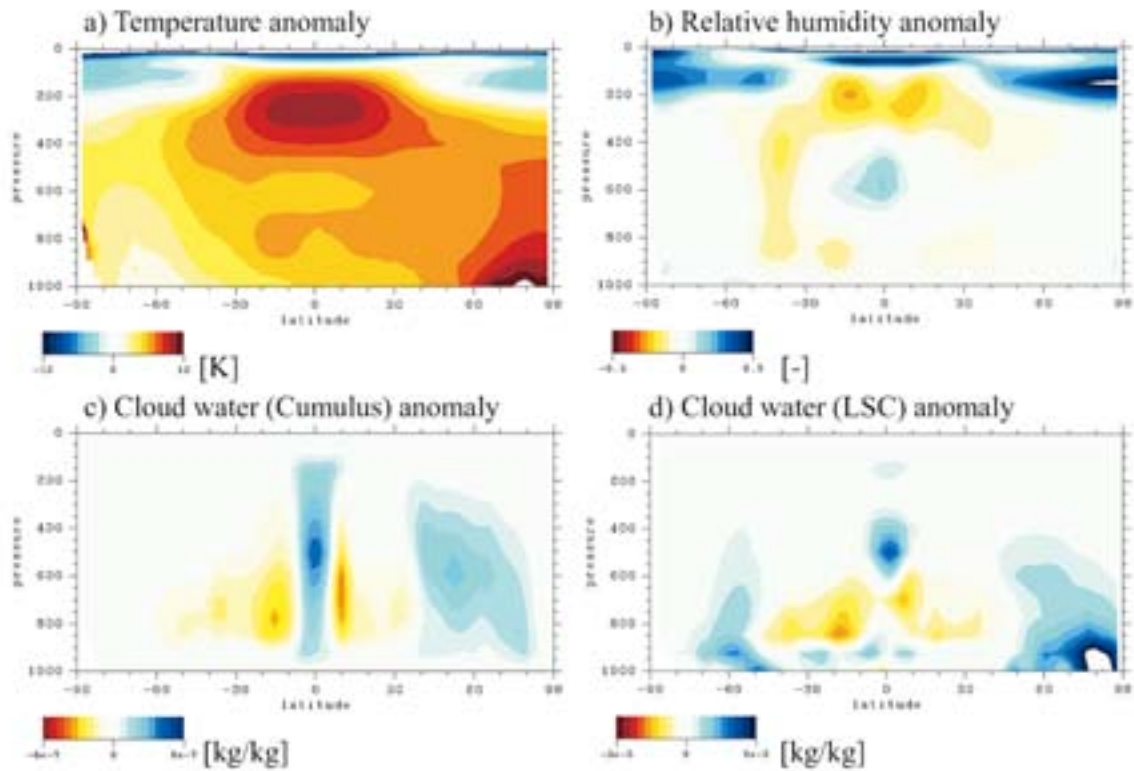
It is interesting to compare the anomaly of SST with that of precipitation. In equatorial regions such as the Indian Ocean (west of Africa around the equator) and the Pacific Ocean (around Indonesia), the precipitation anomaly shows strong maxima. In these areas, the SST anomaly also has large values compared to other regions around the equator. It seems that the large SST anomalies caused the large precipitation anomalies. In high-latitude regions such as the northern Pacific, Barents Sea, and Hudson Bay, very large SST anomalies can be seen. Around these areas, the precipitation anomaly is also large. Precipitation anomalies by cumulus convection and by large scale condensation (LSC) are shown in Figs. 4.4c and 4.4d, respectively. Anomalies of both cumulus and LSC precipitation are large around the equatorial region mentioned above, whereas only that of LSC is dominant at high latitudes in the northern and southern hemispheres.

Fig. 4.5 shows the sea-ice concentration anomaly and the sea-ice concentration at the time of doubled atmospheric CO<sub>2</sub>. The sea-ice concentration anomaly is important for TCR because it determines the strength of the ice-albedo feedback. In the northern hemisphere, the sea-ice concentration decreases much more than in the southern hemisphere. The decrease of sea-ice area in summer is much greater and occurs at higher latitudes compared to that in winter. At the time of doubled atmospheric CO<sub>2</sub>, the sea-ice area in the summer season is about half of that in the winter season in the northern hemisphere. On the other hand, the decrease in sea-ice concentration in the southern hemisphere is much smaller compared to that in the northern hemisphere. Since the sea-ice concentration in the initial state (namely, the mean state of the control experiment) is underestimated compared to the observation (Fig. 4.4 in the description of control experiment), the response of sea ice would be underestimated in the southern hemisphere (see Yokohata *et al.*, 2007 for further discussion).

Fig. 4.6 shows vertical sections of the zonal means of temperature, humidity, and cloud water anomalies. As discussed in the explanation of Fig. 4.1b, the temperature increase is relatively large in the upper troposphere. In particular, in the equatorial region where the latitude is less than 30°, the temperature anomaly is very large. This is likely because at low latitudes, the temperature lapse rate is very close to moist adiabatic (Stone and Carlson, 1979) and thus the lapse rate feedback is more effective in these regions (Soden and Held, 2006). In addition, the temperature anomaly is very large at higher latitudes, especially at greater than 60° in the northern hemisphere. This is because strong ice-albedo feedback occurs around these areas. It is interesting to note that this warmth decreases with altitude. In the southern hemisphere, the surface temperature increase is not so large compared to that in the northern hemisphere. At altitudes higher than the tropopause, the temperature decreases with the atmospheric CO<sub>2</sub> increase as discussed in the explanation of Fig. 4.1b. Cooling is stronger at higher altitudes in the stratosphere.

The relative humidity anomaly is shown in Fig. 4.6b. Large decreases of relative humidity can be seen in the upper troposphere. It is interesting to note that there are two local maxima of relative humidity decrease between the equatorial region with latitudes below 30° at the altitude with the largest temperature increase (Figs. 4.6a and 4.6b). A decrease in relative humidity is also seen throughout almost all the altitude of the troposphere from 30° to 50° in the southern hemisphere. On the other hand, an increase in the relative humidity is seen at altitudes around 500 hPa in the equatorial region (latitudes less than 10°). Since the cumulus cloud water also increases in this region, it is conceivable that cumulus convection is enhanced in the equatorial region (e.g., Bony *et al.*, 2004). In the region next to the equatorial region, namely the subtropical region, cumulus cloud water decreases. This is possibly because the large-scale sinking is enhanced owing to the increase in the cumulus convection at the equatorial region (e.g., Bony *et al.*, 2004).

Cloud water by LSC increases at high latitudes with low altitude and at low latitudes with high altitude. These correspond to the temperature regions where a mixed-phase cloud (a mixture of solid and liquid cloud particles) exists in the model (K-1 model developers, 2004, Ogura *et al.*, 2007). In this mixed-phase region, solid cloud particles are converted to liquid cloud particles under global warming, and thus liquid cloud water increases in these regions. Since the sedimentation velocity of liquid cloud particles is smaller than that of solid cloud particles, the total cloud water (the sum of the solid and liquid cloud particle masses) increases in the mixed-phased region under global warming. In addition, since the reflectivity of liquid cloud particles is larger than that of ice cloud particles in the model (Ogura *et al.*, 2007), this increase in ice cloud particles causes an increase in cloud reflection under global warming (i.e., it causes a negative feedback). This is also shown in Fig. 4.9d, which illustrates the cloud-albedo feedback.



**Fig. 4.6: Zonal averages of anomalies in a) temperature, b) relative humidity, c) cloud water formed by cumulus convection, and d) cloud water by LSC. Anomalies are calculated in the same way as Fig. 4.4.**

Fig. 4.7 shows the zonal mean of zonal wind ( $u$ ). The zonal mean  $u$  anomaly is shown by comparing its mean state and bias to the control experiment. In the upper troposphere and stratosphere, the zonal mean  $u$  is enhanced at latitudes around  $30^\circ$  to  $40^\circ$  in both hemispheres under global warming (Fig. 4.7a). This intensification could be related to the shift of the westerly winds in the control experiment (Fig. 4.7b). In the southern hemisphere, the region of intensified anomaly in the zonal mean wind extends to the lower troposphere in the latitudinal regions from  $40^\circ\text{S}$  to  $60^\circ\text{S}$  (Fig. 4.7a). This intensification of the lower-tropospheric westerly winds corresponds to a poleward intensification of westerly winds, which possibly causes an increase in ocean heat uptake (Stouffer *et al.*, 2006, Russell *et al.*, 2006). The ocean heat uptake increases in these latitudinal areas (Fig. 4.9f), namely in



the Southern Ocean (details are discussed later). According to Russell *et al.*, (2006), the strength of the ocean heat uptake around these areas would depend on the initial position and strength of the westerly winds over the Southern Ocean. If the initial position of the westerly wind were shifted equatorward, the changes in ocean heat uptake would tend to be smaller. In our model, the westerly wind is shifted equatorward compared to observation (Fig. 4.7c). It is interesting to compare the ocean heat uptake in our model (Fig. 4.9f) with other climate models by paying attention to the initial position of the westerly winds in the control experiments (Figs. 4.7b and 4.7c).

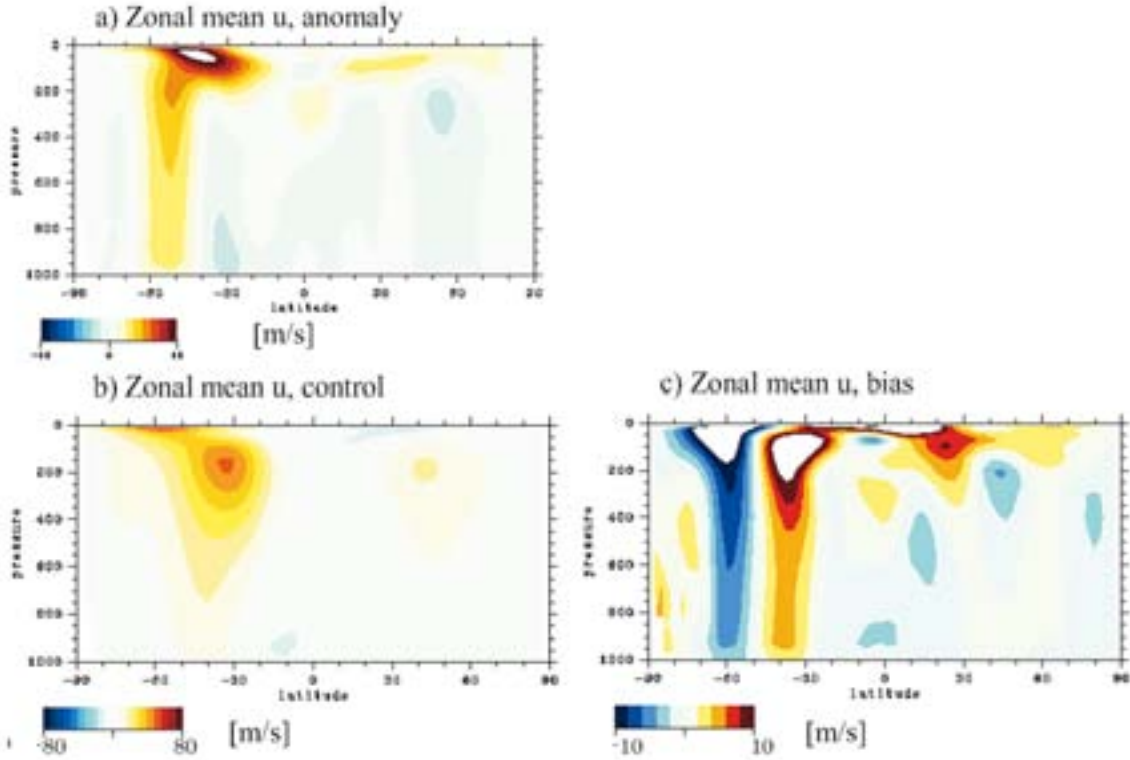


**Fig. 4.7: Zonal mean of zonal wind (u), a) anomaly calculated in the same way as Fig. 4.5, b) in the control experiment, and c) bias in the control experiment.**

### 4.3 Climate Feedback Processes in Global Warming

Finally, we present a climate feedback analysis of 1%CO<sub>2</sub> performed using a scheme we developed (Yokohata *et al.*, 2005, hereinafter called Y05). In our Y05 scheme, the response parameters ( $\gamma$ ) are calculated from anomalies in the shortwave (SW) and longwave (LW) fluxes at the top of the atmosphere (TOA) caused by changes in the surface (SFC), clear-sky atmosphere (CLR), and clouds (CLD), divided by the globally averaged anomaly of SAT ( $\Delta T$ ). When calculating  $\gamma$ , the radiative forcing components are removed. We can evaluate the major radiative feedbacks caused by changes in the surface snow/ice albedo (SFC-SW), water vapor and lapse rate (CLR-LW), and clouds (CLD-SW and CLD-LW). Stefan-Boltzmann damping is evaluated as SFC-LW. We can also calculate the change in the heat content of the climate system from the net downward radiative flux at the TOA,  $\Delta F_{\text{TOA}}$ . Since the heat content of the atmosphere and land surface is small compared to that of the ocean (confirmed by our model results), we can determine the ocean heat uptake (OHU) anomaly by  $\Delta F_{\text{TOA}} / \Delta T$ , which corresponds to the “ocean heat uptake efficiency” defined in Gregory and Mitchell

(1997). Here, positive ocean heat uptake indicates negative feedback because the large ocean heat uptake retards the SAT increase under global warming.

Fig. 4.8 shows the globally averaged response parameters and ocean heat uptake in 1%CO<sub>2</sub>. One of the strongest positive feedback parameters is water vapor and lapse rate feedback (CLR-LW). SW cloud feedback (CLD-SW) is the second strongest positive feedback, and LW cloud feedback (CLD-LW) has opposite sign. Ice-albedo feedback (SFC-SW) has positive feedback with an absolute value similar to LW cloud feedback. Stefan-Boltzmann damping (SFC-LW) is large enough to compensate the other SW and LW feedbacks and OHU.

Fig. 4.9 shows global maps of the climate feedback processes described above. It is interesting to interpret these maps by comparison to the global map of the SAT anomaly (Fig. 4.3). Water vapor and lapse rate feedback shows a response similar to the SAT anomaly (Fig. 4.9a). This is because the regions where the SAT increase is large have large increases in water vapor and thus have strong positive water vapor feedback. Since the global map shown in Fig. 4.9 is calculated by the anomaly of radiative fluxes over the globally averaged SAT, a strong signal in the response parameters can be seen where the SAT increase is large. This is the case for the global map of Stefan-Boltzmann damping (Fig. 4.9e). Also, as discussed in the explanation of the SAT anomaly (Fig. 4.3a), ice-albedo feedback works effectively in the Arctic Ocean, especially around the area of the Barents Sea. Note that ice-albedo feedback in the Southern Ocean also plays an important role in determining the climate response under global warming (Yokohata *et al.*, 2007). Ocean heat uptake also plays an important role in determining the climate response: In our model, ocean heat uptake becomes large in regions of large ocean mixing (Yokohata *et al.*, 2007).

It is interesting to compare global maps of LW and SW cloud feedback. In general, their globally averaged values have opposite signs (e.g., Colman, 2003, Soden and Held, 2006). However, their geological distributions are not so straightforward: In LW cloud feedback, negative values can be seen forming two inhomogeneous band structures (Fig. 4.9b). On the other hand, SW cloud feedback has a relatively homogeneous positive value over the Pacific and Atlantic Oceans, which could be caused by the decrease in low altitude clouds (Fig. 4.6d) (Webb *et al.*, 2006).

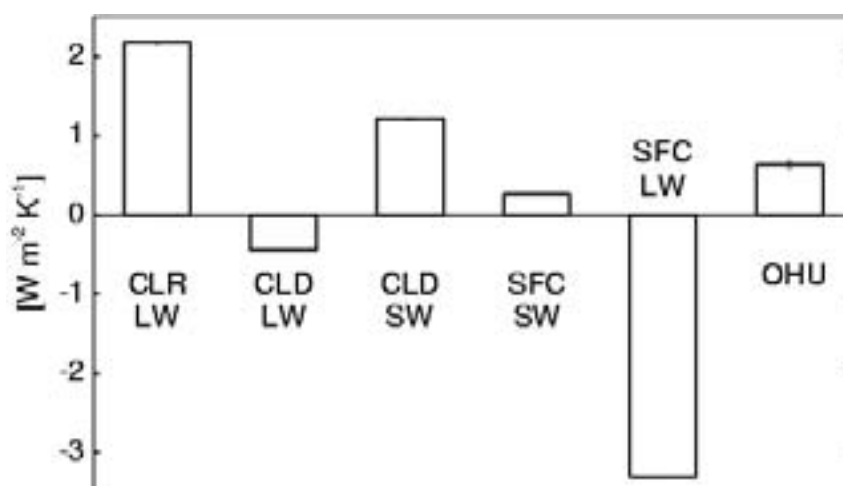


**Fig. 4.8: Climate feedback analysis based on the scheme by Yokohata *et al.*, 2005.** The response parameters and ocean heat uptake are shown (details are given in the main text). The parameters are calculated by taking the anomaly of the 20-year averages (from the year 60 to 80) using the first 20-year average as a baseline.

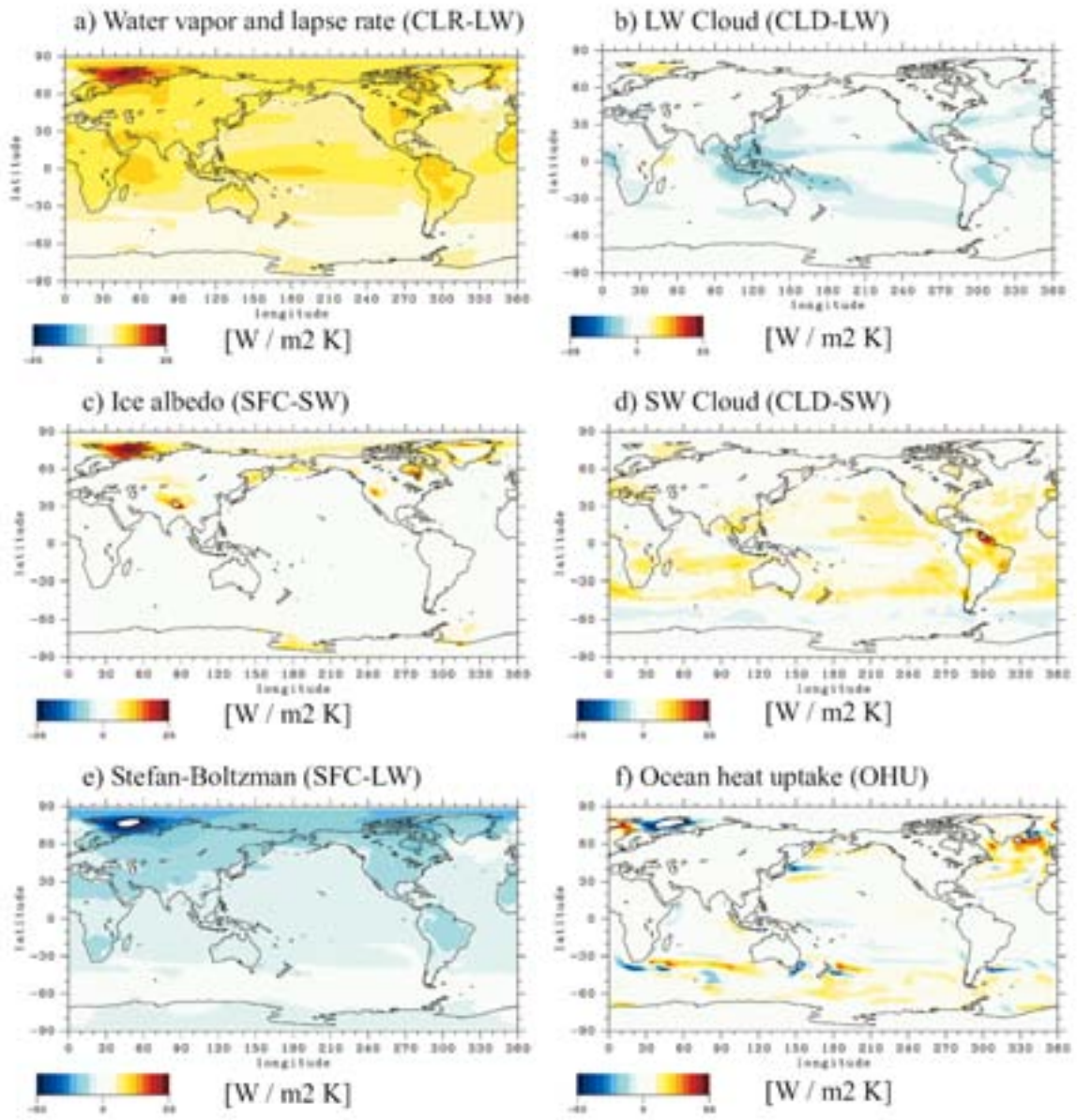


Fig. 4.9: Global maps of the parameters shown in Fig. 4.8. Details are explained in the main text.

## References

- Bony, S., Dufresne, J.L., Le Treut, H., Morcrette, J.J., Senior, C. (2004) On dynamic and thermodynamic components of cloud changes. *Clim. Dyn.*, 22, 71-86, DOI 10.1007/s00382-003-0369-6.
- Colman, R.A. (2003) A comparison of climate feedbacks in general circulation models. *Clim. Dyn.*, 20, 865-873.
- Gregory, J.M., Mitchell, J.F.B. (1997) The climate response to CO<sub>2</sub> of the Hadley Centre coupled AOGCM with and without flux adjustment. *Geophys. Res. Lett.*, 24, 1943-1946.
- Hartmann, D.L. (1994) *Global physical climatology*. Academic Press, New York, 411pp.
- K-1 model developers (2004) K-1 coupled GCM (MIROC) description, K-1 technical report. 1, Hasumi, H., Emori, S. (eds.), Center for Climate System Research, University of Tokyo, Tokyo, 34pp.
- Ogura, T., Emori, S., Tsushima, Y., Yokohata, T., Abe-Ouchi, A., Kimoto, M. (2007) Climate sensitivity of a general circulation model with different cloud modelling assumptions. *Climate sensitivity of a general circulation model with different cloud modelling assumptions*, submitted to *J. Meteor. Soc. Japan*.
- Russell, J.L., Dixon, K.W., Gnanadesikan, A., Stouffer, R.J., Toggweiler, J.R. (2006) The southern hemisphere westerlies in a warming world: Propping open the door to the deep ocean. *J. Climate* 19, 6382-6390.
- Sakamoto, T.T., Hasumi, H., Ishii, M., Emori, S., Suzuki, T., Nishimura, T., Sumi, A. (2005) Responses of the Kuroshio and the Kuroshio Extension to global warming in a high-resolution climate model. *Geophys. Res. Lett.*, 32, L14617, doi:10.1029/2005GL023384.
- Santer, B.D., Wigley, T.M.L., Mears, C., Wentz, F.J., Klein, S.A., Seidel, D.J., Taylor, K.E., Thorne, P.W., Wehner, M.F., Gleckler, P.J., et al. (2005) Amplification of surface temperature trends and variability in the tropical atmosphere. *Science* 309, 1551-1556.
- Soden, B.J., Held, I.M. (2006) An assessment of climate feedbacks in coupled ocean-atmosphere models. *J. Climate*, 19(14), 3354-3360.
- Stone, P.H., Carlson, J.H. (1979) Atmospheric lapse rate regimes and their parameterization. *J. Atmos. Sci.*, 36, 415-423.
- Stouffer, R.J., Russell, J., Spelman, M.J. (2006) Importance of oceanic heat uptake in transient climate change. *Geophys. Res. Lett.*, 33, L17704, doi:10.1029/2006GL027242.
- Webb, M.J., Senior, C.A., Sexton, D.M.H., Ingram, W.J., Williams, K.D., Ringer, M.A., McAvaney, B.J., Colman, R., Soden, B.J., Gudgel, R., et al. (2006) On the contribution of local feedback mechanisms to the range of climate sensitivity in two GCM ensembles. *Climate Dynamics*, 27, 17-38.
- Winton, M. (2006) Surface albedo feedback estimates for the AR4 climate models. *J. Climate*, 19, 359-365.
- Yokohata, T., Emori, S., Nozawa, T., Ogura, T., Tsushima, Y., Kimoto, M. (2005) A simple scheme for climate feedback analysis. *Geophys. Res. Lett.*, 32, L19703, doi:10.1029/2005GL023673.
- Yokohata, T., Emori, S., Nozawa, T., Ogura, T., Okada, N., Suzuki, T., Tsushima, Y., Kawamiya, M., Abe-Ouchi, A., Hasumi, H., Sumi, A., Kimoto, M. (2007) Different transient climate responses of two versions of an atmosphere-ocean coupled general circulation model with similar climate responses. *Geophys. Res. Lett.*, in press, doi:10.1029/2006GL027966.





## Chapter 5: 20th Century Simulations

The 20th century simulations are described in this chapter. In particular, we compare mean and extremes of near surface air temperature (SAT) between observations and the model. Causes of climate change in the 20th century are estimated by applying a state-of-the-art statistical analysis technique.

### 5.1 Causes of Global Warming during the Latter Half of the 20th Century

#### 5.1.1 Goals of This Section

A number of detection/attribution studies that compare the historical monthly mean SAT record and 20th century climate simulations of coupled atmosphere-ocean general circulation models (CGCM) have provided evidence that rising concentrations of well-mixed GHGs are largely responsible for the observed SAT warming, at least over the past 3 to 5 decades, on global and regional spatial scales (see the reviews by the Intergovernmental Panel on Climate Change (IPCC), 2001, and the International ad hoc Detection and Attribution Group, 2005). It has also been demonstrated that cooling due to anthropogenic aerosol emissions has potentially contributed greatly to counteracting the warming due to well-mixed GHGs (e.g., Tett *et al.*, 2002, hereinafter referred to as T02). Knowledge about the causes of past climate change enables us to constrain the uncertainties of future climate projections made by CGCMs (Stott and Kettleborough, 2002; Hegerl *et al.*, 2006; Stott *et al.*, 2006).

In this section, we confirm that the global warming observed over the latter half of the 20th century is attributable to human influences, primarily by increasing the concentrations of well-mixed GHGs, by comparing simulated SATs to an observed SAT dataset (Jones and Moberg, 2003).

#### 5.1.2 Experiments

Four ensembles with different combinations of external forcing factors were carried out for the period from 1850 to 2000. The first one is FULL, where the simulations were forced with both natural and anthropogenic forcings: changes in solar irradiance (Lean *et al.*, 1995), stratospheric volcanic aerosols (Sato *et al.*, 1993), well-mixed GHGs (Johns *et al.*, 2003), tropospheric and stratospheric ozone (Sudo *et al.*, 2002; Randel and Wu, 1999), surface emissions of anthropogenic carbonaceous aerosols and precursors of sulfate aerosols (Nozawa and Kurokawa, 2007; Lefohn *et al.*, 1999), and land use (Hirabayashi *et al.*, 2005). In the second (NTRL) and third (ANTH), the simulations were forced with natural and anthropogenic forcings, respectively. The final ensemble is GHGS, where the simulations were forced with changes in well-mixed GHGs only. Each ensemble consists of 4 ensemble simulations starting from different initial conditions taken from a stable pre-industrial control run.

#### 5.1.3 Results

Fig. 5.1 shows the temporal variations of the global annual mean SAT for the FULL, NTRL, ANTH, and GHGS ensembles. The observed SAT is superimposed on each ensemble. The FULL ensemble captures well the observed multi-decadal variations throughout the 20th century. In all ensembles except NTRL, the simulated SAT shows a remarkable temperature increase after the 1970s in close agreement with observed temperatures, suggesting that the warming observed in the past 3 decades resulted primarily from an increase in concentration

of well-mixed GHGs. GHGS shows larger warming than the observations in the latter half of the 20th century. The SAT warming of ANTH is closer to the observations than that of GHGS. Therefore, together with GHGS forcing, anthropogenic aerosol forcing is essential to reproduce the observed changes in SAT during the latter half of the 20th century.

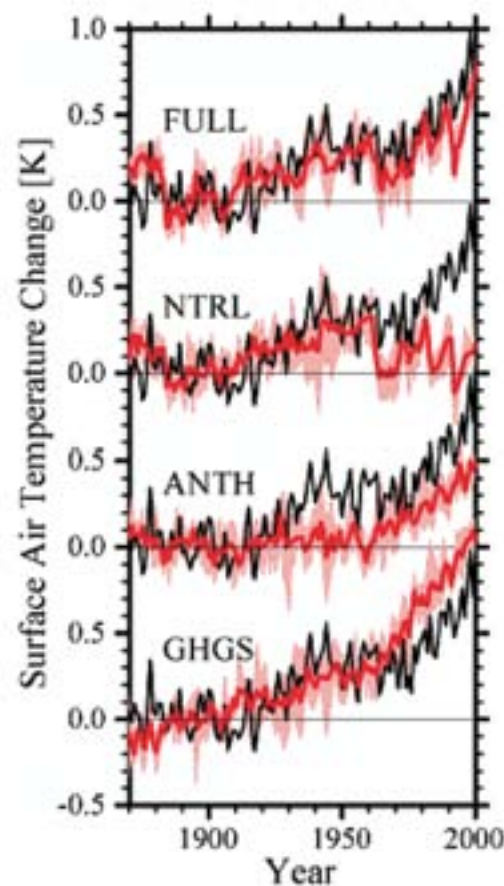


**Fig. 5.1: Temporal variations of global annual mean surface air temperature (SAT).** Anomalies from the 1881-1910 mean for the observations (Jones and Moberg, 2003) (solid thick line) and the ensemble mean of the FULL, NTRL, ANTH, and GHGS simulations (red thick lines). Maximum and minimum ranges from the individual simulations are shaded in pink. In calculating the global annual mean SAT, modeled data are projected onto the same resolution of the observations discarding simulated data at grid points where there were missing observational data. More than 10 months of data were required at each location to calculate the annual mean value.

## 5.2 Causes of Global Warming during the Early Half of the 20th Century: (1) Influences of Natural and Anthropogenic Forcings

### 5.2.1 Goals of This Section

As discussed in section 5.1, the global warming observed over the latter half of the 20th century is attributable to human influences. However, there is considerable uncertainty about the SAT responses in the early 20th century. Possible causes include greenhouse-gas induced warming (Tett *et al.*, 1999; Stott *et al.*, 2001; T02; Hegerl *et al.*, 2003), internal variability (Delworth and Knutson, 2000), and natural climate forcings (Broccoli *et al.*, 2003; Meehl *et al.*, 2004a). While Broccoli *et al.* (2003) also suggested that early century warming could arise from a combined effect of internal variability and natural forcings, T02 and Hegerl *et al.* (2003) mentioned that early warming could stem from a combined effect of well-mixed GHGs and natural contributions. Stott *et al.* (2003, hereinafter S03), based on simulations with HadCM3 (Gordon *et al.*, 2000), indicated that early warming is attributable to a combination of increased well-mixed GHGs and solar irradiance changes. Therefore, owing to this obvious lack of agreement, we feel further investigation is required to clarify which forcing factors contribute extensively to early 20th century warming. In this section, we estimate the natural and anthropogenic contributions to the observed temperature increase in the early 20th century. An optimal fingerprinting method (Hasselmann, 1997; Allen and Stott, 2003) is applied to detect natural and anthropogenic influences on the early SAT rises.

### 5.2.2 Experiments

We analyzed the FULL, NTRL, ANTH, and GHGS experiments. We also used a stable 1300-year pre-industrial control run. The simulated decadal variability of the control run is comparable to the decadal variability found in observations. For example, the standard deviation of the observed global decadal mean SAT, calculated from linearly detrended data for the 1900-1949 period, falls within the minimum and maximum range of the simulated standard deviations for 50-year segments of the control run. An *F*-test revealed that there is no significant disagreement between the observed and the modeled decadal variability.

### 5.2.3 Results

Fig. 5.1 shows that all ensembles except ANTH reproduce the early century warming. In the ANTH simulations, the warming due to well-mixed GHGs is offset by a cooling due to increases in anthropogenic aerosols, resulting in no significant warming until the 1950s (Nagashima *et al.*, 2006; section 5.4). The simulated temperature increase in NTRL in the first half of the 20th century is about 0.5 K/century, which is slightly less than that in the observations. This global annual mean SAT trend in NTRL is larger than those in Stott *et al.* (2000) and T02 (~0.3 K/century) for their simulations with natural forcings only, although we use natural forcing datasets identical to the ones they used. The trend of the global annual mean SAT in GHGS is nearly equal to that in NTRL; therefore, without further investigation, we cannot conclude which factors are the main contributors to the observed early warming.

Geographical distributions of linear SAT trends for the first half of the century are shown in Fig. 5.2 for the observations and the ensemble mean of each ensemble. The trend patterns in NTRL as well as in FULL (Figs. 5.2b and 5.2c) compare quite favorably with the trend pattern drawn from the observations (Fig. 5.2a). In the ANTH simulations, on the other hand, the indirect effect of anthropogenic aerosols introduces cooling trends in North America and the Northern Atlantic Ocean (Fig. 5.2d), where the observed warming was largest in this period (1900-1949) (Fig. 5.2a). The trend pattern in GHGS (Fig. 5.2e) looks less similar to the

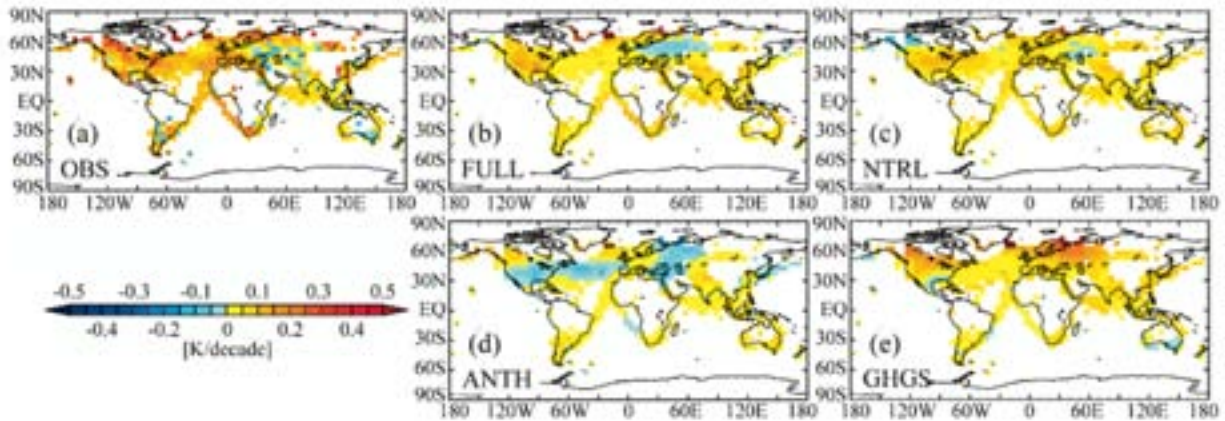
trends in the observations than do the trends in NTRL.

To clarify the relative importance of the effect of well-mixed GHGs and natural influences on warming in the early 20th century, an optimal detection method using total least squares regression (TLS) (Allen and Stott, 2003) was applied to the simulated and observed SATs. In contrast to ordinary least squares regression (OLS), as was used in many previous studies (e.g., T02), TLS takes into account sampling uncertainty in the model responses when estimating the signal amplitudes, and gives an unbiased regression coefficient. Similar to the analysis of T02, we regress the observed spatio-temporal variations onto the 3 model-derived response patterns from GHGS, ANTH, and NTRL to estimate the signal amplitudes for GHGS, ANTH-GHGS (i.e., the temperature response to all the anthropogenic influences except well-mixed GHGs), and NTRL effects. The signal amplitude for ANTH-GHGS is computed via a linear transformation from the GHGS and ANTH responses (see T02 for more details). Following the approach of Stott *et al.* (2001), the observed and simulated SATs in the early 20th century (1900-1949) were averaged decadal, expressed as anomalies with respect to the same period, and filtered by projecting onto T4 spherical harmonics. We calculate the signal amplitudes by estimating covariance matrices, for optimization, from the intra-ensemble spread of the ensembles using a truncation of 10 eigenvectors (EOFs). Applying the residual test of Allen and Tett (1999), we found that the residual in the regression was consistent with control variability. The uncertainty on the amplitudes was estimated from our 1300-year control simulation.

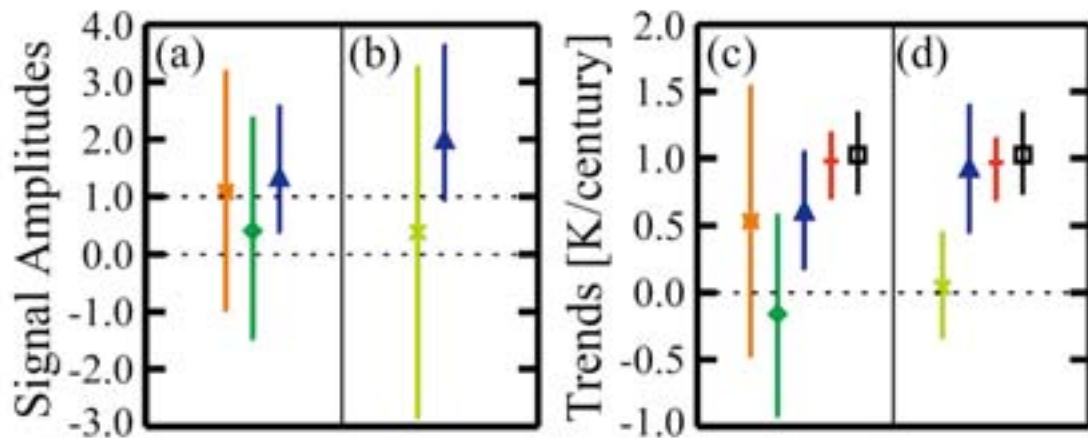
The estimated signal amplitudes and uncertainty ranges (Fig. 5.3a) indicate that, unlike with T02, only the natural contribution is detectable (i.e., only the uncertainty range for NTRL is entirely positive), and since the uncertainty range includes unity, the signal amplitude is consistent with the amplitude of the signal in observations. It should also be noted that the detection of the NTRL signal and its consistency with the observations is independent of the number of EOFs retained in the analysis (not shown). Therefore the detected natural contribution is robust. The 2 anthropogenic signals, on the other hand, have large uncertainty and are not detectable. Again this result is independent of the number of EOFs retained in the analysis (not shown). To make a direct comparison with the analysis of T02, we repeated our analysis using OLS. We found that the best-estimated signal amplitudes are not largely different from those shown in Fig. 5.3a (calculated with TLS). However, since OLS assumes no sampling uncertainty in the model responses, the estimated uncertainty limits are smaller with OLS than with TLS (not shown). It should be noted that, unlike with T02, the 2 anthropogenic signals have large uncertainty and are not detected even in our OLS analysis.

Fig. 5.3c shows the best-estimated linear trends for the early half of the century. The total trend shows much better agreement with the observations than in T02. Note that the best-estimated trends in Fig. 5.3c are also not largely different from those with OLS. The natural forcing causes a warming trend of  $\sim 0.6$  K/century, which is about one half of the observed trend. This is consistent with the global annual mean SAT anomalies simulated in NTRL (Fig. 5.1). The residual of the observed trend ( $\sim 0.4$  K/century) may be caused by the combined anthropogenic forcings, primarily by the well-mixed GHGs. However, the 2 anthropogenic signals are highly uncertain and are not detected. Therefore the cause of the residual trend is not obvious.

The robustness of the NTRL signal is tested by regressing the observations onto the 2 simulated responses from ANTH and NTRL (Figs. 5.3b and 5.3d). Again, only the natural contribution is detected while the net anthropogenic signal is highly uncertain and is not detected. This confirms the significance of the natural contributions to early 20th century warming.



**Fig. 5.2: Geographical distributions of linear SAT trends (K/decade) in the first half of the century for the (a) observations (Jones and Moberg, 2003) and the ensemble means of the (b) FULL, (c) NTRL, (d) ANTH, and (e) GHGS simulations.** Trends were calculated from annual mean values only for those grids where annual data were available in at least 2/3 of the 50 years and distributed in time without significant bias.



**Fig. 5.3: Best-estimated (a, b) signal amplitudes and (c, d) linear trends (K/century) with 5%-95% uncertainty ranges for the 50-year segment from 1900 to 1949 for the (a, c) GHGS, ANTH-GHGS (anthropogenic signal other than well-mixed GHGs), and the NTRL analyses and for the (b, d) ANTH and NTRL analyses.** The orange error bar with an asterisk, green error bar with a diamond, light green error bar with a cross, and blue error bar with a triangle indicate GHGS, ANTH-GHGS, ANTH, and NTRL, respectively. Also shown in (c, d) are the total reconstructed trend from the regression model (red error bar with a plus) and the observed (solid error bar with a square) trend. Error bars denote 5%-95% uncertainty ranges.

### 5.2.4 Discussion

Surface air temperature changes simulated by a global coupled climate model with different external forcings are investigated to detect the observed climate change signals in the early 20th century. Unlike with several previous studies, the natural contribution is robustly detected in the observed early century warming by investigating linear temperature trend patterns and by employing a regression-based optimal detection technique. Further investigation is needed to clarify the relative importance between a recovery from heavy volcanic eruptions and an increase in solar irradiance; the results of such a study are reported in section 5.3.

In our statistical analysis, we cannot detect any anthropogenic contribution to early 20th century warming. However, we do note that the uncertainty range of the greenhouse-gas contribution is consistent with the estimated range of observed warming; therefore we cannot rule out that anthropogenic factors, particularly GHGS, have influenced global temperatures over the early 20th century.

We should note that since the uncertainty limits obtained from the optimal fingerprinting analysis are estimated using the control variability, our results are dependent on whether the control run correctly simulates the observed multi-decadal internal climate variability. Our simple analysis shows that the multi-decadal control variability of MIROC3.2 is comparable to the estimated observed variability, suggesting that our results using the optimal detection methodology are robust.

In our simulations, all the known major external forcing factors are introduced to reduce the uncertainties that arise due to missing forcing agents, although we recognize there could be large uncertainties in the newly introduced forcing agents such as the historical emission of carbonaceous aerosols. Nevertheless, the FULL ensemble shows spatio-temporal variations quite similar to the observations, suggesting that the errors in the external forcings are not obviously apparent.

## 5.3 Causes of Global Warming during the Early Half of the 20th Century: (2) Influences of Volcanic Activity and Changes in Solar Irradiance

### 5.3.1 Goals of This Section

In this section, we enlarge the work of section 5.2 by performing additional simulations of MIROC3.2 to investigate the relative importance of solar and volcanic forcings on early century warming. We also discuss the reason why the anthropogenic contribution is not well constrained in our model. Furthermore, we explore why different CGCMs respond differently to solar and volcanic forcings, and why these different responses lead to different estimates of the relative contributions of different factors causing early century warming.

### 5.3.2 Experiments

We consider 4 ensembles of 20th century climate simulations performed by MIROC3.2. The first ensemble was forced with changes in solar irradiance (Lean *et al.*, 1995) alone (hereinafter SOLR); the second was forced with changes in stratospheric aerosols due to volcanic activity (Sato *et al.*, 1993) alone (VLCN); the third was NTRL; and the last was ANTH. Each of the ensembles consists of 4 ensemble members.

To determine the relative importance of the external factors on early 20th century warming, the optimal detection/attribution approach (Allen and Stott, 2003) is applied to the model simulations and the observations for the 1900–1949 period. For the

detection/attribution analysis, 10 pentad (5-year) mean anomalies during the 1900–1949 period are used rather than the decadal (10-year) mean diagnostic used in section 5.2, since the typical recovery time from volcanic cooling is considered to be shorter than a decade. We require  $\geq 5$  pentads at each grid point; otherwise the pentad averages are omitted from the analysis. These anomalies are spatially truncated onto T4 spherical harmonics.

For signal-to-noise optimization, the observed and simulated SAT anomalies are projected onto the leading 20 EOFs of intra-ensemble variability (the variability among the 4 simulations, after subtracting the mean signal), rather than the 10 EOFs used in section 5.2, since the pentad mean data analyzed in the present study have twice the temporal resolution of the decadal mean data investigated in section 5.2. The results given below are insensitive to the exact level of truncation.

### 5.3.3 Detection and Attribution

Fig. 5.4 shows temporal variations of the global annual mean SAT for the observations and the model simulations. The observed warming over the early half of the 20th century is well simulated by NTRL, whereas ANTH shows little warming. Both SOLR and VLCN produce global warming during the same period, although the magnitude of the warming is less than that of the observations. In the SOLR and VLCN simulations, these warming trends can be explained by the increase of solar irradiance over the early 20th century (Lean *et al.*, 1995), and a recovery from the cooling due to heavy volcanism in the 1900s and the 1910s (Sato *et al.*, 1993), respectively.

Results of the 2-way (SOLR and VLCN) and 3-way (ANTH, SOLR, and VLCN) optimal detection/attribution analyses are given in Figs. 5.5 and 5.6, respectively. Fig. 5.5a depicts the scaling factors with their uncertainty ranges for SOLR and VLCN. The uncertainty ranges of both SOLR and VLCN signals are positive, and include unity, indicating that these simulated signals are detectable in the observed SAT changes, and their signal amplitudes are consistent with observations.

Best-estimate trends of global mean SAT are shown in Fig. 5.5b. The observed trend ( $\approx 0.9$  K/century) is well reproduced by a combination of the SOLR and VLCN signals. Each of the scaled trends for SOLR and VLCN is about a half of the observed trend (their best estimates are 0.34 K/century and 0.46 K/century, respectively). These results suggest that global warming over the early half of the 20th century is attributable to both effects of the solar irradiance change and the large volcanic activity, at least in MIROC3.2.

We also performed an ANTH, SOLR, and VLCN 3-way detection/attribution analysis (Fig. 5.6). The SOLR and VLCN signals show no changes from the 2-way analysis (Fig. 5.5), while the uncertainty range of the ANTH signal is poorly constrained as discussed in section 5.2. Therefore, the effects of the anthropogenic forcing are unclear, while the solar and volcanic responses are robust. Squared signal-to-noise ratio,  $(\text{SNR})^2$  defined by T02, of the ANTH response is 1.4, which is not significant at the one-sided 10% level of the  $F$ -test. This poor  $(\text{SNR})^2$  prevents us from achieving good estimates of the uncertainty range of the ANTH scaling factor. On the other hand,  $(\text{SNR})^2$  for SOLR and VLCN (2.0 and 2.1, respectively) are significant at the 10% level.

It should be noted that although the ANTH signal is not detected during the early 20th century with MIROC3.2, it is detected in a full-century or 1950–1999 analysis. For example, a detection/attribution analysis of the decadal mean ANTH and NTRL signals for 1900–1999 shows that their scaling factors are  $1.81$  <its 5–95% uncertainty range is  $1.38 \cdot 2.40$ > and  $1.03$  < $0.28 \cdot 2.01$ >, respectively. However, it has also been suggested that MIROC3.2 slightly underestimates the ANTH response, while the NTRL one is consistent with the observations.



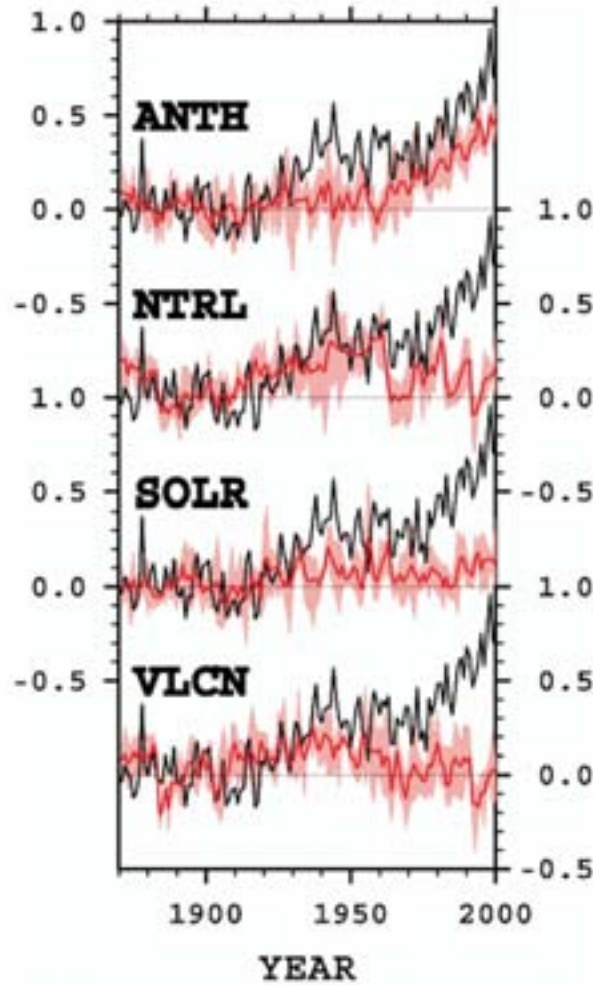


**Fig. 5.4: Temporal changes of global annual mean surface air temperature.** Black thick lines are anomalies from the 1881-1910 mean for the observations; red thick lines indicate the ensemble mean of the ANTH, NTRL, SOLR, and VLCN simulations. Maximum and minimum ranges from the individual simulations are shaded in pink.

This underestimation of the ANTH response is related to its smaller  $(\text{SNR})^2$ , making the estimate of the ANTH contribution unclear. Although it is important to investigate the reason why the ANTH response in MIROC3.2 is small, it is beyond the focus of the present study.

To make a more direct comparison with the results of section 5.2, the SOLR and VLCN 2-way analysis was also performed with decadal mean data using the leading 10 eigenvectors. The scaling factors for SOLR and VLCN are  $2.41 <0.93 \cdot 6.17>$  and  $0.71 <-1.4 \cdot 2.2>$ , respectively. The solar signal is detected and still consistent with the observed response, although with an increased best-estimate amplitude over that obtained from the pentad mean analysis. On the other hand, the volcanic signal is not detected. A lack of a detectable volcanic signal when using the decadal mean diagnostic is expected since, as already mentioned, a decade is longer than the typical recovery time of a large volcanic activity, hence any response in SAT is likely to be smoothed out. The increased best-estimate scaling factor on the solar response is probably indicative of a weaker solar signal in the decadal mean diagnostic, which could arise from larger smoothing of the response to the 11-year solar

cycle. S03 also found an increase in the scaling factor for the solar signal when going from pentad to decadal mean analysis. Decreasing the temporal resolution of the data, which reduces the number of degrees of freedom in the SAT anomalies, inevitably leads to increased degeneracy between the solar and volcanic responses, and thus reduces the ability of the regression to distinguish between the signals. Together these factors are likely to be responsible for the increased and much less constrained scaling factor for the solar signal when we move from analyzing pentad mean data to decadal mean data. We do note, however, that the scaling factor on the decadal mean solar signal is consistent with the scaling factor on the solar response obtained from the pentad mean analysis.

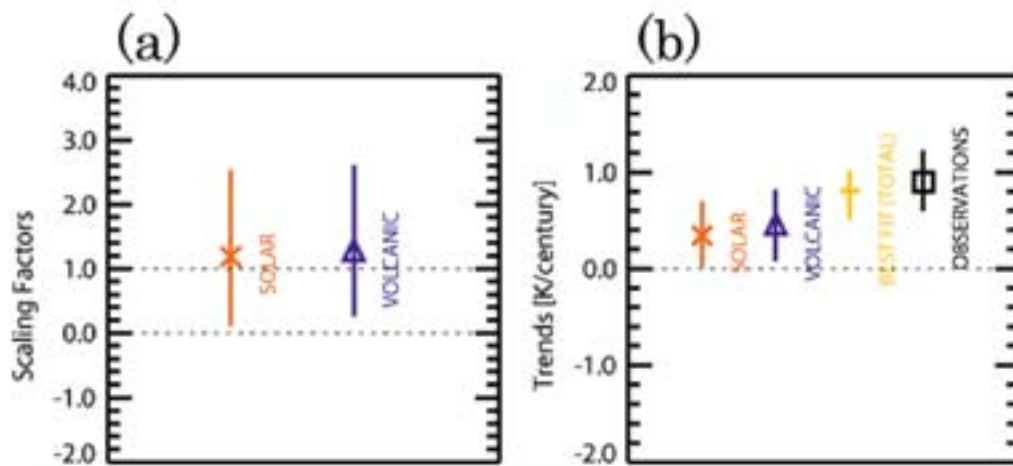


**Fig. 5.5: Best estimates of (a) scaling factors and (b) linear trends (K/century) with 5%-95% uncertainty ranges for the SOLR and VLCN in a 2-way analysis.** The orange error bar with an asterisk and purple error bar with a triangle indicate SOLR and VLCN, respectively. Also shown in (b) are the total reconstructed trend from the regression model (yellow error bar with a plus) and the observed trend (black error bar with a square).

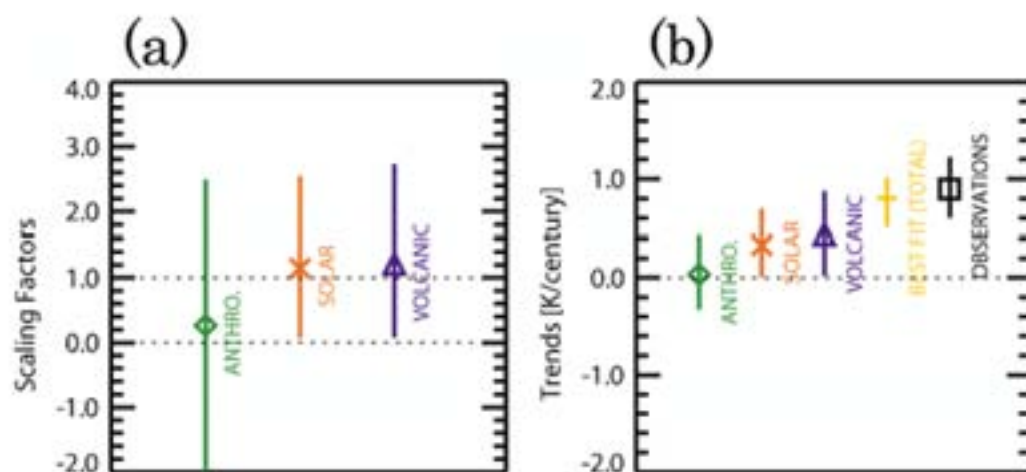


**Fig. 5.6: Same as Fig. 5.5, except for the ANTH, SOLR, and VLCN 3-way analysis.** The green error bar with a diamond indicates the estimated ANTH signal.

There is uncertainty in the solar and volcanic forcings in the early part of the 20th century, and the solar forcing seems to be less certain than the volcanic forcing (e.g., Foukal *et al.*, 2004; Ammann *et al.*, 2003). To test the sensitivity of our results, it is worthwhile to analyze additional ensembles forced with other reconstructions of solar and volcanic forcing.

### 5.3.4 Comparison with the HadCM3 Model

The reconstructed solar response trend of MIROC3.2,  $0.34 < 0.04 \cdot \cdot 0.68 >$  K/century, is consistent with the results of S03, who according to Lean *et al.* (1995) found a trend due to solar of  $0.29 < 0.15 \cdot \cdot 0.46 >$  K/century from simulations of HadCM3 forced with solar irradiance changes. However, in HadCM3 the scaling factor for the solar signal is 2.64 (obtained from 1900–1999 analysis), compared to 1.19 in MIROC3.2, hence suggesting that the non-scaled response in MIROC3.2 to solar forcing is larger than that in HadCM3. Since the response to solar forcing in MIROC3.2 is consistent with the observed response, it shows that we can obtain a suitable magnitude of response to solar forcing without recourse to an additional physical process that may act to amplify the amplitude of the solar response, such as a solar-ozone feedback process (Haigh, 1996). However, it does not preclude that these additional influences are important and may have a discernible impact on SATs.

For the sake of future projections (Stott and Kettleborough, 2002), it is important to understand why these 2 models respond differently to solar forcing. The diagnosing method of the climate feedback parameter ( $\alpha$ ) derived by Gregory *et al.* (2004) enables us to compare sensitivities ( $S$ ) of MIROC3.2 to solar forcing and that of HadCM3. Note that smaller  $\alpha$  indicates greater  $S$ , since  $S$  is proportional to  $\alpha^{-1}$ . The  $\alpha$  of MIROC3.2 to solar irradiance increases is 1.07, which is less than that of HadCM3 (2.0; see Gregory *et al.* (2004)), demonstrating that MIROC3.2 has a larger sensitivity to solar forcing than HadCM3. Larger sensitivities would cause larger responses to the historical solar irradiance changes, making it easier to detect the solar signal. It is worth stressing that MIROC3.2's sensitivity to solar forcing ( $\alpha = 1.07$ ) is consistent with its sensitivity to GHGS forcing ( $\alpha = 1.13$ ), whereas HadCM3's sensitivities are inconsistent ( $\alpha = 2.0$  for solar, and  $\alpha = 1.26$  for GHGS), so this may highlight a puzzle for HadCM3.

There is also a large difference in the volcanic responses between the present study and S03, i.e., the volcanic signal is detectable in the present study, while it was not detected in S03. Forster and Collins (2004) and Yokohata *et al.* (2005) demonstrated that both HadCM3 and MIROC3.2 reproduce the SAT response to the Mt. Pinatubo eruption in June 1991 in good agreement with the observations. To compare the response of both CGCMs to a volcanic activity under better signal-to-noise ratios, we performed a volcanic super-eruption experiment (Jones *et al.*, 2005), which simulates the response to the aerosol optical depth changes following a volcanic activity which is 100 times larger than the Mt. Pinatubo eruption. MIROC3.2 has longer relaxation time to the volcanic super-eruption (recovering to half amplitude of peak cooling by  $\approx 7$  years) than HadCM3 ( $\approx 5$  years; see Jones *et al.* (2005)), although the peak cooling amplitude of MIROC3.2 (9.7 K) is slightly less than that of HadCM3 (10.7 K) (not shown). This difference in the relaxation time to the volcanic eruption may cause different estimates of the volcanic contribution to the early century warming: with the model possessing longer relaxation time, the model volcanic signal tends to be less smoothed out by the temporal low-pass filter (pentad mean) applied in the detection/attribution analysis, with the likely result that the volcanic signal can be detected more easily. However, it should be noted that because of non-linear changes in ocean circulation, a volcanic super-eruption might not be representative of the response time for more regular eruptions.

### 5.3.5 Discussion

We investigated the relative roles of solar and volcanic contributions to global warming over the early half of the 20th century. By applying the optimal detection/attribution methodology to the observations and the MIROC3.2 simulations, we suggested that both solar and volcanic influences are detectable in the observed early warming. On the other hand, the uncertainty in the anthropogenic contribution is not successfully constrained, since its signal is probably underestimated.

Climate responses to solar and volcanic forcings in MIROC3.2 were compared with HadCM3. MIROC3.2 has larger climate sensitivities to the solar forcing than HadCM3 by a factor of 2. Unlike HadCM3, the solar sensitivity of MIROC3.2 is consistent with its greenhouse gas sensitivity, and therefore, MIROC3.2 seems to be telling a simpler story than HadCM3. Furthermore, MIROC3.2 has longer relaxation times to volcanic cooling than HadCM3. These differences would affect the detection/attribution of the past climate change, and also affect estimates of the uncertainty of future climate projection. Since it is still unclear why there are large uncertainties in climate responses to solar and volcanic forcings, it is necessary to compare mechanisms determining climate responses to external forcing factors among various CGCMs.

## 5.4 Causes of the Changes in SAT during the Mid-20th Century

### 5.4.1 Goals of This Section

The Earth's near-surface temperature in the mid-20th century, from the mid-1940s to the mid-1970s, shows a slight cooling, while apparent global warming has occurred in both the early and late 20th century (IPCC, 2001 and references therein). The likely causes of global warming in these periods has been the focus of several studies using state-of-the-art coupled atmosphere-ocean models (climate models) (e.g., Delworth and Knutson, 2000; Tett *et al.*, 2002; Meehl *et al.*, 2004a; Nozawa *et al.*, 2005); however, there is little literature that refers to the cause of mid-century cooling.

Wigley *et al.* (1997) showed that the leveling off of solar irradiance in mid-century brought a reasonable cooling trend to their energy-balance model, whereas Andronova and Schlesinger (2000) suggested that an internal oscillation over the North Atlantic and its adjacent land area with a period of 65-70 years is a possible explanation of the cooling in the mid-century. Tett *et al.* (1999) proposed that the cooling effect of sulfate aerosols could balance the effect of greenhouse gases in mid-century giving a slight cooling trend. However, none has explicitly considered the impact of carbonaceous aerosols, which should have a large impact on the near-surface temperature (e.g., Ramanathan *et al.*, 2001).

Using MIROC3.2 forced with a range of different anthropogenic aerosol emissions, we investigate the impact of increasing emissions of carbonaceous aerosols on the mid-20th century SAT change. A detailed comparison is made between the observed spatial and temporal temperature change over this period and the spatial and temporal responses simulated by MIROC3.2.

### 5.4.2 Experiments

We performed 3 experiments, spanning the years from 1850 to 2000. Each experiment was forced by a different combination of historical changes in anthropogenic aerosol emissions in order to investigate the impact of such changes on 20th century climate. In the experiment labeled "FULL", the carbonaceous (OC+BC) aerosols and the precursors of the sulfate aerosols (SO<sub>2</sub>) increase according to estimations derived from country-based inventory

data. The emissions of  $\text{SO}_2$  are obtained from Lefohn *et al.* (1999), while those of carbonaceous aerosols are provided by Nozawa and Kurokawa (2007), a brief description of which can be found in Takemura *et al.* (2005). The 2 other experiments were labeled “CEFX,” in which only  $\text{SO}_2$  emissions were increased, and “AEFX,” in which both the  $\text{SO}_2$  and carbonaceous emissions were fixed at the 1850 level. In addition, all of the experiments were driven by several other major external forcings relevant to the 20th century. These include historical changes in well-mixed greenhouse gases ( $\text{CO}_2$ ,  $\text{CH}_4$ ,  $\text{N}_2\text{O}$ , and halocarbons), stratospheric ozone, tropospheric ozone estimated by a chemical model, land use, solar irradiance, and stratospheric volcanic aerosol. Each experiment consists of 4 ensemble members, starting from different initial conditions taken from a 900-year control simulation, at intervals of 100 years.

### 5.4.3 Results

The evolutions of global annual mean SAT over the 20th century derived from the 3 experiments are compared with observations (Jones and Moberg, 2003) in Fig. 5.7. Until approximately 1940, the calculated warming from the end of the 19th century in each of the 3 experiments is similar to the observed warming during the same period. After 1940, however, AEFX fails to reproduce the slight cooling in the mid-century, and overestimates global warming during the late 20th century, resulting in a temperature increase at the end of the 20th century twice as large as that observed. Compared to AEFX, since 1940, CEFX and FULL better trace the course of observed global annual mean changes in SAT. A comparison of those 2 experiments with AEFX demonstrates a significant offsetting of greenhouse-gas-induced global warming by global cooling due to increased anthropogenic aerosols. However, the better correspondence between the observed SAT change and modeled SAT change in CEFX than in FULL, especially after about 1960, could indicate that the additional cooling stemming from the carbonaceous aerosols used in the model during this period could be slightly too large.

To take a closer look at the effect of increased carbonaceous aerosols on changes in SAT after 1940, we now examine the geographical distribution of the linear trends (trend pattern) in SAT. In the latter part of the 20th century (1976-2000), both CEFX and FULL predict significant global-mean warming, but FULL catches the features of the observed trend pattern better than CEFX (not shown). This would suggest considerable regional impacts of carbonaceous aerosols on SAT in the latter part of the 20th century as described by Menon *et al.* (2002) or Ramanathan *et al.* (2005), for example; however, the analysis of such an impact is beyond the scope of this paper and should be reported elsewhere.

Around mid-century, the trend patterns from each of the 3 experiments differ from each other (Fig. 5.8). Comparing the 3 experiments and the observations, it is clear that the trend pattern from FULL gives the best agreement with the observed trend pattern, although the large-scale warming trend that occurred over Eurasia is not reproduced. When we measure the correspondence between the trend pattern from each experiment with the observed trend pattern using both centered- and uncentered-pattern correlation statistics (Tett *et al.*, 1996), the values of the correlation statistics for the FULL experiment are high and statistically significant, while they are low and generally insignificant for the other 2 experiments (see lower numbers for each experiment in Fig. 5.8). Such is the case not only for the period shown in Fig. 5.8 (1942-1979), but also for other periods around the mid-20th century (not shown). The regional cooling trends for southern China, sub-Saharan Africa, Central-South America (except Argentina), and the equatorial Atlantic coast, which are reproduced only in FULL, improve the correspondence with the trend pattern from the observations. In FULL,

increases in the carbonaceous aerosol loading mainly originating from biomass burning were simulated in these regions (not shown) implying that increased levels of such aerosols had a negative radiative forcing (RF) in those regions.

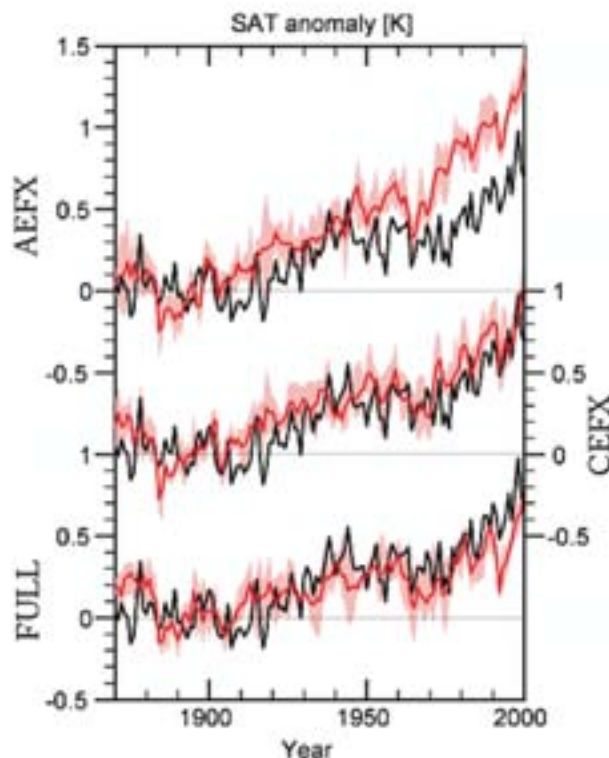


**Fig. 5.7: Time series of annual and global mean T2 from the observations (Johns and Moberg, 2003) (black thick lines) and from the AEFX, CEFX, and FULL experiments expressed as anomalies relative to the 1881-1910 mean (K).** The ensemble means (thick red lines) and the ensemble member range (minimum-to-maximum; pink shade) are shown. In calculating the annual global means for the model, the model data were masked at times and locations where observational data were not available. More than 10 months of data were required at each location to calculate the annual mean value.

The instantaneous RFs due to carbonaceous and sulfate aerosols were calculated separately using the atmospheric component of MIROC3.2. The RFs were calculated between 1900 and 2000 at intervals of 10 years. The estimated global annual mean net direct RFs due to BC and OC for the year 2000 condition at the Earth's surface (at the top of the atmosphere) are  $-0.78$  and  $-0.36$  ( $+0.42$  and  $-0.28$ )  $\text{W/m}^2$ , respectively. These estimates compare well with the previous estimates (IPCC, 2001 and references therein). The trend patterns of net RF at the surface show that the increase in both carbonaceous and sulfate aerosols invoked in FULL caused cooling of most of the Earth's surface between 1940 and 1980 (Figs. 5.9a-d). However, the geographical distributions of the radiative cooling trend caused by increases in both of these anthropogenic aerosols are completely different from each other. The above-mentioned regions, in which the cooling trend for SAT was only predicted by FULL in Fig. 5.8, coincide well with the regions where the radiative cooling due to the first-indirect effect of carbonaceous aerosols is reinforced, while the cooling due to both the first-indirect and direct effects of sulfate aerosols is unlikely to account for the regional SAT cooling trends



in those regions. The radiative cooling due to the direct effect of carbonaceous aerosols is also reinforced in the above-mentioned regions (Fig. 5.9a) because of the large absorption of incoming solar radiation (SR) by BC, which reduces the SR reaching the surface. BC also absorbs the upward SR reflected by the surface or clouds, resulting in a positive RF at the tropopause (Fig. 5.9e). Such absorptions of SR by BC warm the surrounding air, and then the thermal radiation from the warmed air warm the surface. Unfortunately, such surface warming cannot be precisely estimated from the instantaneous RFs; therefore, we cannot state how large is the net impact by the direct effect of carbonaceous aerosols on the change in SAT.

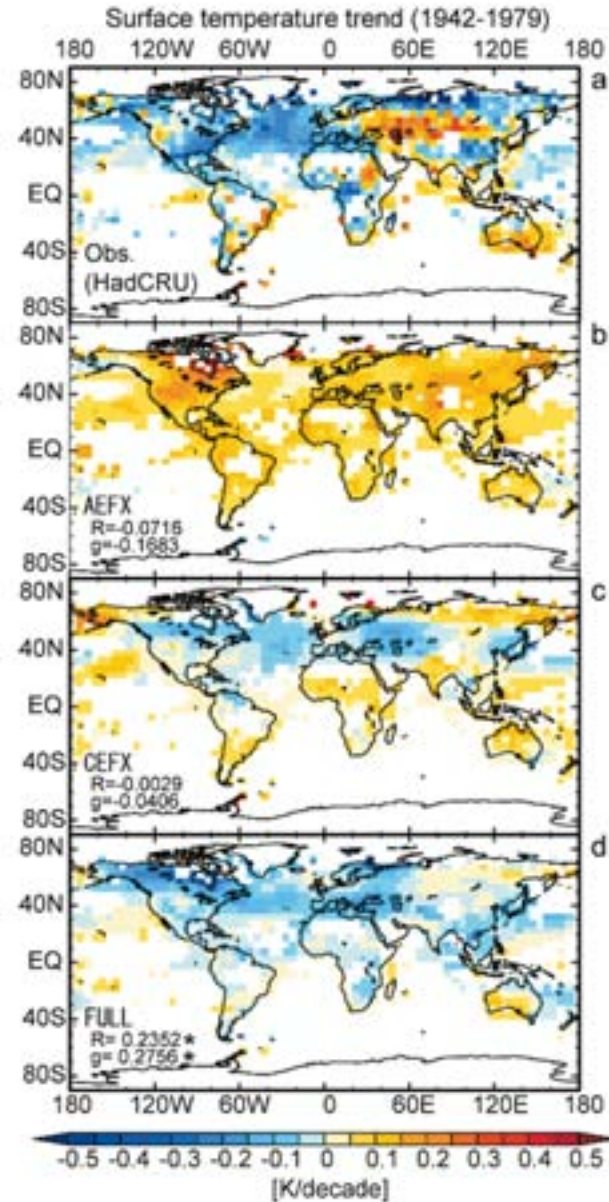


**Fig. 5.8: Geographical distributions of linear trends (K/decade) of T2 from 1942 to 1979 for (a) the observations (Johns and Moberg, 2003), (b) AEFX, (c) CEFX, and (d) FULL. The trends were calculated from the annual mean data only for those grids where annual data were available for at least 2/3 of the 38 years in question and distributed in time without significant bias. The values of the centered (R) and uncentered (g) pattern correlation statistics are shown for each experiment. An asterisk denotes that the value is outside the  $\pm 2\sigma$  range of the probability density function (PDF) of both statistics as estimated from the control simulation.**

Finally, we formally tested the consistency between the spatio-temporal changes observed for SAT and the simulated values of SAT by using a standard optimal fingerprinting method (Allen and Tett, 1999; Allen and Stott, 2003). Fig. 5.10 shows the best-estimate values of the scaling factor,  $\beta$ , and their uncertainty ranges for the spatio-temporal changes between 1940 and 1979 for the 3 experiments.  $\beta$  is only significantly positive for FULL with a best-estimate value of about 1, while the values for CEFX and AEFX cannot be statistically distinguished from 0. This implies that the observed spatio-temporal change in SAT in the mid-20th century that results in a slight global cooling cannot be attributed to any combination of climate forcings in which an increase in carbonaceous aerosols is not included. Furthermore, we regressed the observed spatio-temporal change in SAT onto the 2 model-simulated responses from FULL and CEFX to estimate the  $\beta$  values for the carbonaceous aerosol forcing alone and the sum of all other forcings by using a linear transformation method (Tett *et al.*, 2002). The best-estimated values of  $\beta$  for carbonaceous aerosol forcing and the sum of all other forcings are  $2.19 <0.87\text{--}7.92>$  and  $1.03 <0.17\text{--}3.18>$  respectively. The uncertainty range of  $\beta$  for the carbonaceous aerosol forcing does not include 0, indicating that we can detect the influence of carbonaceous aerosols in the observations in the presence of the other forcings. Moreover, the uncertainty on the amplitude of the carbonaceous aerosol signal includes 1; thus, our simulated signal is consistent with the observed response to carbonaceous aerosols in the mid-20th century, although the large value of  $\beta$  implies that our model possibly underestimates the signal.

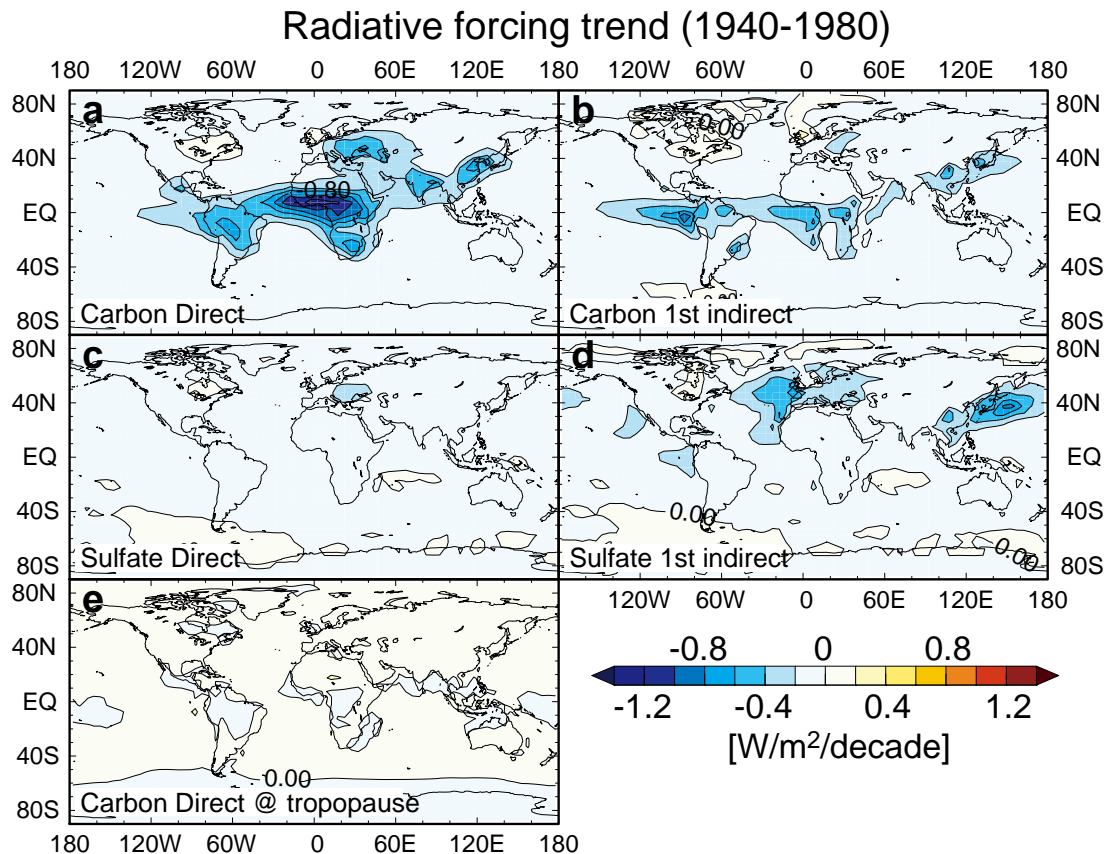


**Fig. 5.9: Geographical distributions of linear trends of net RFs from 1940 to 1980 from carbonaceous (a and b) and sulfate (c and d) aerosols for direct (a and c) and first-indirect (b and d) effects at the Earth's surface, while (e) shows (a) but in the tropopause. The linear trends were calculated using 5 annual mean values of RFs for 1940, 1950, 1960, 1970, and 1980.**



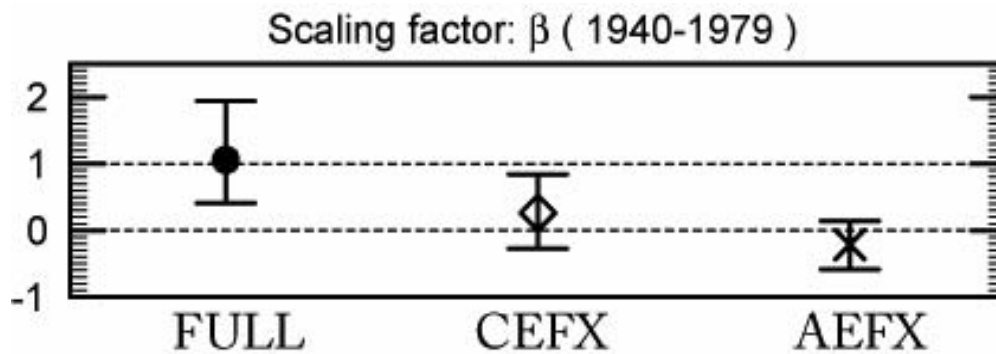


**Fig. 5.10: Scaling factors by which we must multiply the model-simulated spatio-temporal change of T2 (1940-1979) to reproduce the corresponding change in the observation.** The error bars show the 5%-95% uncertainty range due to internal variability estimated from the control simulation.

#### 5.4.4 Discussion

The SAT changes simulated by a climate model are investigated to demonstrate the impact of carbonaceous aerosols on the SAT trend in the mid-20th century. If we try to take into account the representation of both spatial and temporal trend patterns of SAT, the change in SAT that occurred in mid-century can only be reproduced adequately when we consider an increase in carbonaceous aerosol emissions. This demonstrates that radiative cooling due to increased levels of carbonaceous aerosols is an indispensable contributor to the slight cooling in annual global mean SAT in the mid-20th century.

We should note that the cooling trend of SAT in the mid-20th century in tropical land regions that was calculated in FULL could be attributed to an increase in carbonaceous aerosols from biomass burning (not shown). Although the historical emission levels of carbonaceous aerosols from biomass burning are uncertain, we estimated them assuming that their spatial distribution (Cooke and Willson, 1996) in the mid-1980s is unchanged time-wise, but that its value is scaled to the historical world population. This assumption is valid to a first-order approximation because a large part of the biomass burning that occurs in the tropics is relevant to agricultural activities (Crutzen and Andreae, 1990; Hao and Liu, 1994) that are normally traditional and indigenous. This implies that the regions in which biomass burning occurs may not have changed dramatically during the 20th century.

We cannot discuss the relative contributions of direct and indirect effects of carbonaceous aerosols, because of the difficulty in estimating the net impact of BC absorption of solar radiation on the surface temperature. Moreover, large uncertainty in the treatment of indirect effects in the model due to limited knowledge about aerosol-related atmospheric processes is another difficulty. Although these difficulties should be addressed to advance the present study, the present results clearly show the relative importance of carbonaceous aerosols for the SAT change in the mid-20th century with the use of a climate model and an optimal fingerprinting methodology.

## 5.5 Causes of the Changes in Temperature Extremes

### 5.5.1 Goals of This Section

Detection/attribution analyses of mean SAT have been reported in the previous sections. In addition to detection/attribution studies of mean temperature, it is important to study changes in temperature extremes, because these have large societal and health impacts (Easterling *et al.*, 2000; McMichael *et al.*, 2006). However, until recently, there has been no high-quality gridded dataset of daily temperature observations that covered a long time scale and global spatial scale, making it difficult to compare model simulations and observations. Recently, an effort was made to compile comprehensive global datasets that contain daily maximum/minimum temperatures, or extreme indices (Gleason *et al.*, 2002; Klein Tank *et al.*, 2002; Caesar *et al.*, 2006; Frich *et al.*, 2002; Alexander *et al.*, 2006 (hereinafter A06)), and impacts of human activity on some temperature extreme indices have been reported (Kiktev *et al.*, 2003). Christidis *et al.* (2005, hereinafter C05) is the first study that applied a standard detection/attribution approach to compare 20th century climate simulations performed by HadCM3 (Gordon *et al.*, 2000) and the new gridded observational dataset of daily maximum/minimum temperatures from Caesar *et al.* (2006). They investigated the annual warmest/coldest values of daily maximum/minimum temperatures, which had been employed to test the detectability of anthropogenic signals in a perfect model study (Hergel *et al.*, 2004). They found that human influences are detectable in changes in the annual warmest minimum temperature, and the annual coldest maximum/minimum temperatures from 1950 to 1999. However, human influence is not detectable in changes in the warmest maximum temperature, which has the smallest signal-to-noise ratio among these 4 indices.

Uncertainty about climate sensitivity causes different responses to external forcing among various CGCMs (IPCC, 2001), resulting in different estimates of contributors to past climate change (Shiogama *et al.*, 2006; section 5.3), and uncertainty of future climate projections (Stott *et al.*, 2006). Therefore, it is worth confirming the findings of C05 by carrying out the same detection/attribution analysis using a different CGCM, MIROC3.2 (K-1 model developers, 2004). MIROC3.2 has been utilized in several detection/attribution studies of monthly mean temperature changes (Nozawa *et al.*, 2005; Nagashima *et al.*, 2006; Shiogama *et al.*, 2006). This is the first aim of the present study. The second aim is to extend the analysis of C05 to other important temperature extreme indices. Furthermore, we estimate the relative importance of well-mixed GHGs and other forcing factors (including aerosol forcing) to past changes in temperature extremes. This is expected to yield valuable information about the causes of past climate change and the uncertainty of future climate projection.

### 5.5.2 Data and Experiments

We use HadGHCND, a newly gridded dataset of daily near-surface maximum/minimum temperature observations (Caesar *et al.*, 2006). This dataset covers land areas mainly over the northern hemisphere and Australia on a 2.5° lat by 3.75° lon grid during the period from 1946 to 2000.

We compare the observations with 3 ensembles of 20th century climate simulations performed by MIROC3.2, GHGS, ANTH, and FULL. Each ensemble consists of 4 runs starting from different initial conditions taken from a 2270-year stable pre-industrial control run, and the ensemble mean is analyzed. Model data are bi-linearly interpolated in latitude and longitude from its T42 grid to the grid of the observation data.

The present study investigates changes in the “annual most extreme value” indices examined by Hergel *et al.* (2004) and C05:

- warmest day (annual maximum of daily maximum temperature),
- warmest night (annual maximum of daily minimum temperature),
- coldest day (annual minimum of daily maximum temperature),
- coldest night (annual minimum of daily minimum temperature).

In addition, we analyze 2 “number of annual occurrence” indices (A06):

- summer days (annual number of days with daily maximum temperature  $> 25^{\circ}\text{C}$ ),
- frost days (annual number of days with daily minimum temperature  $< 0^{\circ}\text{C}$ ).

For both the observations and the model, these annual indices are computed when there are observations for more than 182 days per year at each grid. When annual indices exist for every year from 1950 to 1999, we compute 5 decadal averaged anomalies from the 1950 to 1999 mean.

Detection/attribution analysis is carried out by applying the optimal fingerprinting method (Allen and Stott, 2003). To optimize the signal-to-noise ratio, before the regression analysis, observed and model anomalies are spatially truncated onto T4 spherical harmonics and projected onto the leading 10 eigenvectors obtained from half of the 2270-year control run. The results given below are insensitive to the exact number of eigenvectors used.

### 5.5.3 Results

Fig. 5.11 shows the changes in the warmest night during the second half of the 20th century for the observations and the model. Warming is found over large parts of the globe in the observations and all the simulations. GHGS shows larger warming than the observations. Cooling due to anthropogenic aerosols cancels some degree of the GHGS warming, resulting in a smaller warming in ANTH than found in GHGS. The difference between ANTH and FULL is not pronounced, suggesting that natural forcing factors have little impact on the warmest night during this period. Larger global warming is found in the coldest day/night than the warmest night in both the observations and the model (not shown). The warmest day shows the smallest warming trend among these 4 indices (not shown).

The significance of the response to external forcing is tested by single detection/attribution analyses for FULL, ANTH, and GHGS (Fig. 5.12). For the warmest night and the coldest day/night, the scaling factors of GHGS are positive, suggesting that the influences of GHGS are detectable in the observed changes in these 3 indices. In the warmest night, the scaling factor of GHGS is smaller than 1, indicating that the response amplitude of GHGS is larger than the observations. The uncertainty range for the scaling factor of ANTH includes 1, indicating that the response amplitude of ANTH is consistent with that of the observations. We suggest that, together with the GHGS forcing, anthropogenic aerosol forcing is essential to reproduce the observed changes in the warmest night. Little difference is found between ANTH and FULL. It seems that natural forcings have no significant impact on the warmest night during this period. For the coldest day/night, the scaling factors of GHGS are consistent with 1, and the ANTH and FULL signals are larger than 1. These ANTH and FULL responses are underestimated. Human influence is not detectable in the warmest day.

These results of warmest/coldest day/night are similar and generally in agreement with that of C05. Thus, the present study confirms the robustness of the results of C05. On the other hand, there are interesting differences between these studies. ANTH and FULL of MIROC3.2 have larger scaling factors than HadCM3, indicating that the ANTH and FULL responses in MIROC3.2 are smaller than in HadCM3. MIROC3.2 may have larger aerosol cooling than HadCM3.

Decreases in the number of frost days are found in the observations and the model (Fig.

5.13). The warming due to GHGS forcing results in large decreases in frost days. Cooling due to aerosol causes smaller signals in ANTH than in GHGS. Previous studies have also shown anthropogenic influences on the decrease in frost days (Frich *et al.*, 2002; Kiktev *et al.*, 2003; Meehl *et al.*, 2004b; A06; Tebaldi *et al.*, 2006). Natural forcing induces little difference between ANTH and FULL. Increases in summer days are found in the observations and the simulations, but their amplitudes are smaller than the frost days (not shown). Single detection/attribution analyses show that the signal amplitude of FULL in the frost days is consistent with the observations, while anthropogenic influence is not detectable in the summer days (Fig. 5.12).

To evaluate the relative contributions from the GHGS forcing and the other factors (hereinafter FULL–GHGS), we apply a multi detection/attribution analysis for [GHGS, FULL–GHGS], which are obtained by a linear transformation of multi-detection/attribution analysis for [GHGS, FULL] (Allen and Tett, 1999). The radiative forcing shown by Takemura *et al.* (2006) indicates that the FULL–GHGS forcing should be dominated by aerosol forcing. Fig. 5.14a shows scaling factors for GHGS and FULL–GHGS. For the warmest night and the frost days, both the signal amplitudes of GHGS and FULL–GHGS are consistent with the observations. On the other hand, for the coldest day/night, the GHGS responses are underestimated, while the signal amplitudes of FULL–GHGS are consistent with the observations. For the warmest day and the summer days, the GHGS and FULL–GHGS influences are not detectable.

Figs. 5.14b–d depict global mean trends in the extreme indices attributable to the influences of GHGS and FULL–GHGS. Observed trends are well reproduced by the total trends from the regression model. For the warmest night and the coldest day/night, the FULL–GHGS cooling cancels about half of the GHGS warming. The increases in the number of frost days due to the FULL–GHGS cooling counteract the decreases due to the GHGS warming, reducing the amplitude of the changes in the frost days to half of the GHGS response. For the warmest day and the summer days, the best estimates of the observed trends are positive, but not significant. It will be necessary to analyze another index with better signal-to-noise ratios to detect anthropogenic influences from the daily maximum temperatures of the warm season.

#### 5.5.4 Discussion

The present study corroborates the findings of C05, which utilized HadCM3, regarding the changes in the annual warmest/coldest day/night from 1950 to 1999, by using another CGCM, MIROC3.2. We confirmed that the influences of rising greenhouse gas concentrations are detectable in past changes in the warmest night and the coldest day/night. Also, we showed that MIROC3.2 has smaller responses to anthropogenic forcing than HadCM3. To understand the different responses to external forcing between these 2 models, and to achieve a more robust estimate of the reasons for past changes in extreme temperatures, we have started working on a multi-model analysis with these models. The results will be reported in another paper.

The observed decreases in frost days are attributable to decreases due to anthropogenic influences. On the other hand, it is difficult to detect human influences in the summer days and the warmest day, since these indices have poor signal-to-noise ratios.

Furthermore, we separate the contributions of greenhouse gas warming and the cooling due to other forcings to the changes in the temperature extremes with the exceptions of the warmest day and the summer days. The other forcings (aerosol cooling likely being the dominant component) mitigate the greenhouse gas influences by about half of the amplitude.

Growing knowledge of the serious health effects of aerosols should lead to efforts to reduce aerosol emissions (Andreae *et al.*, 2005). In the future, a rapid decline of aerosol emissions coupled with rising greenhouse gas concentrations is likely to result in larger changes in the temperature extremes in addition to the mean temperature (Andreae *et al.*, 2005). Amplification of changes in the temperature extremes could induce more serious societal and health impacts than changes in the mean temperature alone.

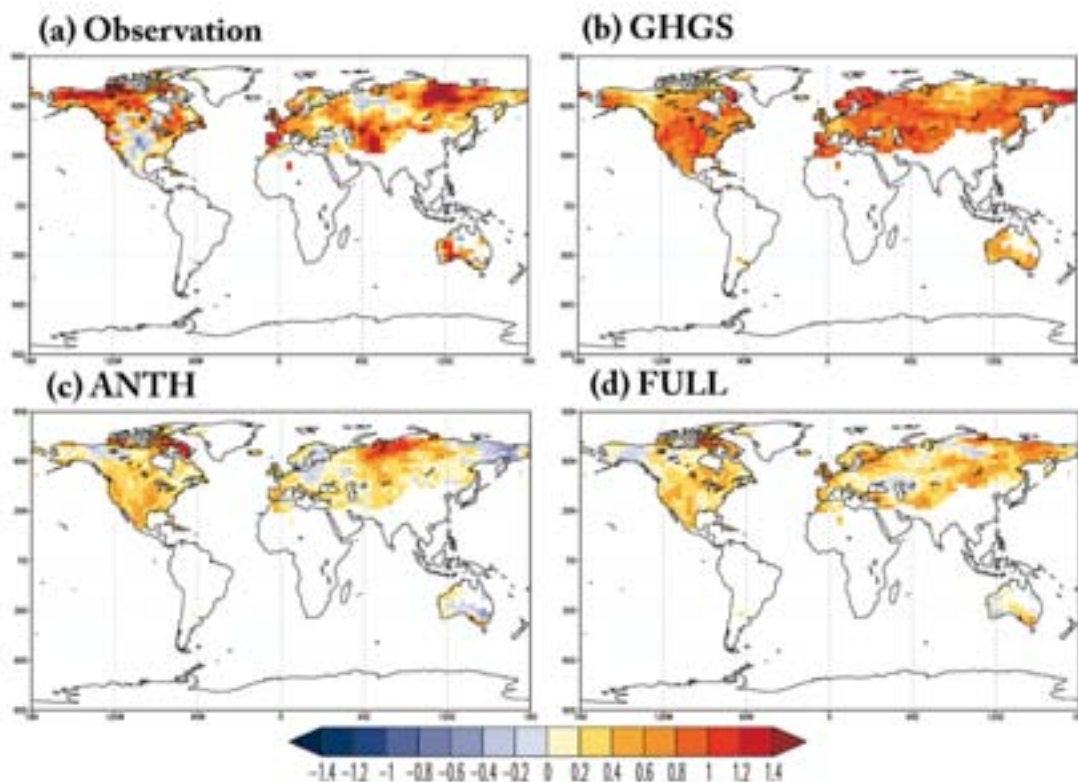


Fig. 5.11: Changes in the warmest night (1980–1999 minus 1950–1969; K) for (a) the observations, (b) GHGS, (c) ANTH, and (d) FULL.

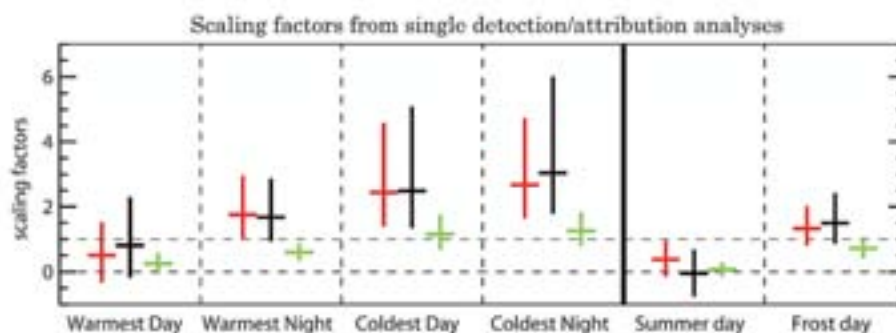
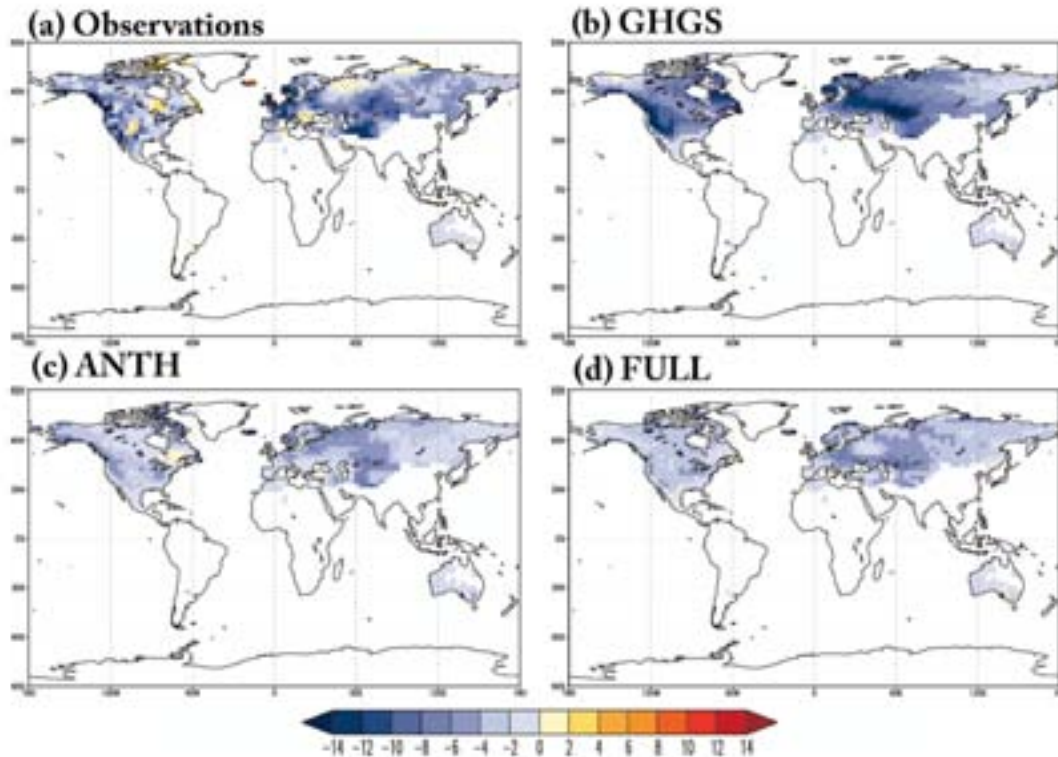
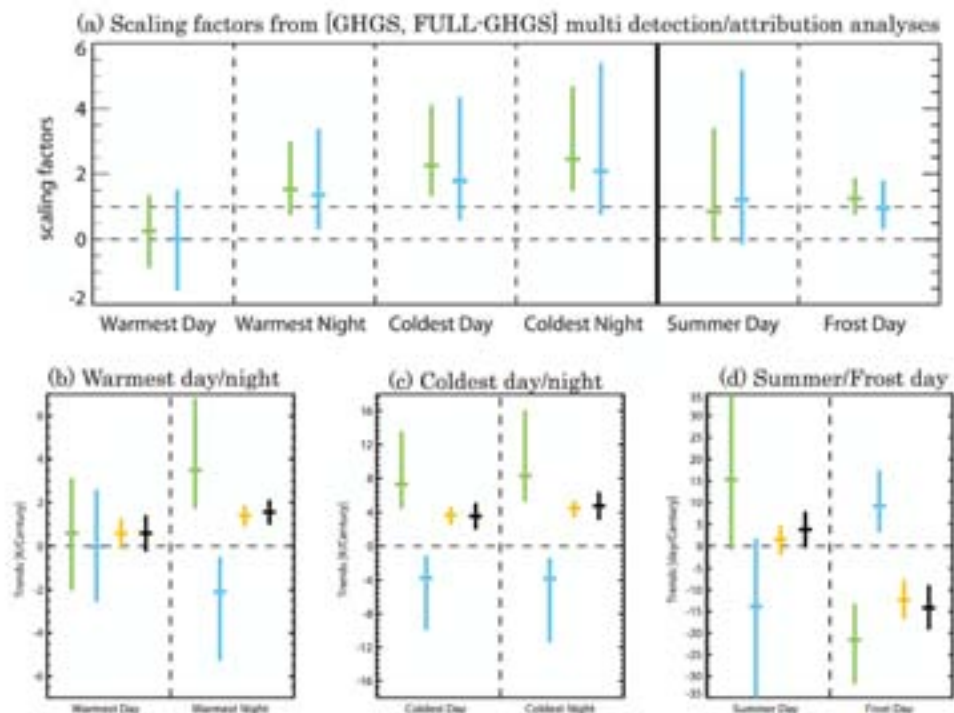


Fig. 5.12: Scaling factors and their 5%–95% uncertainty ranges from single detection/attribution analyses. Red, black, and green bars indicate scaling factors of FULL, ANTH, and GHGS, respectively.



**Fig. 5.13: Changes in the frost days (1980–1999 minus 1950–1969; days) for (a) the observations, (b) GHGS, (c) ANTH, and (d) FULL.**



**Fig. 5.14: (a) Scaling factors and their 5%–95% uncertainty ranges from [GHGS, FULL-GHGS] multi detection/attribution analyses. Green and blue bars indicate scaling factors of GHGS and FULL-GHGS, respectively. The lower 3 panels are global mean linear trends with 5%–95% uncertainty ranges for (b) warmest day/night, (c) coldest day/night, and (d) summer/frost days. Green and blue bars show GHGS and FULL-GHGS, which are inflated by their scaling factors, respectively. The yellow bar is the total reconstructed trend from the regression model. The observed trends are in black.**

## References

- Alexander, L.V., et al. (2006) Global observed changes in daily climate extremes of temperature and precipitation. *J. Geophys. Res.*, 111, D05109, doi:10.1029/2005JD006290.
- Allen, M.R., Tett, S.F.B. (1999) Checking for model consistency in optimal fingerprinting. *Clim. Dyn.*, 15, 419-434.
- Allen, M.R., Stott, P.A. (2003) Estimating signal amplitudes in optimal fingerprinting, part I: theory. *Clim. Dyn.*, 21, 477-491.
- Ammann, C.M., Meehl, G.A., Washington, W.M., Zender, C.S. (2003) A monthly and latitudinally varying volcanic forcing dataset in simulations of 20th century climate. *Geophys. Res. Lett.*, 30(12), 1657, doi:10.1029/2003GL016875.
- Andreae, M.O., Jones, C.D., Cox, P.M. (2005) Strong present-day aerosol cooling implies a hot future. *Nature*, 435, 1187-1190, doi:10.1038/nature03671.
- Andronova, N.G., Schlesinger, M.E. (2000) Causes of global temperature changes during the 19th and 20th centuries. *Geophys. Res. Lett.*, 20, 2137-2140.
- Broccoli, A.J., Dixon, K.W., Delworth, T.L., Knutson, T.R., Stouffer, R.J. (2003) Twentieth-century temperature and precipitation trends in ensemble climate simulations including natural and anthropogenic forcing. *J. Geophys. Res.*, 108(D24), doi:10.1029/2003JD003812.
- Caesar, J., Alexander, L., Vose, R. (2006) Large-scale changes in observed daily maximum and minimum temperatures: Creation and analysis of a new gridded data set. *J. Geophys. Res.*, 111, D05101, doi:10.1029/2005JD006280.
- Christidis, N., Stott, P.A., Brown, S., Hegerl, G.C., Caesar, J. (2005) Detection of changes in temperature extremes during the second half of the 20th century. *Geophys. Res. Lett.*, 32, L20716, doi:10.1029/2005GL023885.
- Cooke, W.F., Wilson, J.J.N. (1996) A global black carbon aerosol model. *J. Geophys. Res.*, 101, 19395-19409.
- Crutzen, P.J., Andreae, M.O. (1990) Biomass burning in the tropics: Impact on atmospheric chemistry and biogeochemical cycles. *Science*, 250, 1669-1678.
- Delworth, T.L., Knutson, T.R. (2000) Simulation of early 20th century global warming. *Science*, 287, 2246-2250.
- Easterling, D.R., Meehl, G.A., Parmesan, C., Changnon, S.A., Karl, T.R., Mearns, L.O. (2000) Climate Extremes: Observations, Modeling, and Impacts. *Science*, 289, 2068-2074.
- Forster, P.M. de F., Collins, M. (2004) Quantifying the water vapour feedback associated with post-Pinatubo global cooling. *Clim. Dyn.* 23, 207-214, DOI:10.1007/s00382-004-0431-z.
- Foukal, P., North, G., Wigley, T. (2004) A stellar view on solar variations and climate. *Science*, 306(5693), 68-69, DOI: 10.1126/science.1101694.
- Frich, P., Alexander, L.V., Della-Martin, P., Gleason, B., Haylock, M., Klein Tank, A.M.G., Peterson, T. (2002) Observed coherent changes in climatic extremes during the second half of the twentieth century. *Clim. Res.*, 19, 193-212.
- Gleason, B., Groisman, P., Peterson, T.C., Vose, R., Ezell, R. (2002) A new global daily temperature and precipitation dataset, paper presented at 13th Symposium on Global Change and Climate Variations, Am. Meteorol. Soc., Orlando, FL.
- Gordon, C., Cooper, C., Banks, H., Gregory, J.M., Johns, T.C., Mitchell, J.F.B., Wood, R.A. (2000) The simulation of SST, sea ice extents and ocean heat transports in a version of the Hadley Centre coupled model without flux adjustments. *Clim. Dyn.*, 16, 147-168.
- Gregory, J.M., Ingram, W.J., Palmer, M.A., Jones, G.S., Stott, P.A., Thorpe, R.B., Lowe, J.A., Johns, T.C., Williams, K.D. (2004) A new method for diagnosing radiative forcing and climate sensitivity. *Geophys. Res. Lett.*, 31, L03205. doi:10.1029/2003GL018747.
- Haigh, J.D. (1996) Impact of solar variability on climate. *Science*, 272, 981-984.
- Hao, W.M., Liu, M.-H. (1994) Spatial and temporal distribution of tropical biomass burning. *Global Biogeochem. Cyc.*, 8, 495-503.
- Hasselmann, K. (1997) Optimal fingerprints for the detection of time dependent climate change. *J. Climate*, 6, 1957-1971.
- Hegerl, G.C., Crowley, T.J., Baum, S.K., Kim, K.-Y., Hyde, W.T. (2003) Detection of volcanic, solar and greenhouse gas signals in paleo-reconstructions of Northern Hemispheric temperature. *Geophys. Res. Lett.*, 30(5), 1242, doi:10.1029/2002GL016635.
- Hegerl, G.C., Crowley, T.J., Hyde, W.T., Frame, D.J. (2006) Climate sensitivity constrained by temperature reconstructions over the past seven centuries. *Nature*, 440, 1029-1032, doi:10.1038/nature04679.



- Hegerl, G.C., Zwiers, F.W., Stott, P.A., Kharin, V.V. (2004) Detectability of anthropogenic changes in annual temperature and precipitation extremes. *J. Clim.*, 17, 3683-3700.
- Hirabayashi, Y., Kanae, S., Struthers, I., Oki, T. (2005) A 100-year (1901-2000) global retrospective estimation of the terrestrial water cycle. *J. Geophys. Res.*, 110, D19101, doi:10.1029/2004JD005492.
- IPCC (2001) *Climate Change 2001: The Scientific Basis. Contribution of Working Group I to the Third Assessment Report of the Intergovernmental Panel on Climate Change*, Houghton, J.T. et al. (eds.), Cambridge Univ. Press, New York.
- International ad hoc Detection and Attribution Group (2005) Detecting and attributing external influences on the climate system: A review of recent advances. *J. Clim.*, 18, 1291-1314.
- Johns, T.C., Gregory, J.M., Ingram, W.J., Johnson, C.E., Jones, A., Lowe, J.A., Mitchell, J.F.B., Roberts, D.L., Sexton, D.M.H., Stevenson, D.S., et al. (2003) Anthropogenic climate change for 1860 to 2100 simulated with the HadCM3 model under updated emissions scenarios. *Clim. Dyn.*, 20, 583-612.
- Jones, G.S., Gregory, J.M., Stott, P.A., Tett, S.F.B., Thorpe, R.B. (2005) An AOGCM simulation of the climate response to a volcanic super-eruption. *Clim. Dyn.*, 25, 725-738, DOI 10.1007/s00382-005-0066-8.
- Jones, P.D., Moberg, A. (2003) Hemispheric and large-scale surface air temperature variations: An extensive revision and an update to 2001. *J. Climate*, 16, 206-223.
- K-1 model developers (2004) K-1 coupled GCM (MIROC) description, K-1 technical report. 1, Hasumi, H., Emori, S. (eds.), Center for Climate System Research, University of Tokyo, Tokyo, 34pp.
- Kiktev, D., Sexton, D.M.H., Alexander, L., Folland, C.K. (2003) Comparison of modelled and observed trends in indices of daily climate extremes. *J. Clim.*, 16, 3560-3571.
- Klein Tank, A.M.G., et al. (2002) Daily surface air temperature and precipitation dataset 1901-1999 for European Climate Assessment (ECA). *Int. J. Climatol.*, 22, 1441-1453.
- Lean, J., Beer, J., Bradley, R. (1995) Reconstruction of solar irradiance since 1610: Implications for climate change. *Geophys. Res. Lett.*, 22, 3195-3198.
- Lefohn, A.S., Husar, J.D., Husar, R.B. (1999) Estimating historical anthropogenic global sulfur emission patterns for the period 1850-1990. *Atmos. Environ.*, 33, 3435-3444.
- McMichael, A.J., Woodruff, R.E., Hales, S. (2006) Climate change and human health: present and future risks. *Lancet*, 367, 859-869.
- Meehl, G.A., Washington, W.M., Ammann, C.M., Arblaster, J.M., Wigley, T.M.L., Tebaldi, C. (2004a) Combinations of natural and anthropogenic forcings in 20th century climate. *J. Climate*, 17, 3721-3727.
- Meehl, G.A., Tebaldi, C., Nychka, D. (2004b) Changes in frost days in simulations of twentyfirst century climate. *Clim. Dyn.*, 23, 495-511, DOI 10.1007/s00382-004-0442-9.
- Menon, S., Hansen, J., Nazarenko, L., Luo, Y. (2002) Climate effects of black carbon aerosols in China and India. *Science*, 297, 2250-2253.
- Nakajima, T., Tsukamoto, M., Tsushima, Y., Numaguti, A., Kimura, T. (2000) Modeling of the radiative process in an atmospheric general circulation model. *Appl. Opt.*, 39, 4869-4878.
- Nagashima, T., Shiogama, H., Yokohata, T., Takemura, T., Crooks, S.A., Nozawa, T. (2006) Effect of carbonaceous aerosols on surface temperature in the mid twentieth century. *Geophys. Res. Lett.*, 33, L04702, doi:10.1029/2005GL024887.
- Nozawa, T., Kurokawa, J. (2007) Historical and future emissions of sulfur dioxide and black carbon for global and regional climate change studies. in preparation.
- Nozawa, T., Nagashima, T., Shiogama, H., Crooks, S.A. (2005) Detecting natural influence on surface air temperature change in the early twentieth century. *Geophys. Res. Lett.*, 32, L20719, doi:10.1029/2005GL023540.
- Ramanathan, V., Crutzen, P.J., Kiehl, J.T., Rosenfeld, D. (2001) Aerosols, climate, and the hydrological cycle. *Science*, 294, 2119-2124.
- Ramanathan, V., Chung, C., Kim, D., Bettge, T., Buja, L., Kiehl, J.T., Washington, W. M., Sikka, Q., Fu, D.R., Wild, M. (2005) Atmospheric brown clouds: Impacts on South Asian climate and hydrological cycle. *Proc. Natl. Acad. Sci. USA*, 102, 5326-5333.
- Randel, W.J., Wu, F. (1999) A stratospheric ozone trends data set for global modeling studies. *Geophys. Res. Lett.*, 26, 3089-3092.
- Sato, M., Hansen, J.E., McCormick, M.P., Pollack, J.B. (1993) Stratospheric aerosol optical depths, 1850-1990. *J. Geophys. Res.*, 98, 22987-22994.
- Shiogama, H., Nagashima, T., Yokohata, T., Crooks, S.A., Nozawa, T. (2006) Influence of volcanic activity and changes in solar irradiance on surface air temperatures in the early twentieth century. *Geophys. Res. Lett.*, 33, L09702, doi:10.1029/2005GL025622.
- Stott, P.A., Jones, G.S., Mitchell, J.F.B. (2003) Do models underestimate the solar contribution to recent climate change? *J. Climate*, 16, 4079-4093.



- Stott, P.A., Kettleborough, J.A. (2002) Origins and estimates of uncertainty in predictions of twenty first century temperature rise. *Nature*, 416, 723-726.
- Stott, P.A., Mitchell, J.F.B., Allen, M.R., Delworth, T.L., Gregory, J.M., Meehl, G.A., Santer, B.D. (2006) Observational constraints on past attributable warming and predictions of future global warming. *J. Clim.*, 19, 3055-3069.
- Stott, P.A., Tett, S.F.B., Jones, G.S., Allen, M.R., Ingram, W.J., Mitchell, J.F.B. (2001) Attribution of twentieth century temperature change to natural and anthropogenic causes. *Clim. Dyn.*, 17, 1-21.
- Stott, P.A., Tett, S.F.B., Jones, G.S., Allen, M.R., Mitchell, J.F.B., Jenkins, G.J. (2000) External control of 20th century temperature by natural and anthropogenic forcings. *Science*, 290, 2133-2137.
- Sudo, K., Takahashi, M., Kurokawa, J., Akimoto, H. (2002) CHASER: A global chemical model of the troposphere 1. Model description. *J. Geophys. Res.*, 107, doi:10.1029/2001JD001113.
- Takemura, T., Nozawa, T., Emori, S., Nakajima, T.Y., Nakajima, T. (2005) Simulation of climate response to aerosol direct and indirect effects with aerosol transport-radiation model. *J. Geophys. Res.*, 110, D02202, doi:10.1029/2004JD005029.
- Takemura, T., Tsushima, Y., Yokohata, T., Nozawa, T., Nagashima, T., Nakajima, T. (2006) Time evolutions of various radiative forcings for the past 150 years estimated by a general circulation model, *Geophys. Res. Lett.*, 33, L19705, doi:10.1029/2006GL026666.
- Tebaldi, C., Hayhoe, K., Arblaster, J.M., Meehl, G.A. (2006) Going to the extremes: An intercomparison of model-simulated historical and future changes in extreme events. *Climatic Change*, 79, 185-211, DOI: 10.1007/s10584-006-9051-4.
- Tett, S.F.B., Mitchell, J.F.B., Parker, D.E., Allen, M.R. (1996) Human influence on the atmospheric vertical temperature structure: Detection and observation. *Science*, 274, 1170-1173.
- Tett, S.F.B., Stott, P.A., Allen, M.R., Ingram, W.J., Mitchell, J.F.B. (1999) Causes of twentieth-century temperature change near the Earth's surface. *Nature*, 399, 569-572.
- Tett, S.F.B., Jones, G.S., Stott, P.A., Hill, D.C., Mitchell, J.F.B., Allen, M.R., Ingram, W.J., Johns, T.C., Johnson, C.E., Jones, A., et al. (2002) Estimation of natural and anthropogenic contributions to twentieth century temperature change. *J. Geophys. Res.*, 107(D16), 4306, 2000JD000028.
- Wigley, T.M.L., Jones, P.D., Raper, S.C.B. (1997) The observed global warming record: What does it tell us? *Proc. Natl. Acad. Sci. USA*, 94, 8314-8320.
- Yokohata, T., Emori, S., Nozawa, T., Tsushima, Y., Ogura, T., Kimoto, M. (2005) Climate response to volcanic forcing: Validation of climate sensitivity of a coupled atmosphere-ocean general circulation model. *Geophys. Res. Lett.*, 32, L21710, doi:10.1029/2005GL023542.

## Chapter 6: Projections of Climate Change under IPCC SRES Scenarios

In this chapter, we show the projections of changes in annual mean surface air temperature (SAT) and annual mean precipitation under IPCC SRES scenarios.

### 6.1 Surface Air Temperature

For all scenarios, the global mean SAT anomalies show significant positive trends during the 21st century (Fig. 6.1). The largest warming appears under the A2 scenario (about 4 K anomaly in the 2090s from the 1961-2000 mean). A1B and B1 show about 3.6 K and 2.4 K anomalies in the 2090s. There is an uncertainty in the warming amplitude of about 1.6 K in the 2090s among these 3 scenarios.

Fig. 6.2 shows the spatial patterns of the changes in SAT. Warming is found over almost the entire world for all scenarios. Although the warming amplitude varies among the scenarios, the warming patterns are similar among them: the surface warming is large over the land in the northern hemisphere and over the Arctic Ocean.

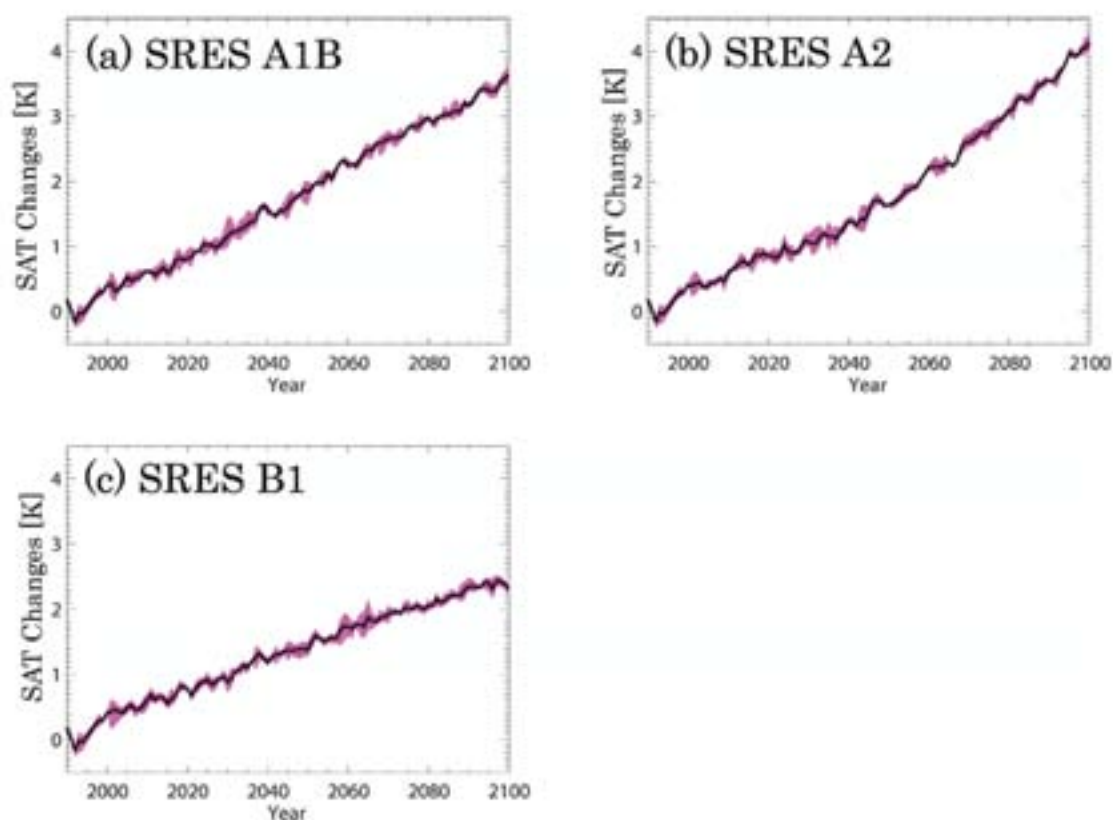


**Fig. 6.1:** Changes in the global mean annual mean of surface air temperature (K; anomalies from the 1961-2000 mean) under (a) the A1B, (b) A2, and (c) B1 scenarios. Solid lines indicate the mean of the 3 ensemble members. Pink shading shows the maximum-minimum range of the 3 ensemble members.

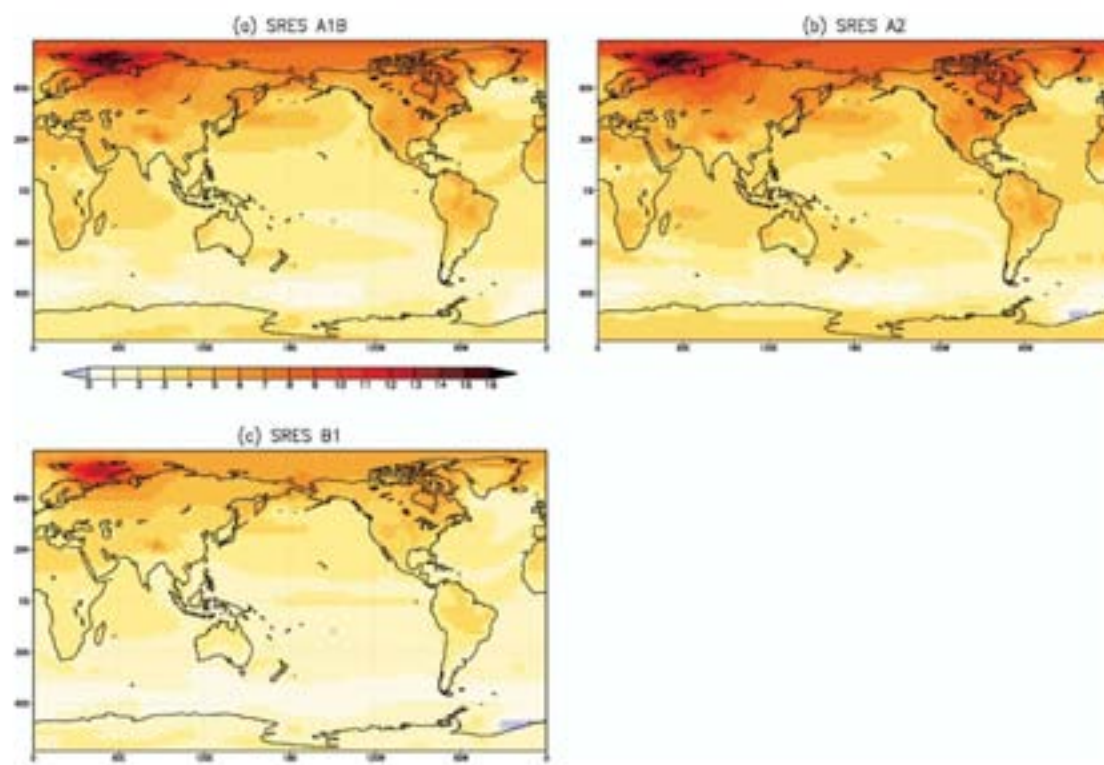
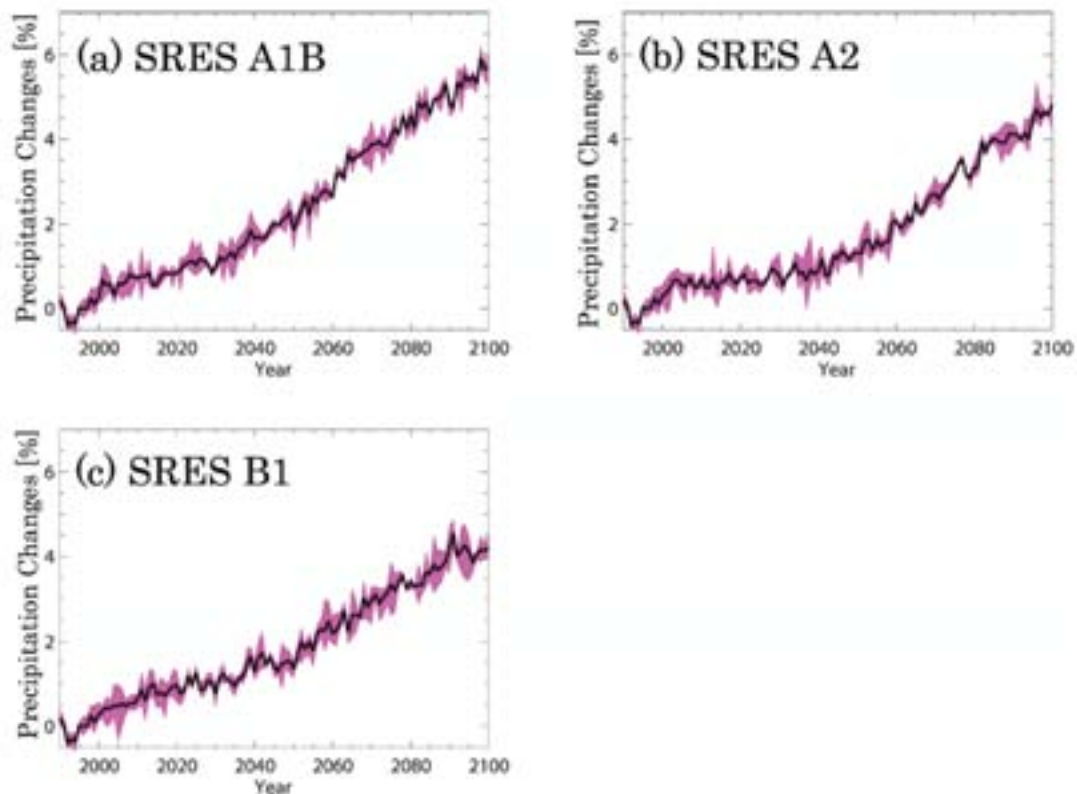


**Fig. 6.2:** Changes in surface air temperature (K; 2081-2100 minus 1961-2000) under (a) the A1B, (b) A2, and (c) B1 scenarios. Shading shows the mean of the 3 ensemble members.

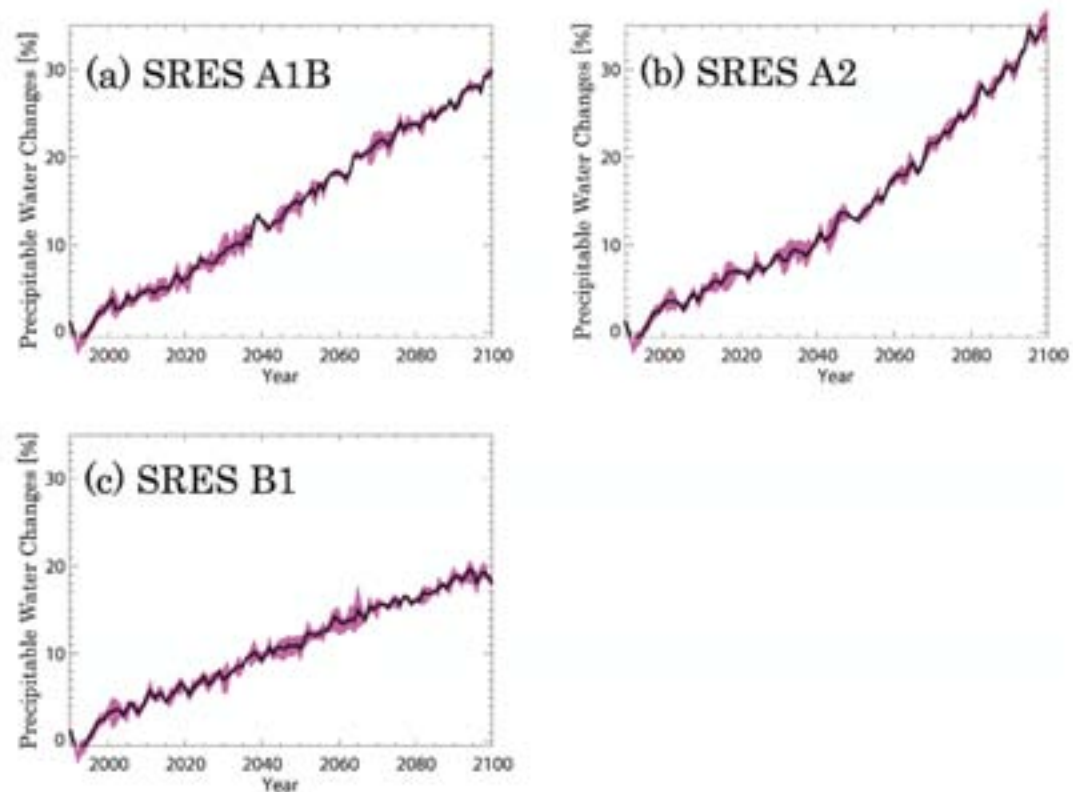
## 6.2 Precipitation

Fig. 6.3 depicts projections of changes in the global mean precipitation. The precipitation anomalies increase during the 21st century for all scenarios. The warming of SAT induces increases of precipitable water (column integrated water vapor) as shown in Fig. 6.4, resulting in an intensification of the hydrological cycle. Relationships between changes in precipitable water and SAT obey the Clausius-Clapeyron theory; the sensitivity of precipitable water to SAT is about 7%/K. The changes in precipitation are smaller than the scaling of the Clausius-Clapeyron theory as discussed by Allen and Ingram (2002). The B1 scenario, which has the smallest warming of SAT, shows the smallest increase in precipitation in the 2090s among these scenarios. Surprisingly, the changes in precipitation in the A2 scenario are smaller than the A1B scenario, whereas the A2 scenario shows larger increases of precipitable water than the A1B scenario. We presume that this smaller increasing rate of precipitation in the A2 scenario is due to the larger loading of aerosol in the A2 scenario than the A1B scenario. Larger loading of aerosol in the A2 scenario would induce more intensified indirect effects of aerosol, resulting in a decrease of precipitation. This hypothesis is supported by Fig. 6.5, which shows the sensitivity of precipitation to SAT warming. The scenarios with larger loading of aerosol show weaker sensitivity of precipitation to SAT.

Fig. 6.6 shows the spatial patterns of changes in precipitation. The pattern of the changes in precipitation does not vary much among these scenarios, although the amplitude of the change varies. Precipitation increases in the tropics and the high latitudes, and decreases in the subtropics.



**Fig. 6.3: Changes in the global mean annual mean of precipitation (percentile changes with respect to the 1961-2000 mean) under (a) the A1B, (b) A2, and (c) B1 scenarios. Solid lines indicate the mean of the 3 ensemble members. Pink shading shows the maximum-minimum range of the 3 ensemble members.**



**Fig. 6.4: Same as Fig. 6.3 except for precipitable water (%).**

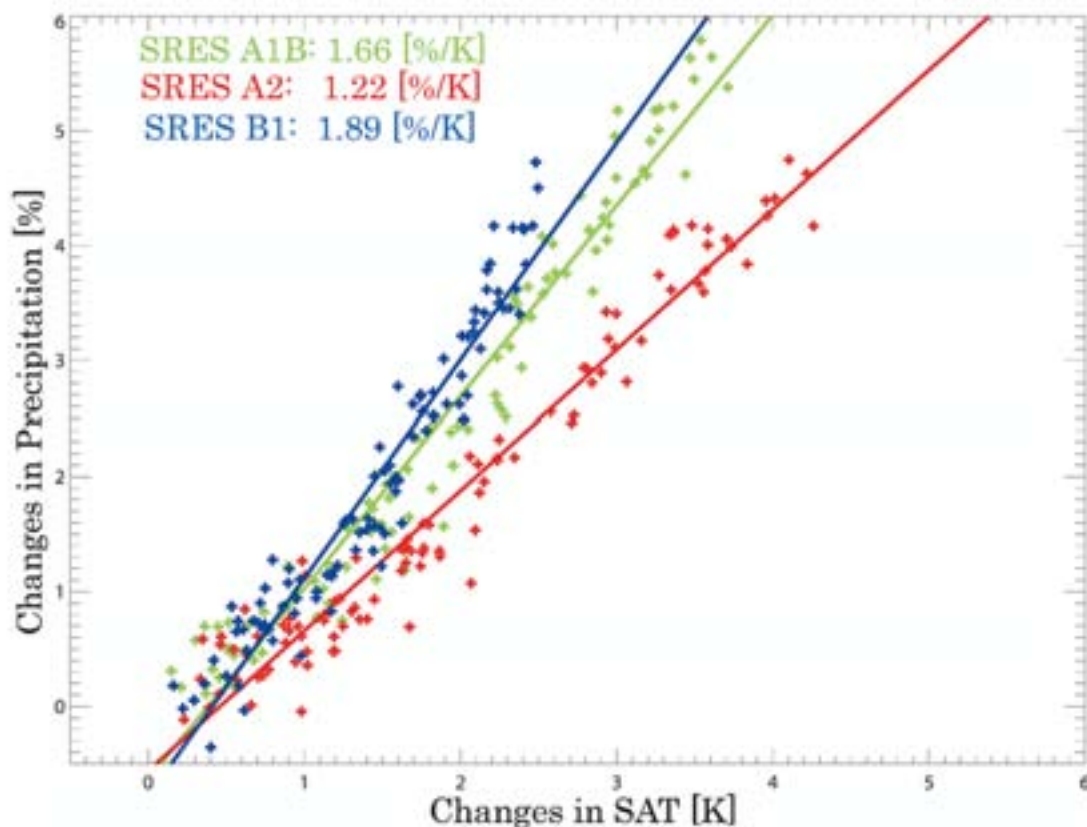


**Fig. 6.5:** Scatter plot of annual mean anomalies of SAT and precipitation for (green) the period of 2001-2100 under the A1B, (red) A2, and (blue) B1 scenarios. Solid lines are linear regressions, and their slopes are shown in the figure.

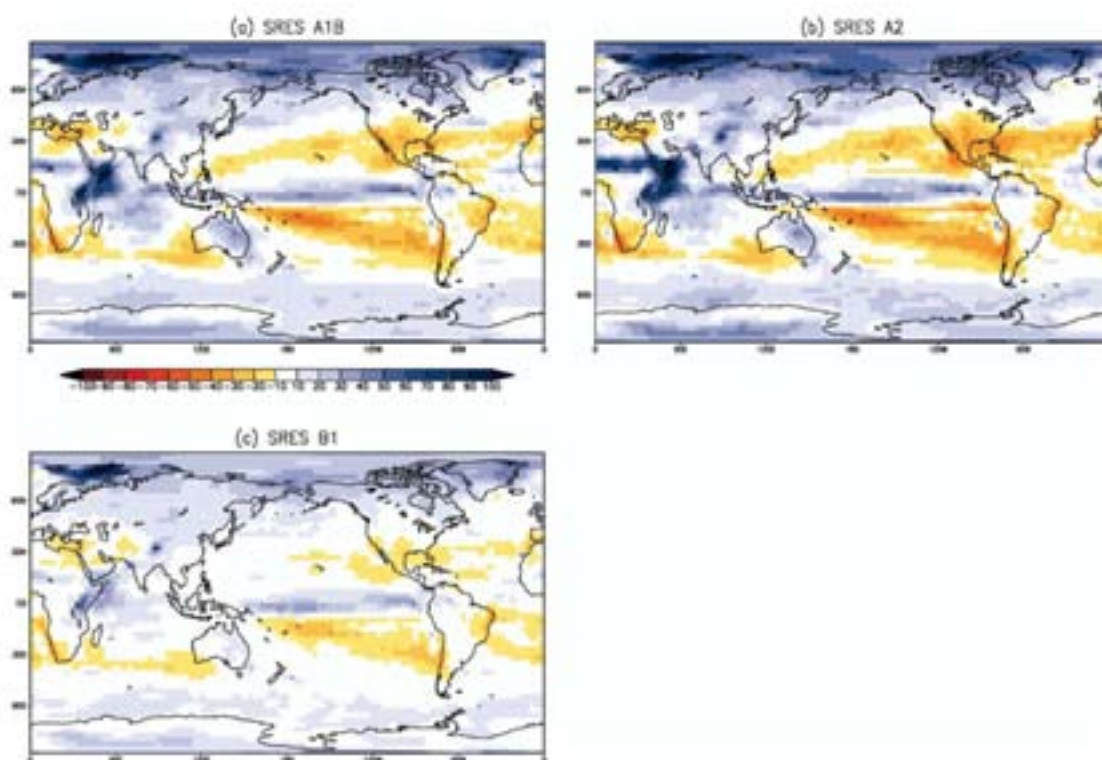


**Fig. 6.6:** Changes in precipitation (%; 2081-2100 minus 1961-2000) under (a) the A1B, (b) A2, and (c) B1 scenarios. Shading shows the mean of the 3 ensemble members.



### 6.3 Commitment Scenarios

If concentrations of greenhouse gases (GHGs) could be stabilized at some level, rises in SAT and precipitation would continue due to oceanic thermal inertia. To quantify committed changes in SAT and precipitation, we performed simulations in which the concentrations of GHGs and the emissions of aerosols are fixed at the levels of the year 2000, or the year 2100 under the A1B or B1 scenarios.

Fig. 6.7 depicts the warming commitment of the global mean SAT. If we can stabilize the concentrations of GHGs and the aerosol emissions at year 2000 levels, an additional warming of about 0.4 K would be committed by the 2090s. A warming commitment of about 0.6 K by 2300 is projected by the simulations in which the concentrations of GHGs and the aerosol emissions are fixed at 2100 levels under the A1B and B1 scenarios. It seems that additional warming continues after 2300. These results are similar to projections with other CGCMs (e.g., Meehl *et al.*, 2005).

Changes in precipitation are similar to those of SAT (Fig. 6.8). If the concentrations of GHGs and the emissions of aerosols were kept at some level, we would be committed to additional increases of global mean precipitation.

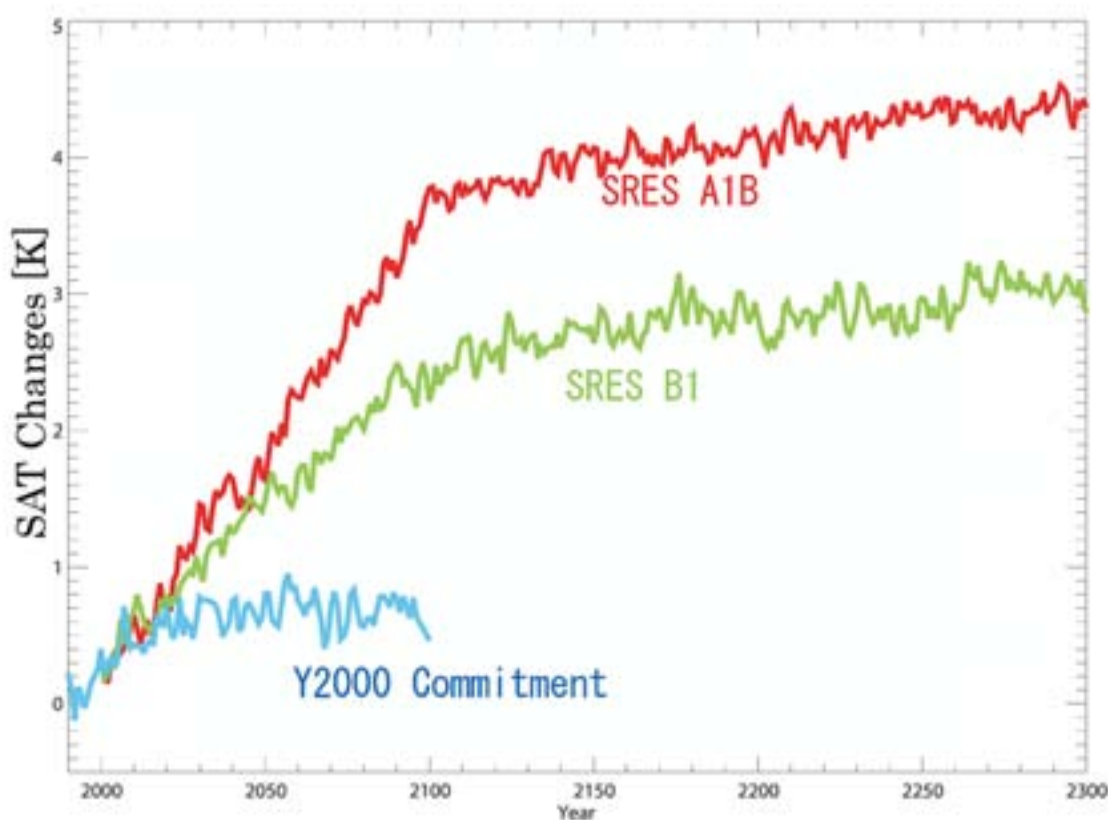
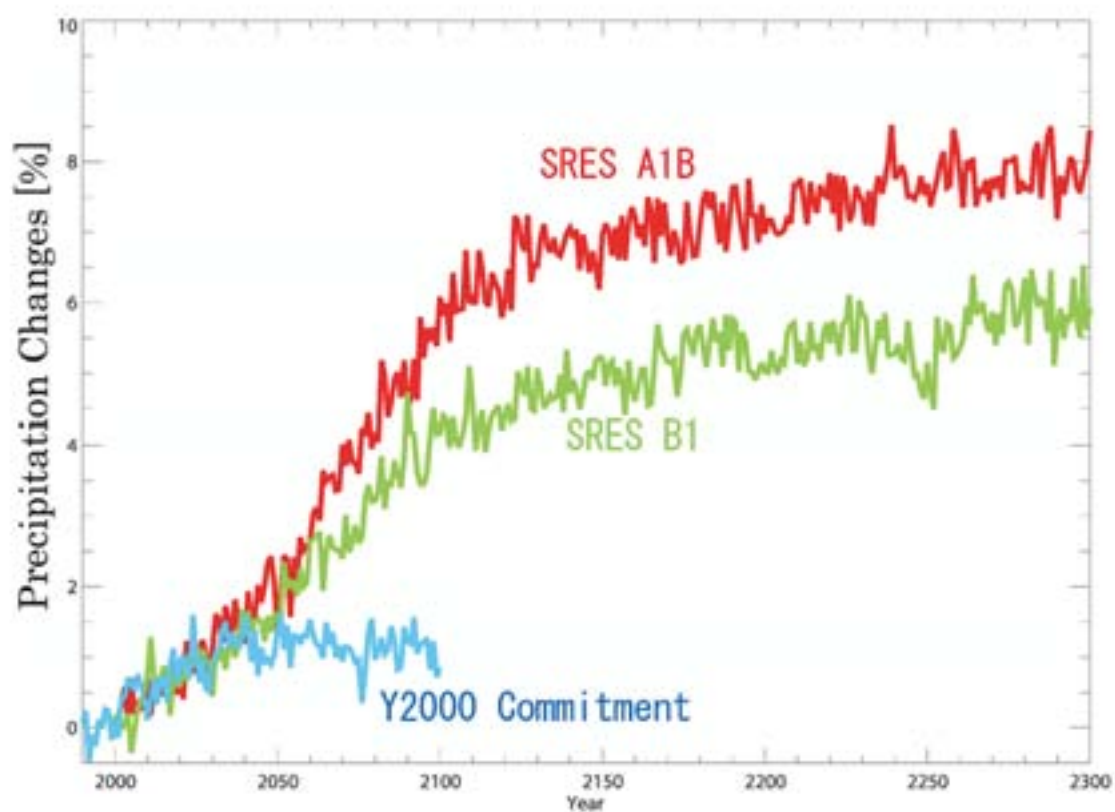


Fig. 6.7: Changes in global mean of surface air temperature (K; anomalies from the 1961-2000 mean) under (red) the year 2100 commitment experiment for A1B (green) and A2, and (blue) the year 2000 commitment experiment.



**Fig. 6.8:** Same as Fig. 6.7 except for precipitation (%).

### References

- Allen, M., Ingram, W. (2002) Constraints on future changes in climate and the hydrologic cycle. *Nature*, 419, 224-232.
- Meehl, G.A., Washington, W.M., Collins, W.D., Arblaster, J.M., Hu, A., Buja, L.E., Strand, W.G., Teng, H. (2005) How much more global warming and sea level rise? *Science*, 307, 1769-1772, DOI: 10.1126/science.1106663.

## Chapter 7: Summary and Conclusions

A series of climate change experiments are performed with a coupled ocean–atmosphere general circulation model (CGCM) called the Model for Interdisciplinary Research on Climate (MIROC; K-1 model developers, 2004). No flux correction is applied in exchanging heat, water, and momentum flux between the atmosphere and the ocean. The atmospheric component of MIROC has an interactive aerosol transport module (Takemura *et al.*, 2000, 2002) that can handle major tropospheric aerosols (sulfate, black carbon, organic carbon, sea salt, and soil dust). It also includes an explicit representation of the first and second kinds of indirect effects induced by soluble aerosols, as well as the direct effects of all aerosols. The equilibrium climate sensitivity to a doubling of CO<sub>2</sub> concentrations of the atmospheric part of MIROC coupled to a mixed-layer ocean is 4.0 K in this resolution. Simulated results are presented for the pre-industrial control run, transient climate change experiment with 1%/year increase in CO<sub>2</sub> concentration, 20th century climate change simulations, and future climate change projections based on the IPCC SRES marker scenarios.

In the pre-industrial control experiment, both global mean surface air temperature (SAT) and global mean soil temperature do not show any significant drift for more than 2000 years. Although global mean ocean temperature shows a slight warming drift, the maximum of stream function of North Atlantic deep water (NADW) does not show any significant drift over 2000 years or more, indicating that the simulated control climate is extremely stable. The spatial distribution of mean climate state shows slight biases for SAT, precipitation, etc., but these appear to be within uncertainty ranges.

The transient climate response (TCR) for global mean SAT is about 1.9 K at the time of doubling CO<sub>2</sub> and about 4.9 K at the time of quadrupling in the 1%/year CO<sub>2</sub> increase experiment, and these TCR values are about average among state-of-the-art climate models around the world. According to a climate feedback analysis with a scheme developed by Yokohata *et al.* (2005), positive climate feedbacks due to changes in water vapor and lapse rate (longwave radiation in the clear-sky), clouds (shortwave radiation), and ocean heat uptake are compensated by the negative Stefan-Boltzmann feedback (surface longwave) for MIROC. Note that net climate feedback due to changes in clouds is variable depending on climate models; thus, it could be necessary to investigate climate feedbacks for multi-model dataset.

In the 20th century climate change simulations, we consider most of external forcings, including both natural and anthropogenic factors: changes in solar irradiance, stratospheric volcanic aerosols, well-mixed greenhouse gases, tropospheric and stratospheric ozone, surface emissions of anthropogenic carbonaceous aerosols and precursors of sulfate aerosols, and land use. Our model can reproduce the observed SAT change, not only for the global annual mean but also for the spatial distribution of long-term SAT trends, with both natural and anthropogenic external forcings. Statistical analyses are carried out using numerous experiments with different combinations of external forcing factors. Our results strongly suggest that the observed warming in the latter half of the 20th century results from anthropogenic forcings. Our results also confirm that the influences of rising greenhouse gas concentrations are detectable in the temperature extremes such as warmest night and frost days in the latter half of the 20th century (Shiogama *et al.*, 2006b). On the other hand, the observed warming in the first half of the 20th century seems to result mainly from natural forcings (Nozawa *et al.*, 2005), although we cannot rule out that increases in greenhouse-gas concentrations influenced global warming in the same period. According to a statistical detection and attribution analysis with the optimal fingerprinting method (Allen and Tett,



1999; Allen and Stott, 2003), the early warming is attributable to the combined effects of recovery from heavy volcanic eruptions and an increase in solar irradiance (Shiogama *et al.*, 2006a). The impact of aerosols on the SAT change is also investigated. The impact of carbonaceous aerosol on the global mean SAT trend is not discernible, but the effect on the horizontal distribution of the SAT trend is significant in the middle of the 20th century (Nagashima *et al.*, 2006).

Climate responses due to increasing concentrations of greenhouse gases and varying ozone and aerosols in the future are projected based on the IPCC SRES scenarios. The spatial distribution of changes in SAT as well as in precipitation is not largely different among the scenarios as shown in Nozawa *et al.* (2003), although the amplitude is different among the scenarios. Changes in global annual mean precipitation are larger in the SRES A1B scenario than in the A2 scenario but changes in global annual mean precipitable water are vice versa, indicating that changes in global hydrological cycle are different among the scenarios. These differences seem to be caused by different aerosol loadings, and to confirm this further investigations are needed.

## Acknowledgements

The authors thank the K-1 project members for their support and discussions, and two anonymous reviewers for their valuable comments. They also thank Chizuru Kogai for help with the manuscript. This work was supported by the Research Revolution 2002 (RR2002) of the Ministry of Education, Culture, Sports, Science and Technology, and by the Global Environment Research Fund (GERF) of the Ministry of the Environment of Japan. An NEC SX-6 at NIES and the Earth Simulator were employed to perform the CGCM simulations. The GFD-DENNOU Library was used for some of the figures.

## References

- Allen, M.R., Tett, S.F.B. (1999) Checking for model consistency in optimal fingerprinting. *Clim. Dyn.*, 15, 419-434.
- Allen, M.R., Stott, P.A. (2003) Estimating signal amplitudes in optimal fingerprinting, part I: theory. *Clim. Dyn.*, 21, 477-491.
- K-1 model developers (2004) K-1 coupled GCM (MIROC) description, K-1 technical report. 1, Hasumi, H., Emori, S. (eds.), Center for Climate System Research, University of Tokyo, Tokyo, 34pp.
- Nagashima, T., Shiogama, H., Yokohata, T., Takemura, T., Crooks, S.A., Nozawa, T. (2006) Effect of carbonaceous aerosols on surface temperature in the mid twentieth century. *Geophys. Res. Lett.*, 33, L04702, doi:10.1029/2005GL024887.
- Nozawa, T., Emori, S., Numaguti, A., Tsushima, Y., Takemura, T., Nakajima, T., Abe-Ouchi, A., Kimoto, M. (2003) Transient climate change simulations in the 21st century with the CCSR/NIES CGCM under a new set of IPCC SRES scenarios, CGER's Supercomputer Monograph Report, 8, CGER-REPORT, CGER/NIES, Tsukuba, 44pp.
- Nozawa, T., Nagashima, T., Shiogama, H., Crooks, S.A. (2005) Detecting natural influence on surface air temperature change in the early twentieth century. *Geophys. Res. Lett.*, 32, L20719, doi:10.1029/2005GL023540.
- Shiogama, H., Nagashima, T., Yokohata, T., Crooks, S.A., Nozawa, T. (2006a) Influence of volcanic activity and changes in solar irradiance on surface air temperatures in the early twentieth century. *Geophys. Res. Lett.*, 33, L09702, doi:10.1029/2005GL025622.
- Shiogama, H., Christidis, N., Caesar, J., Yokohata, T., Nozawa, T., Emori, S. (2006b) Detection of greenhouse gas and aerosol influences on changes in temperature extremes. *SOLA*, 2, 152-155, doi:10.2151/sola.2006-039.
- Takemura, T., Okamoto, H., Maruyama, Y., Numaguti, A., Higurashi, A., Nakajima, T. (2000) Global three-dimensional simulation of aerosol optical thickness distribution of various origins. *J. Geophys. Res.*, 105, 17,853-17,873.
- Takemura, T., Nakajima, T., Dubovik, O., Holben, B.N., Kinne, S. (2002) Single-scattering albedo and radiative forcing of various aerosol species with a global three-dimensional model. *J. Climate*, 15, 333-352.
- Yokohata, T., Emori, S., Nozawa, T., Ogura, T., Tsushima, Y., Kimoto, M. (2005) A simple scheme for climate feedback analysis. *Geophys. Res. Lett.*, 32, L19703, doi:10.1029/2005GL023673.



## **CGER'S SUPERCOMPUTER MONOGRAPH REPORT**

### **Back Issues**

- Vol. 1 CGER-I021-'96 (Out of stock)  
Turbulence Structure and CO<sub>2</sub> Transfer at the Air-Sea Interface and Turbulent Diffusion in Thermally-Stratified Flows
- Vol. 2 CGER-I022-'96  
A Transient CO<sub>2</sub> Experiment with the MRI CGCM -Annual Mean Response -
- Vol. 3 CGER-I025-'97  
Study on the Climate System and Mass Transport by a Climate Model
- Vol. 4 CGER-I028-'97 (Out of stock)  
Development of a Global 1-D Chemically Radiatively Coupled Model and an Introduction to the Development of a Chemically Coupled General Circulation Model
- Vol. 5 CGER-I035-'99  
Three-Dimensional Circulation Model Driven by Wind, Density, and Tidal Force for Ecosystem Analysis of Coastal Seas
- Vol. 6 CGER-I040-2000  
Tropical Precipitation Patterns in Response to a Local Warm SST Area Placed at the Equator of an Aqua Planet
- Vol. 7 CGER-I045-2001  
New Meteorological Research Institute Coupled GCM (MRI-CGCM2)  
Transient Response to Greenhouse Gas and Aerosol Scenarios
- Vol. 8 CGER-I055-2003 (Out of stock)  
Transient Climate Change Simulations in the 21st Century with the CCSR/NIES CGCM under a New Set of IPCC Scenarios
- Vol. 9 CGER-I057-2004  
Vortices, Waves and Turbulence in a Rotating Stratified Fluid
- Vol.10 CGER-I060-2005  
Modeling of Daily Runoff in the Changjiang (Yangtze) River Basin and Its Application to Evaluating the Flood Control Effect of the Three Gorges Project
- Vol.11 CGER-I063-2006  
Development of process-based NICE model and simulation of ecosystem dynamics in the catchment of East Asia (Part I)

Copies of these reports can be obtained by contacting:  
Center for Global Environmental Research  
National Institute for Environmental Studies  
16-2 Onogawa, Tsukuba, Ibaraki 305-8506, Japan

These reports are also available as PDF files.  
See: [http://www-cger.nies.go.jp/cger-e/e\\_report/r\\_index-e.html](http://www-cger.nies.go.jp/cger-e/e_report/r_index-e.html)



*This book is printed on recycled paper.*